Resolvent-based modeling of flows in a channel

Thesis by
Kevin Rosenberg

In Partial Fulfillment of the Requirements for the
Degree of
Doctor of Philosophy

CALIFORNIA INSTITUTE OF TECHNOLOGY
Pasadena, California

2018
Defended May 21, 2018

Kevin Rosenberg
ORCID: 0000-0001-6101-3823

ACKNOWLEDGEMENTS

First and foremost, I would like to thank my advisor Beverley McKeon. This thesis would not have been possible without her guidance and support over the past six years. I would also like to thank my committee: Tim Colonius, Anthony Leondard, and Dan Meiron for their helpful comments and suggestions. The support of the AFOSR (FA 9550-16-1-0361, FA 9550-12-1-0469) and ONR (N00014-17-1-2307) is also gratefully acknowledged.

I would like to thank J.S. Park and M.D. Graham from the University of Wisconsin for sharing their data. I would also like to thank J. Gibson from the University of New Hampshire for making his data and software openly available on his website. Additionally, I wish to thank A.L. Duràn and A. Towne from Stanford University for their collaboration stemming from the CTR summer program.

I would like to thank A. Sharma and A. Ahmed from the University of Southampton for hosting me during my visit to the U.K. and for their continued collaboration.

I am extremely grateful towards Jamie Sei for all the support she provided and the wonderful conversations we shared. I would like to thank the GALCIT staff: Peggy, Dimity, Christine, and Denise for their tremendous assistance over the years. I would also like to thank Joe, Ali, and Matt from the machine shop for their patience and willingness to help in my early years as an experimentalist.

I would like to thank all the members of the McKeon research group for their kindness, their willingness to always discuss research problems, and for providing great memories from our many social activities. A special thank you to Tess for the illuminating conversations we shared at CTR and to Sean for the numerous ideas we discussed while sharing an office.

I would like to thank my incoming class of friends: Chris, Melanie, Neel, Sean, and Simon for the wonderful memories. I would also like to thank all the amazing people I met along the way: Ishan, Nick, Amber, Dingyi, Reid, Andrew. I am a very lucky person to have been able to spend so much time with such intelligent and hilarious people.

Lastly, I thank my family for always supporting my education.

ABSTRACT

This thesis concerns the continued development of the resolvent framework (McKeon and Sharma, 2010) to model wall-bounded turbulent flows. Herein, we introduce novel modifications and extensions of the framework to improve the compact representation of flows in a channel. In particular, inspired by ideas rooted in classical linear stability theory, we introduce a decomposition of the velocity field into Orr-Sommerfeld (OS) and Squire (SQ) modes in a nonlinear context via the resolvent operator. We demonstrate through the analysis of a number of exact coherent states (ECS) of the Navier-Stokes equations (NSE) in Couette and Poiseuille flow that this decomposition offers a significant improvement in the low-dimensional representation of these flows. With this efficient basis, we are able to develop through the notion of interaction coefficients a method to compute accurate, self-consistent solutions of the NSE with knowledge of only the mean velocity profile. We also highlight the role of the solenoidal component of the nonlinear forcing in the solution process. In addition, the resolvent framework is extended to the analysis of 2D/3C flows. This approach, again applied to ECS, sheds light on the underlying scale interactions which sustain these solutions. Notably, it reveals that lower branch ECS can be effectively described in their entirety with a single resolvent response mode. This discovery is leveraged to construct a method to compute accurate approximations of ECS starting from a laminar profile using a single parameter model. This thesis also utilizes a constant time-step DNS of a turbulent channel to perform a direct characterization of the nonlinear forcing terms. We compute power spectra and confirm that the nonlinear forcing has a non-trivial signature in the wavenumber-frequency domain. We also compute and analyze spectra for the OS/SQ vorticity and discuss the potential benefit of this decomposition technique to the study of fully turbulent flows as well.

PUBLISHED CONTENT AND CONTRIBUTIONS

Rosenberg, K., Duvvuri, S., Luhar, M., McKeon, B.J., Barnard, C., Freidkes, B., Meloy, J., and Sheplak, M. (2016a). "Phase relationships between velocity, wall pressure, and wall shear stress in a forced turbulent boundary layer". In: *46th AIAA Fluid Dynamics Conference*. DOI: 10.2514/6.2016-4396.

Assisted in making the experimental measurements, created the figures, and was the primary author of the paper.

Rosenberg, K. and McKeon, B.J. (2018). "Efficient representation of exact coherent states of the Navier-Stokes equations using resolvent analysis". In: *Fluid Dynamics Research (to appear)*. DOI: 10.1088/1873-7005/aab1ab.

Analyzed the data, created the figures, and was the primary author of the paper.

Rosenberg, K., Saxton-Fox, T., Lozano-Duràn, A., Towne, A., and McKeon, B.J. (2016b). "Toward low order models of wall turbulence using resolvent analysis". In: *Proceedings of the CTR Summer Program*. URL: http://resolver.caltech.edu/CaltechAUTHORS:20171128-094432410.

Analyzed the DNS data for the turbulent channel, was the primary author of section 3, and contributed text to the Introduction/Conclusion.

Symon, S., Rosenberg, K., Dawson, S., and McKeon, B.J. (2018). "On non-normality and classification of amplification mechanisms in stability and resolvent analysis". In: *Physical Review Fluids*. DOI: 10.1103/PhysRevFluids.3.053902.

Performed the analysis, generated the figures, and contributed text to Section V.

TABLE OF CONTENTS

LIST OF ILLUSTRATIONS

Number *Page*

LIST OF TABLES

NOMENCLATURE

x: Streamwise coordinate

y: Wall-normal coordinate

z: Spanwise coordinate

u: Streamwise velocity

v: Wall-normal velocity

w: Spanwise velocity

η: Wall-normal vorticity

t: Time

h: Channel half-height

p: Pressure

u_τ: Friction velocity

Re_τ: Friction Reynolds number

L_x: Streamwise length of simulation box

L_z: Spanwise length of simulation box

N_x: Number of streamwise discretization points

N_y: Number of wall-normal discretization points

N_z: Number of spanwise discretization points

k_x: Streamwise wavenumber

k_z: Spanwise wavenumber

ω: Radial frequency

c: Streamwise wavespeed of traveling wave

Chapter 1

INTRODUCTION

1.1 Motivation

The phenomenon of turbulence is ubiquitous; from the passage of air over the wings of a plane, to the transport of oil in pipelines, and even within the stars above, its presence is felt throughout nature. Unfortunately, from a practical standpoint, associated with turbulent flows over engineering surfaces of interest is a significant increase in drag and hence an equally significant economic cost in overcoming it. Even modest reductions in the turbulent drag would yield savings on the order of billions of dollars annually in the shipping and airline industries (Kim, 2011), and thus a complete understanding of turbulence remains an important scientific and engineering challenge.

The dynamics of turbulence (and fluid flows in general) are governed by a set of nonlinear partial differential equations known as the Navier-Stokes equations (NSE). The broad range of spatio-temporal scales present in most turbulent flows of practical interest and their intrinsic coupling dictated by the nonlinear NSE gives rise to immensely complicated flow fields. Despite decades of experimental measurements and recent advancements in direct numerical simulations (DNS) of the NSE, a comprehensive description of many aspects of turbulence eludes us. However, buried within this sea of complex motion, is evidence of coherent structures which underlie the fundamental processes of turbulent flows and thus provide an avenue for understanding the apparent complexity in terms of simpler pieces. This has motivated the development of low-order models to identify these dynamically and energetically significant features, as well as attempts to understand how they interact to sustain turbulence and its salient characteristics. It is hoped these models will be part of a systematic framework used to make useful predictions for engineering flows of interest and as a tool for the development of efficient control strategies.

In this chapter, we give an overview of various methods and analysis techniques developed to provide low-order descriptions of turbulent flows. This will include recent advancements of the resolvent framework of McKeon and Sharma, 2010, which will be utilized throughout this thesis. We conclude with an overview of the present

approach and the numerical datasets utilized, along with the key contributions of this thesis.

1.2 Low-order descriptions of turbulence

We will begin with a brief overview of modal decomposition techniques commonly used in the analysis of fluid flows as recently outlined by Taira et al., 2017. Next, we will provide a survey of the work performed with respect to the analysis of the linearized NSE, which will provide a natural motivation for the resolvent model. We will then describe the so-called quasilinear approaches, which attempt to incorporate limited nonlinear effects, and their connections to the self-sustenance of turbulence. We will conclude with the recent advancements in the computation of exact coherent states, fully nonlinear invariant solutions to the NSE.

Modal decompositions

The seminal experimental measurements of Kline et al., 1967, which clearly provided evidence of organized near-wall streaks in a boundary layer, were one of the earliest instances identifying the existence and importance of coherent structures in turbulent flows. In this context, coherent structures refer to features that are persistent in both space and time that serve prominent roles in the transport of mass, momentum, and energy in a flow (Marusic et al., 2010). A recent overview of coherent structures in turbulent flows is found in Jiménez, 2018. Most flows of scientific interest, turbulent or not, exhibit the presence of coherent structures, and thus there has been a large body of work developed to mathematically extract these structures and use them to build low-order representations of these flows. There are many existing approaches and they can be broadly split into two categories (Taira et al., 2017): data-driven and operator-driven. In both instances, the aim is to construct an optimal basis (in some defined sense) to represent the flow field; the former relies on snapshots of data from experiments or simulations while the latter exploits the mathematical structure of the governing equations. An extensive overview of existing techniques and their use in literature is found in Rowley and Dawson, 2017 and Taira et al., 2017. In what follows, we provide a condensed description of some of the more prominent data-driven techniques used in the field. Of the operator-driven techniques, our focus will be on resolvent analysis, which we shall discuss in further detail later in the section.

One of the older and most used methods in the fluid dynamics community is the

proper orthogonal decomposition (POD), first introduced by Lumley, 1967. This method generates (from data) an ordered set of basis functions that are optimal with respect to capturing the total kinetic energy of the flow. In this sense, the notion of extracting coherent structures is linked to the dominance of their energetic signature. In some instances, a projection onto a small subset of these basis functions will capture a large percentage of the total energy, and thus the representation of the flow using this basis can be significantly truncated. An attractive property of POD is that the basis functions are orthogonal; this property can be leveraged to construct reduced-order models of the high-dimensional NSE via Galerkin projection as explored by Aubry et al., 1988. It should be noted that most modern applications of POD employ a separation of variables and compute coherent spatial basis functions which are accompanied by time-varying amplitudes to describe their temporal evolution. Recently, Towne et al., 2017a have introduced a variant termed the spectral proper orthogonal decomposition (SPOD) (whose origins can be traced back to the work of Lumley, 1967), which instead considers (for stationary flows) an expansion in time-harmonic modes and computes orthogonal basis functions at discrete frequencies; this technique has been successfully applied to the analysis of turbulent jets (Schmidt et al., 2017).

Generally speaking, one limitation of POD is that sometimes the most energetic structures are not always the most dynamically significant, a limitation that is addressed by balanced-POD. This approach, rooted in controls theory, attempts to retain modes that are both highly controllable and highly observable through the introduction of a coordinate transformation. Requiring the solution of an adjoint system, this approach is mostly limited to computational studies. Particularly for systems where the underlying dynamics are nonnormal (an idea we will discuss in more detail shortly), the balanced POD can provide an improved representation in comparison to POD (Ilak and Rowley, 2008).

Another data-driven technique that has seen a rapid development in the past couple of years is the dynamic mode decomposition (DMD) (Schmid, 2010), which shares connections to Koopman analysis (Rowley et al., 2009). This method extracts spatial modes, each with an associated frequency and growth rate, by fitting a linear operator between pairs of time snapshots. In this sense, it often has connections to the discrete Fourier transform and to the previously mentioned SPOD (Towne et al., 2017a). DMD can be applied to a wide range of data and has spawned many variations to promote desirable properties such as sparsity. Unlike POD, however,

there is no natural ranking of DMD modes and sometimes the selection of the most physically relevant modes is not a straightforward process. In addition, as DMD involves a linear fit between time snapshots, it can sometimes poorly represent flows where nonlinear effects are prominent. Despite some of the aforementioned weaknesses, DMD has seen extensive use in fluid mechanics (and other fields) due to its versatility. It has also been applied recently in the development of near-wall models of turbulent flows (Schmid and Sayadi, 2017).

While such data-driven methods continue to make important contributions to our understanding of turbulence, we now shift our attention to methods rooted deeply in the governing NSE.

Linearized NSE

Though turbulence is undoubtedly a nonlinear phenomenon, it has come to light that linear mechanisms play a prominent role in the dynamics of turbulent flows (Farrell, 1988; Kim and Lim, 2000; Jiménez, 2013). Early studies in the linear stability analysis of laminar base flows, pioneered by the formulations of Orr and Sommerfeld for parallel shear flows (Orr, 1907; Sommerfeld, 1908), were used to understand and make predictions about the transition to turbulence. However, in some instances, this led to the prediction that certain shear flows were linearly stable (via an eigen-analysis) for all Reynolds numbers, a fact clearly refuted by experimental observations (Drazin and Reid, 1981). A significant breakthrough came in the early 1990s when it was appreciated that the linearized Navier-Stokes operator is in general nonnormal (i.e. the operator has a set of nonorthogonal eigenvectors) (Trefethen et al., 1993; Reddy et al., 1993; Butler and Farrell, 1992). This property leads to the phenomenon of transient growth where stable modes can grow significantly over short time-horizons; it was then argued this growth could be large enough to trigger nonlinear effects and subsequent transition to turbulence.

Upon appreciation of this behavior, studies sought to compute the optimal perturbations which led to the largest transient growth (i.e. the most dangerous initial conditions) (Schmid and Henningson, 2000). This was explored in (laminar) Couette and Poiseuille flow by Butler and Farrell, 1992 and Reddy and Henningson, 1993, which revealed structures in the form of (spanwise-varying) streamwise vortices to be the optimal perturbation. These structures were reminiscent of the quasi-streamwise vortices (and associated streaks) observed in near-wall turbulence and thus offered an enticing explanation for the emergence of these features from

linear origins. This formulation was extended to the analysis of a turbulent mean flow via the introduction of an eddy-viscosity term (Del Álamo and Jiménez, 2006) (which accounts for the fact that the turbulent mean is not a solution to the NSE) and similarly yielded streamise-constant vortices as the optimal perturbations.

In addition to the investigation of initial conditions on finite time-horizons, the nonnormality of the linearized NSE was further probed via its response to external stochastic and harmonic forcing. Farrell and Ioannou, 1993 showed via stochastic excitation of the linearized NSE for Couette and Poiseuille flow that perturbations could extract energy from the mean flow via linear nonnormal mechanisms and sustain large variance levels. Jovanović and Bamieh, 2005 considered the input/output response of the linearized NSE to external harmonic forcing for Poiseuille flow. This analysis investigated the properties of the transfer function which mapped input to output, henceforth referred to as the resolvent operator (Schmid and Henningson, 2000). The resolvent operator, and its use in a turbulent context (McKeon and Sharma, 2010), will be discussed in further detail shortly. The work of Jovanović and Bamieh, 2005 further confirmed the large amplification of streamwise-constant modes via nonnormal mechanisms; in addition, via a componentwise analysis, it identified that the large streamwise response stemmed from forcing in the cross-stream directions. These analyses were again extended to the study of the turbulent mean (with an eddy viscosity model as before) by Hwang and Cossu, 2010, who also found similar results.

Such studies have motivated the development of models which consider the linearized NSE (about the turbulent mean) subject to stochastic forcing as a means to explain the observed statistical and structural features of turbulent flows. Of particular interest has been the required characteristics of the stochastic forcing needed to accurately reproduce the statistics of the flow. While in many cases an assumption of white-in-time forcing is invoked, a recent study by Zare et al., 2017 argued that the forcing must be colored-in-time (i.e. its spectral content must vary with frequency) in order to recover second order statistics in a turbulent channel flow.

Resolvent analysis of turbulent flows

In contrast, the resolvent formulation of McKeon and Sharma, 2010 takes a slightly different approach. Instead of the addition of an external forcing term, they treat the nonlinear term of the NSE as an endogenous forcing. With this interpretation, an input/output analysis of the NSE with respect to the turbulent mean (assumed known

a priori) can be performed without any explicit linearization (or assumption of small perturbations) to form a self-consistent description of the governing equations. In this context, self-consistency arises from the fact that the input is inextricably linked to the output through the nonlinear interactions. This approach was significant as previous studies had recognized linearizing about the mean flow, while not strictly justified, could provide useful information about the dominant structures and frequencies in the flow (Barkley, 2006); consequently, this provided a formal framework for analyzing the (linear) resolvent operator associated with the turbulent mean even though the mean itself does not constitute a solution to the NSE.

In McKeon and Sharma, 2010, following a decomposition of the velocity field into Fourier modes in the wall-parallel directions and in time, a singular value decomposition (SVD) of the resolvent operator was used to identify highly amplified input/output pairs (in an energetic sense) to generate a low-dimensional basis in the wall-normal direction. The basis is naturally ranked by the amplitude of the associated singular values. The mathematical details behind this framework will be derived in §2.1. It was found for most of the energetically relevant wavenumbers and frequencies that the resolvent operator was low rank (i.e. the first singular value was dominant). This enabled a simplifying rank one approximation, which has been used extensively to model and examine many aspects of turbulence including the scaling of the streamwise energy intensity for large Reynolds numbers (Moarref et al., 2013), the generation of coherent structures such as hairpin packets (Sharma and McKeon, 2013b), a gain-based analysis of opposition control (Luhar et al., 2014), and the development of a framework for the systematic design of compliant surfaces for potential drag reduction applications (Luhar et al., 2015). A comprehensive summary of the progress of the resolvent model for the analysis of wall turbulence is found in McKeon, 2017. Resolvent-based approaches have also been applied to the study of turbulent flow over a backward facing step (Beneddine et al., 2016) and to the analysis of turbulent jets (Towne et al., 2015; Towne, 2016; Schmidt et al., 2017).

The resolvent model of McKeon and Sharma, 2010 will be at the core of this thesis. While most of the work with this model has focused on the properties of the resolvent operator itself, there has been less attention paid to the nonlinear forcing. A notable exception is the work of Moarref et al., 2014, which used optimization to indirectly determine the forcing needed to match energy spectra from the DNS of a turbulent channel. Nonetheless, part of this thesis will serve to fill this void; however, we defer

a discussion of the intended course of action until the next section and continue to describe other modeling efforts which will be relevant to the content of this thesis.

Quasilinear approximation

Quasilinear approaches attempt to reduce the full complexity of the NSE by restricting the number of permissible nonlinear interactions. Due to dominant presence of streamwise-constant structures as described earlier, the flow field is decomposed into a 2D/3C (2-dimensional, 3-component) streamwise-averaged mean, and corresponding streamwise-varying perturbations. The equation that governs the mean flow retains all the nonlinear interactions, i.e. the interaction of the perturbations with their complex conjugates. However, the equation that governs the perturbations allows for interactions with the mean, but not perturbation-perturbation interactions; this term is either neglected entirely or parameterized with stochastic forcing (Gayme et al., 2010; Farrell and Ioannou, 2012). Thus, each perturbation is allowed to interact with itself to feedback to the mean, but the dynamics of the perturbation itself are governed by a linear equation. Interestingly, with these limited interactions, these quasilinear models are able to generate flow features reminiscent of true turbulence, reproduce first-order statistics, and self-sustain (Thomas et al., 2014; Farrell et al., 2016). Furthermore, only a small number of streamwise-varying modes are needed to self-sustain the flow giving further credence to the vision of the self-sustaining process proposed by Waleffe, 1997.

In a natural progression from the discussion of the linearized NSE and subsequently the quasilinear approximation, we now discuss fully nonlinear attempts to describe turbulence.

Exact coherent states

The interpretation of the NSE as a dynamical system has led to the discovery of exact coherent states (ECS), nonlinear invariant solutions that take the form of equilibria, traveling waves, and periodic orbits. Two-dimensional solutions were found by Herbert, 1977 for Poiseuille flow by extending the analysis of the neutral stability curve to the determination of neutral finite-amplitude states using bifurcation theory. The first computation of a three-dimensional solution for Couette flow is due to Nagata, 1990, who continued solutions from Taylor-Couette flow to the case with zero average rotation rate. Additionally, three-dimensional solutions were found in Poiseuille flow by Ehrenstein and Koch, 1991, notably at Reynolds numbers close

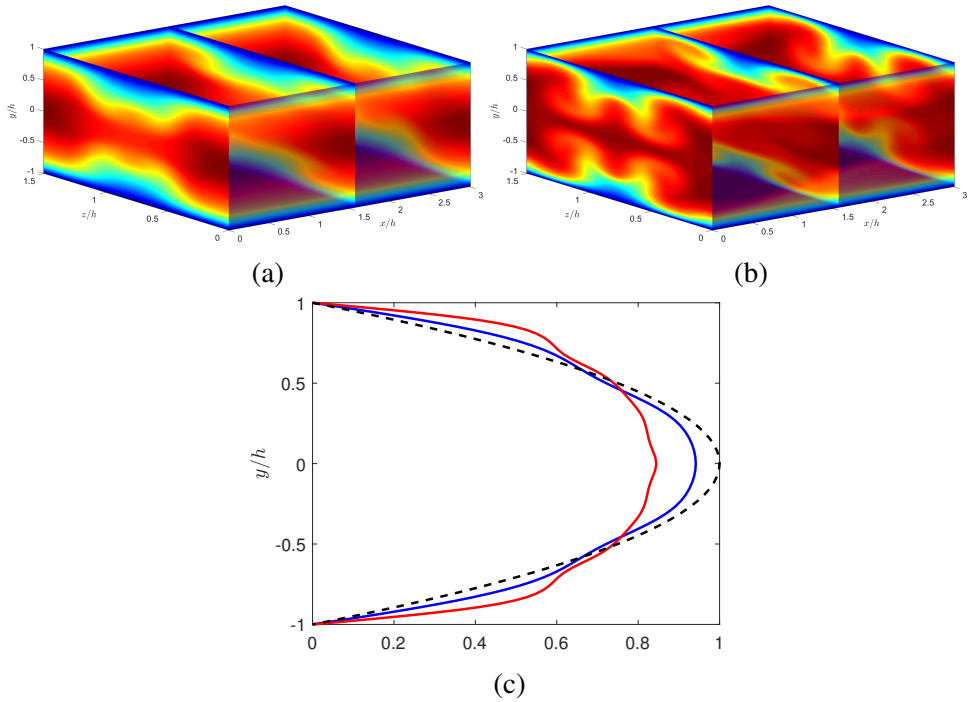

Figure 1.1: Contours of the streamwise velocity for the traveling wave solutions (Poiseuille) (a) P4L, (b) P4U, and (c) a comparison of their 1D mean profiles (P4L: blue, P4U: red) with respect to the laminar profile (dashed line). Data courtesy of Park and Graham, 2015.

to the experimentally observed value where transition to turbulence occurs. ECS have been hypothesized to constitute the state-space skeleton of turbulent dynamics (Kawahara et al., 2012). Families of solutions have been found for all the canonical geometries, including pipes and channels. Solutions primarily arise in pairs due to a bifurcation (often a saddle-node bifurcation) at a finite Reynolds number, where the lower branch (L) solutions (closer in appearance to the laminar state) have lower drag in comparison to the upper branch (U) solutions (closer in appearance to the turbulent state). In Figures 1.1 and 1.2, we plot the velocity field of two such pairs of solutions for Poiseuille flow and Couette flow respectively. The Poiseuille lower and upper branch (traveling-wave) solutions, termed P4L and P4U, were computed by Park and Graham, 2015, who demonstrated interesting connections between these solutions and viscoelastic and Newtonian turbulence. The Couette equilibria, termed EQ1 and EQ2 (where EQ1 corresponds to the original solution of Nagata, 1990, here recomputed by Gibson et al., 2009) have been well studied in the literature, notably their Reynolds number scaling (Wang et al., 2007) and state-space representation (Gibson et al., 2008). In addition to the statistical properties of the upper branch ECS

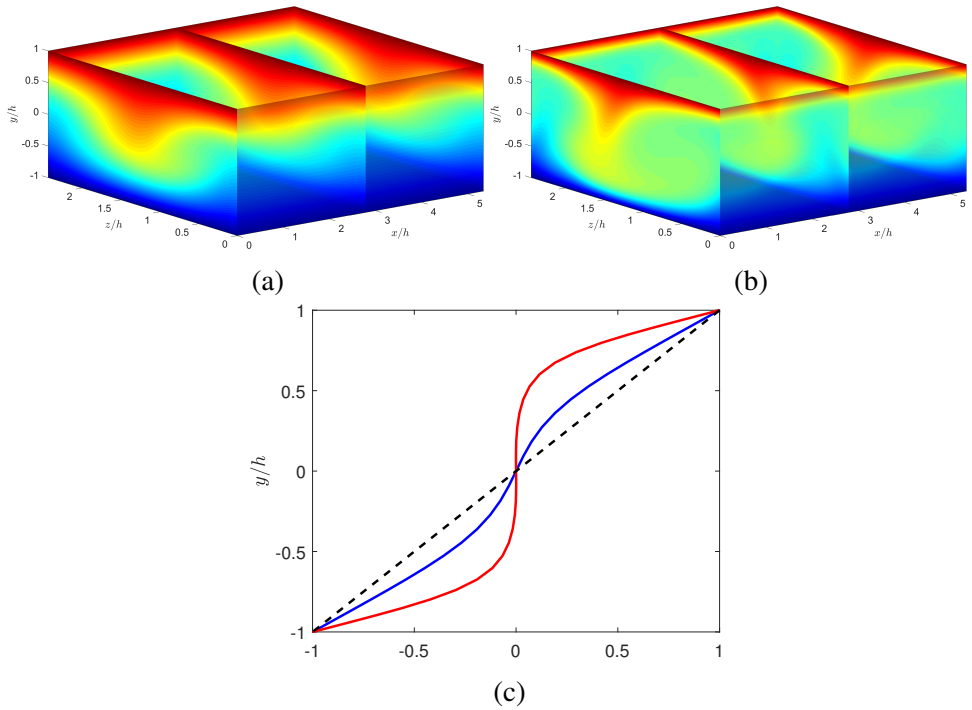

Figure 1.2: Contours of the streamwise velocity for the equilibria solutions (Couette) (a) EQ1, (b) EQ2, and (c) a comparison of their 1D mean profiles (EQ1: blue, EQ2: red) with respect to the laminar profile (dashed line). Data courtesy of J. Gibson (channelflow.org).

closely matching that of full turbulence, their vortex/streak structure also resembles many of the near-wall coherent features of turbulence. Furthermore, the periodic-orbit ECS, such as the Couette solution studied by Viswanath, 2007, have been shown to capture dynamically significant processes like the break-up and reorganization of near-wall streaks. Connections between how these solutions sustain and their asymptotic behavior at high Reynolds number via vortex-wave interactions have also been explored by Hall and Sherwin, 2010.

The computation of these solutions is typically done in minimal flow units. As a result, the solutions often represent a single structure, and thus may be viewed as 'building blocks.' It still remains to be seen how these blocks can be combined and integrated to represent the multi-scale nature of turbulence. While most of the solutions are unstable, it has been argued that turbulent trajectories may spend significant amounts of time in the neighborhood of these solutions. Notably, most of the computation of ECS has been for low to moderate Reynolds numbers, and thus its ability to represent the prominent features of high Reynolds number turbulence (Smits et al., 2011) is a subject of ongoing work.

The numerical computation of ECS often employs Newton-methods due to their quadratic convergence, though these methods require good initial guesses of the solution. Kawahara et al., 2012 outlines some common methods used to generate initial guesses, the most prominent approach being the use of (filtered) snapshots from DNS which display quasi-periodic behavior. Robust numerical tools have been developed which couple DNS solvers with Newton-based algorithms to compute ECS, one being the open-source program Channelflow developed by J. Gibson (channelflow.org) which will be utilized in this thesis.

1.3 Present approach

The statistical, structural, and dynamical relevance of ECS to fully turbulent flows has made this growing field a promising direction towards the understanding of turbulence. Without the complexity of a fully turbulent flow, while certainly retaining nonlinear behavior, ECS present a tractable path forward to make meaningful progress in the modeling of turbulent-like, yet deterministic, flows. A recent study by Sharma et al., 2016 showed the potential of the resolvent model to generate low-dimensional representations of ECS. In this thesis, we hope to expand upon this approach. In particular we wish to address some of the limitations of the current state of the art in resolvent modeling. Our aim is to develop new methods and extensions that not only improve the modeling capabilities of the resolvent framework, but also inform the creation of practical tools to compute and analyze ECS.

In addition, to augment the previous studies that have largely focused on the characteristics of the resolvent operator, we will seek to improve the current understanding of the nature of the nonlinear forcing in wall-bounded turbulent flows. While some of the previously mentioned studies (Moarref et al., 2014; Zare et al., 2017) have inferred certain properties of the forcing via optimization, to our knowledge a direct characterization of the nonlinear forcing in turbulent channel flow has not been performed. In this thesis, we will utilize a constant time-step DNS of a low-Reynolds number channel to compute, amongst other quantities of interest, spectra of the forcing terms. The use of a constant time-step, which will allow for a frequency-domain analysis, while not unprecedented (c.f. Choi and Moin, 1990, Wu et al., 2017) is not used extensively in literature and presents a unique opportunity to explore the full spectral behavior of turbulent fields.

We now outline the content and contributions of this thesis.

1.4 Thesis outline

In Chapter 2, we will provide a formal derivation of the resolvent framework in its original form (termed the 'traditional' 1D approach) before introducing a novel modification which extends the use of ideas rooted in classical linear stability analysis (namely Orr-Sommerfeld/Squire modes) into a nonlinear context. We will also augment the resolvent framework to allow for the analysis of 2D/3C flows to facilitate comparisons to the recent developments in quasilinear approaches. In Chapter 3, we will apply these new developments to the analysis of ECS solutions (equilibria, traveling waves, and periodic orbits) in a channel for both Poiseuille and Couette flows. We will demonstrate the improved characteristics obtained with the modified resolvent approach and explore the insights provided by the 2D/3C framework into how these solutions self-sustain. We will then detail how all these results can be utilized to develop resolvent-based tools to compute ECS in new ways with very limited information. In Chapter 4, we will present the spectral characterization of the nonlinear forcing from the constant time-step DNS. In addition, we will show that the ideas developed for the analysis of ECS may also be of use in fully turbulent flows. In Chapter 5, we will summarize the findings of this thesis and make suggestions for future studies.

Chapter 2

RESOLVENT FRAMEWORK

We begin with a derivation of the traditional 1D resolvent approach based on the governing NSE. Next, we introduce a novel modification to the decomposition of the resolvent operator with connections to Orr-Sommerfeld/Squire modes[1]. We also highlight the role of the nonlinear forcing term via a Helmholtz decomposition. We then detail an extension of the resolvent framework to 2D/3C flows. The section concludes with a discussion of the computation of the nonlinear term in the context of resolvent analysis, which will be used in subsequent chapters.

2.1 Resolvent formulation for a channel

We first introduce the governing equations and modeling framework, largely following the works of Schmid and Henningson, 2000; Jovanović and Bamieh, 2005; McKeon and Sharma, 2010; and Moarref et al., 2013.

2.1.1 Governing equations

We consider the non-dimensional, incompressible NSE for a Newtonian fluid in a channel

$$\begin{aligned} &\frac{\partial \mathbf{u}}{\partial t} + \mathbf{u}\cdot\nabla\mathbf{u} = -\nabla p + \frac{1}{Re_\tau}\Delta\mathbf{u} \\ &\nabla\cdot\mathbf{u} = 0. \end{aligned} \tag{2.1}$$

Here, $\mathbf{u}$ is a three-component velocity field $\mathbf{u} = [u(\mathbf{x},t), v(\mathbf{x},t), w(\mathbf{x},t)]^T$ and $p(\mathbf{x},t)$ is the pressure, each a function of three spatial dimensions $\mathbf{x} = (x, y, z)$ and time t. The streamwise (x) and spanwise (z) directions are infinite in extent, and the wall-normal (y) domain extends from $y/h = -1$ to $y/h = 1$ (where h is the channel half-height), as illustrated in Figure 2.1, with no-slip and no-penetration conditions imposed at the wall. The gradient operator is given by $\nabla = [\partial_x, \partial_y, \partial_z]^T$ and $\Delta = \nabla\cdot\nabla$ is the Laplacian operator. The friction Reynolds number is $Re_\tau = \frac{hu_\tau}{\nu}$, where $u_\tau = \sqrt{\frac{\langle\tau_w\rangle}{\rho}}$ is the friction velocity, $\langle\tau_w\rangle$ is the mean wall shear stress (with $\langle\ \rangle$ denoting an average over x, z, and t), ρ is the density, and ν is the kinematic

[1] Portions of the first two sections have been published as a part of Rosenberg and McKeon, 2018, notably the introduction of the OS/SQ decomposition of the velocity field and the Helmholtz decomposition of the forcing term.

Figure 2.1: A schematic of the flow domain and the associated coordinate system.

viscosity. The velocity is non-dimensionalized by u_τ, time by $\frac{h}{u_\tau}$, spatial variables by h, and pressure by $\rho {u_\tau}^2$. Instances where the viscous length-scale $\frac{u_\tau}{\nu}$ is used for non-dimensionalization (the so-called inner units) will be denoted by the superscript $^+$. For computational purposes, the streamwise and spanwise directions will be of finite length L_x and L_z respectively with periodic boundary conditions imposed to mimic the infinite domain. We will consider both pressure-driven flow in a channel (Poiseuille) and flow driven by the motion of the walls (Couette).

Due to the spatial invariance in the streamwise and spanwise directions, and statistical stationarity (or explicit time-periodicity), the velocity and pressure fields are expressed as Fourier modes in these directions,

$$\begin{bmatrix} \mathbf{u}(x,y,z,t) \\ p(x,y,z,t) \end{bmatrix} = \iiint_{-\infty}^{\infty} \begin{bmatrix} \hat{\mathbf{u}}(\mathbf{k};y) \\ \hat{p}(\mathbf{k};y) \end{bmatrix} e^{i(k_x x + k_z z - \omega t)} \mathrm{d}k_x \mathrm{d}k_z \mathrm{d}\omega \tag{2.2}$$

where k_x is the streamwise wavenumber, k_z is the spanwise wavenumber, ω is the radial frequency, and the wavenumber/frequency triplet is denoted by $\mathbf{k} = (k_x, k_z, \omega)$. The mean velocity is given by $\hat{\mathbf{u}}(\mathbf{k} = \mathbf{0}; y) = \mathbf{U}(y) = [U(y), 0, 0]^T$. Substituting this decomposition into the NSE yields the following equations for the fluctuations (i.e., $\mathbf{k} \neq \mathbf{0}$),

$$\begin{cases} \left[-i\omega + ik_x U\right]\hat{u} + \hat{v}U_y + ik_x\hat{p} - \frac{1}{Re_\tau}\Delta\hat{u} = \hat{f_u} \\ \left[-i\omega + ik_x U\right]\hat{v} + \hat{p}_y - \frac{1}{Re_\tau}\Delta\hat{v} = \hat{f_v} \\ \left[-i\omega + ik_x U\right]\hat{w} + ik_z\hat{p} - \frac{1}{Re_\tau}\Delta\hat{w} = \hat{f_w} \\ ik_x\hat{u} + \hat{v}_y + ik_z\hat{w} = 0, \end{cases} \tag{2.3}$$

where the subscript $_y$ denotes differentiation with respect to the wall-normal direction. Here, $\hat{\mathbf{f}} = \left(\hat{f_u}, \hat{f_v}, \hat{f_w}\right)^T = -\left(\mathbf{u}' \cdot \nabla\mathbf{u}'\right)_{\mathbf{k}}$ is the Fourier-transformed nonlinear forcing term where $\mathbf{u}' = \mathbf{u} - \mathbf{U}$. The mean velocity $U(y)$ is governed by the corre-

sponding mean-momentum equation

$$-\frac{\partial\langle p\rangle}{\partial x}+\frac{1}{Re_\tau}\frac{d^2U}{dy^2}=\langle f_u\rangle \tag{2.4}$$

where the mean u-forcing is given by the wall-normal derivative of the Reynolds stress term

$$\langle f_u\rangle=-\frac{d\langle uv\rangle}{dy}. \tag{2.5}$$

For incompressible flows, the pressure term can be eliminated, and the governing equations can be written in terms of the fluctuating vertical velocity $\hat{v}$ and normal vorticity $\hat{\eta}=ik_z\hat{u}-ik_x\hat{w}$,

$$-i\omega\begin{pmatrix}k^2-\mathcal{D}^2 & 0\\ 0 & 1\end{pmatrix}\begin{pmatrix}\hat{v}\\ \hat{\eta}\end{pmatrix}+\begin{pmatrix}\mathcal{L}_{OS} & 0\\ ik_zU_y & \mathcal{L}_{SQ}\end{pmatrix}\begin{pmatrix}\hat{v}\\ \hat{\eta}\end{pmatrix}=B\hat{\mathbf{f}} \tag{2.6}$$

where the Orr-Sommerfeld (OS) and Squire (SQ) operators are given by

$$\begin{aligned}\mathcal{L}_{OS}&=ik_xU(k^2-\mathcal{D}^2)+ik_xU_{yy}+\frac{1}{Re_\tau}(k^2-\mathcal{D}^2)^2\\ \mathcal{L}_{SQ}&=ik_xU+\frac{1}{Re_\tau}(k^2-\mathcal{D}^2),\end{aligned} \tag{2.7}$$

and the forcing operator is

$$B=\begin{pmatrix}-ik_x\mathcal{D} & -k^2 & -ik_z\mathcal{D}\\ ik_z & 0 & -ik_x\end{pmatrix}, \tag{2.8}$$

where $\mathcal{D}=\frac{\partial}{\partial y}$ and $k^2=k_x^2+k_z^2$. For numerical implementation, the wall-normal operators are discretized with Chebyshev points using the suite developed by Weideman and Reddy, 2000.

2.1.2 Resolvent operator

Equation 2.6 can be recast into the following input/output form

$$\begin{pmatrix}\hat{v}\\ \hat{\eta}\end{pmatrix}=\mathcal{H}(\mathbf{k})\begin{pmatrix}\hat{g}_v\\ \hat{g}_\eta\end{pmatrix} \tag{2.9}$$

where the transfer function $\mathcal{H}$, henceforth referred to as the resolvent operator, is given by

$$\mathcal{H}(\mathbf{k})=(-i\omega+L_1)^{-1}, \tag{2.10}$$

where

$$L_1=M^{-1}L, \tag{2.11}$$

$$M = \begin{pmatrix} k^2 - \mathcal{D}^2 & 0 \\ 0 & 1 \end{pmatrix}, \tag{2.12}$$

$$L = \begin{pmatrix} \mathcal{L}_{OS} & 0 \\ ik_z U_y & \mathcal{L}_{SQ} \end{pmatrix}, \tag{2.13}$$

$$\begin{pmatrix} \hat{g}_v \\ \hat{g}_\eta \end{pmatrix} = M^{-1} B \hat{\mathbf{f}} = \hat{\mathbf{g}} \tag{2.14}$$

The operators are made invertible via enforcement of the boundary conditions described earlier; in the velocity/vorticity formulation, this corresponds to $\hat{v} = \frac{\partial \hat{v}}{\partial y} = \hat{\eta} = 0$ at the walls. The dimensions of $\mathcal{H}$ are $2N_y \times 2N_y$, where N_y is the number of wall-normal discretization points.

From Equation 2.9, we wish to identify high gain input/output modes from the resolvent operator with respect to a kinetic energy norm. To facilitate enforcement of an energy norm, we define the weighted inner product

$$\langle \mathbf{v}_1, \mathbf{v}_2 \rangle_E = \langle \mathbf{v}_1, \mathcal{M} \mathbf{v}_2 \rangle \tag{2.15}$$

where $\mathcal{M} = \frac{1}{k^2} M$ such that for the velocity/vorticity state $\boldsymbol{\varphi} = \begin{pmatrix} \hat{v} \\ \hat{\eta} \end{pmatrix}$,

$$\langle \boldsymbol{\varphi}, \boldsymbol{\varphi} \rangle_E = \int_{-1}^{1} \boldsymbol{\varphi}^* \mathcal{M} \boldsymbol{\varphi} \mathrm{d}y \tag{2.16}$$

is proportional to the kinetic energy of the Fourier mode (Butler and Farrell, 1992). Here, * denotes the complex conjugate. We can approximate this integral numerically and express equation 2.16 and the associated inner product as

$$\langle \boldsymbol{\varphi}, \boldsymbol{\varphi} \rangle_W = \boldsymbol{\varphi}^* W \boldsymbol{\varphi} \tag{2.17}$$

where the weight matrix W is an augmented version of $\mathcal{M}$ that incorporates numerical quadrature points. W can subsequently be factored as $W = Q^* Q$ and it can be shown that for an operator A, the energy norm of A is equivalent to the 2-norm of QAQ^{-1} (Reddy et al., 1993). Returning to the resolvent operator, we introduce a scaled version of Equation 2.9

$$Q \begin{pmatrix} \hat{v} \\ \hat{\eta} \end{pmatrix} = \{ Q \mathcal{H}(\mathbf{k}) Q^{-1} \} Q \begin{pmatrix} \hat{g}_v \\ \hat{g}_\eta \end{pmatrix} \tag{2.18}$$

or

$$Q \begin{pmatrix} \hat{v} \\ \hat{\eta} \end{pmatrix} = \mathcal{H}_s(\mathbf{k}) Q \begin{pmatrix} \hat{g}_v \\ \hat{g}_\eta \end{pmatrix}, \tag{2.19}$$

where $||H_s(\mathbf{k})||_2$ has the desired energy norm. A low order basis in the inhomogeneous wall-normal direction for the velocity/vorticity fields is obtained by considering a SVD of the scaled resolvent operator,

$$\mathcal{H}_s(\mathbf{k}) = \Psi\Sigma\Phi^H \tag{2.20}$$

where Φ contains an ordered set of orthogonal input modes $\left\{ \hat{\phi}'_1(y) \quad \hat{\phi}'_2(y) \quad \cdots \quad \hat{\phi}'_n(y) \right\}$, Ψ contains an ordered set of orthogonal response modes $\left\{ \hat{\psi}'_1(y) \quad \hat{\psi}'_2(y) \quad \cdots \quad \hat{\psi}'_n(y) \right\}$, and Σ contains the corresponding singular values $\left\{ \sigma_1 \quad \sigma_2 \quad \cdots \quad \sigma_n \right\}$, i.e. the gains between input/response pairs, where $\sigma_1 \geq \sigma_2 \geq \cdots \sigma_n$ and σ^2 is proportional to the energy of the Fourier mode. The input and response modes are orthogonal with respect to the inner product defined in Equation 2.17 such that

$$\langle \hat{\phi}_i(\mathbf{k}), \hat{\phi}_j(\mathbf{k}) \rangle_W = \langle \hat{\psi}_i(\mathbf{k}), \hat{\psi}_j(\mathbf{k}) \rangle_W = \delta_{ij}, \tag{2.21}$$

where $\hat{\psi} = Q^{-1}\hat{\psi}'$ and $\hat{\phi} = Q^{-1}\hat{\phi}'$. With this decomposition, we can approximate the velocity/vorticity field as a finite sum of weighted response modes,

$$\begin{pmatrix} \hat{v}(\mathbf{k}; y) \\ \hat{\eta}(\mathbf{k}; y) \end{pmatrix} \approx \sum_{j=1}^{N} \sigma_j(\mathbf{k}) \chi_j(\mathbf{k}) \hat{\psi}_j(\mathbf{k}; y) \tag{2.22}$$

where the weight χ_j represents the projection of the nonlinear forcing onto the j^{th} input mode

$$\chi_j(\mathbf{k}) = \langle \hat{\mathbf{g}}(\mathbf{k}), \hat{\phi}_j(\mathbf{k}) \rangle_W. \tag{2.23}$$

The wall-parallel velocity components are recovered from the relationship

$$\begin{pmatrix} \hat{u} \\ \hat{v} \\ \hat{w} \end{pmatrix} = C \begin{pmatrix} \hat{v} \\ \hat{\eta} \end{pmatrix}, \tag{2.24}$$

where

$$C = \frac{1}{k^2} \begin{pmatrix} ik_x \frac{\partial}{\partial y} & -ik_z \\ k^2 & 0 \\ ik_z \frac{\partial}{\partial y} & ik_x \end{pmatrix} \tag{2.25}$$

We will demonstrate in §3.1 the ability and shortcomings of the basis in Equation 2.22 to represent ECS solutions. We now introduce a modified approach which exploits the structure of the resolvent operator to further elucidate the underlying input/output relationships.

2.2 A new approach with connections to Orr-Sommerfeld/Squire modes

Expanding Equation 2.10 symbolically using the inverse of a 2×2 block matrix, we have

$$\begin{pmatrix} \hat{v} \\ \hat{\eta} \end{pmatrix} = \begin{pmatrix} \mathcal{H}_{vv} & 0 \\ \mathcal{H}_{\eta v} & \mathcal{H}_{\eta\eta} \end{pmatrix} \begin{pmatrix} \hat{g}_v \\ \hat{g}_\eta \end{pmatrix}, \tag{2.26}$$

where

$$\begin{aligned} \mathcal{H}_{vv} &= \left(-i\omega + (k^2 - \mathcal{D}^2)^{-1}\mathcal{L}_{OS}\right)^{-1} \\ \mathcal{H}_{\eta\eta} &= \left(-i\omega + \mathcal{L}_{SQ}\right)^{-1} \\ \mathcal{H}_{\eta v} &= -ik_z \mathcal{H}_{\eta\eta} U' \mathcal{H}_{vv}. \end{aligned} \tag{2.27}$$

Notably there is a lack of coupling between $\hat{v}$ and $\hat{g}_\eta$; this is a direct consequence of the lack of coupling in the OS/SQ operator L in Equation 2.13. As a result, we can leverage this decoupling and express Equation 2.26 as

$$\begin{pmatrix} \hat{v} \\ \hat{\eta} \end{pmatrix} = \begin{pmatrix} \hat{v} \\ \hat{\eta}_{\text{os}} \end{pmatrix} + \begin{pmatrix} 0 \\ \hat{\eta}_{\text{sq}} \end{pmatrix}, \tag{2.28}$$

where

$$\begin{aligned} \begin{pmatrix} \hat{v} \\ \hat{\eta}_{\text{os}} \end{pmatrix} &= \begin{pmatrix} \mathcal{H}_{vv} & 0 \\ \mathcal{H}_{\eta v} & 0 \end{pmatrix} \begin{pmatrix} \hat{g}_v \\ 0 \end{pmatrix} \\ \begin{pmatrix} 0 \\ \hat{\eta}_{\text{sq}} \end{pmatrix} &= \begin{pmatrix} 0 & 0 \\ 0 & \mathcal{H}_{\eta\eta} \end{pmatrix} \begin{pmatrix} 0 \\ \hat{g}_\eta \end{pmatrix} \end{aligned} \tag{2.29}$$

Thus, in an analogous manner to the classical OS/SQ equations from linear stability analysis, we can decompose the normal velocity/vorticity field into a component exclusively driven by $\hat{g}_v$ (termed the OS mode) and a component (vorticity only) driven exclusively by $\hat{g}_\eta$ (termed the SQ mode). Furthermore, $\hat{\eta}_{\text{os}}$ can be interpreted as generated by $\hat{v}$ since

$$\begin{aligned} \hat{\eta}_{\text{os}} &= \mathcal{H}_{v\eta}\hat{g}_v \\ &= -ik_z \mathcal{H}_{\eta\eta} U_y \{\mathcal{H}_{vv}\hat{g}_v\} \\ &= -ik_z \mathcal{H}_{\eta\eta} U_y \hat{v}. \end{aligned} \tag{2.30}$$

If we define the corresponding (scaled) operators and their SVDs,

$$\begin{aligned} \mathcal{H}_{\text{os}} &= Q \begin{pmatrix} \mathcal{H}_{vv} & 0 \\ \mathcal{H}_{\eta v} & 0 \end{pmatrix} Q^{-1} = \Psi_{\text{os}} \Sigma_{\text{os}} \Phi_{\text{os}}^H \\ \mathcal{H}_{\text{sq}} &= Q \begin{pmatrix} 0 & 0 \\ 0 & \mathcal{H}_{\eta\eta} \end{pmatrix} Q^{-1} = \Psi_{\text{sq}} \Sigma_{\text{sq}} \Phi_{\text{sq}}^H, \end{aligned} \tag{2.31}$$

we can again approximate the fields as

$$\begin{aligned}\begin{pmatrix} \hat{v}(\mathbf{k};y) \\ \hat{\eta}_{\mathrm{os}}(\mathbf{k};y) \end{pmatrix} &\approx \sum_{j=1}^{N} \sigma_{\mathrm{os}_j}(\mathbf{k})\chi_{\mathrm{os}_j}(\mathbf{k})\hat{\psi}_{\mathrm{os}_j}(\mathbf{k};y) \\ \begin{pmatrix} 0 \\ \hat{\eta}_{\mathrm{sq}}(\mathbf{k};y) \end{pmatrix} &\approx \sum_{j=1}^{N} \sigma_{\mathrm{sq}_j}(\mathbf{k})\chi_{\mathrm{sq}_j}(\mathbf{k})\hat{\psi}_{\mathrm{sq}_j}(\mathbf{k};y),\end{aligned} \tag{2.32}$$

where the respective weights are

$$\begin{aligned}\chi_{\mathrm{os}_j}(\mathbf{k}) &= \langle \hat{\mathbf{g}}(\mathbf{k}), \hat{\phi}_{\mathrm{os}_j}(\mathbf{k}) \rangle_W \\ \chi_{\mathrm{sq}_j}(\mathbf{k}) &= \langle \hat{\mathbf{g}}(\mathbf{k}), \hat{\phi}_{\mathrm{sq}_j}(\mathbf{k}) \rangle_W\end{aligned} \tag{2.33}$$

It is not immediately obvious that such a decomposition of the velocity/vorticity fields into their OS and SQ components would have any benefit in terms of low-dimensional representation of solutions; however, we will demonstrate in §3.1 the power of such an approach. We do note, in light of this decomposition, that by expanding the energy norm definition in Equation 2.16 for just the vorticity terms we have

$$\frac{1}{k^2}\int_{-1}^{1} \hat{\eta}^*\hat{\eta}\mathrm{d}y = \frac{1}{k^2}\left\{\int_{-1}^{1} \hat{\eta}_{\mathrm{os}}^*\hat{\eta}_{\mathrm{os}}\mathrm{d}y + \int_{-1}^{1} \hat{\eta}_{\mathrm{sq}}^*\hat{\eta}_{\mathrm{sq}}\mathrm{d}y + \int_{-1}^{1} \hat{\eta}_{\mathrm{os}}^*\hat{\eta}_{\mathrm{sq}}\mathrm{d}y + \int_{-1}^{1} \hat{\eta}_{\mathrm{sq}}^*\hat{\eta}_{\mathrm{os}}\mathrm{d}y\right\}. \tag{2.34}$$

Thus one interpretation of what this decomposition provides is an extra degree of freedom to control the relative phase between the OS and SQ modes (and hence manipulate the contribution of the last two terms), an option not available and potentially unfavorably constrained when only using a single SVD of the resolvent operator.

We now explore in more detail the nonlinear forcing components $\hat{\mathbf{g}}$ that arise in the velocity/vorticity formulation of the governing equations and if they have a meaningful physical interpretation.

2.2.1 Forcing decomposition

We consider a Helmholtz decomposition of the nonlinear forcing term into the sum of an irrotational component and a solenoidal component,

$$\mathbf{f} = -\mathbf{u}\cdot\nabla\mathbf{u} = \nabla\xi + \nabla\times\zeta = \mathbf{f}_i + \mathbf{f}_s = \begin{pmatrix} f_{u_i} \\ f_{v_i} \\ f_{w_i} \end{pmatrix} + \begin{pmatrix} f_{u_s} \\ f_{v_s} \\ f_{w_s} \end{pmatrix} \tag{2.35}$$

This decomposition requires a constraint to make it unique; here we choose $\nabla\cdot\zeta = 0$. Orthogonality between the irrotational and solenoidal fields manifests itself as

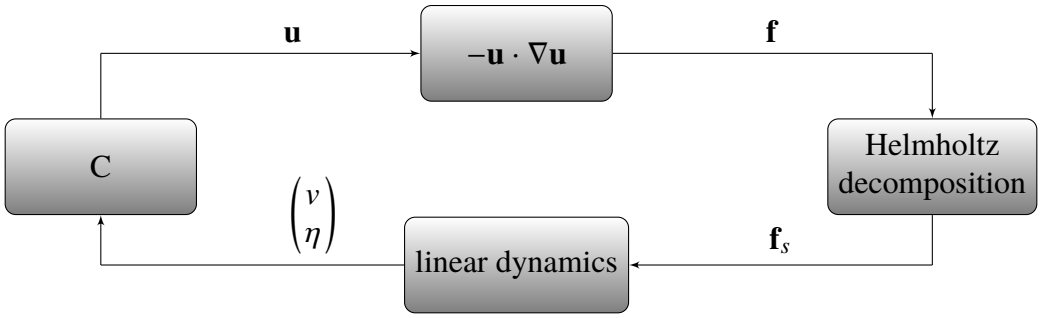

Figure 2.2: A block diagram representation of the NSE, adapted from McKeon et al., 2013. The Helmholtz decomposition of the nonlinear forcing term illustrates how only the solenoidal component drives the velocity/vorticity fluctuations.

enforcing homogeneous Dirichlet boundary conditions on f_{v_s} (Wu et al., 2007). This type of decomposition of the nonlinear term has previously been explored (Wu et al., 1996; Perot and Moin, 1996). Substituting Equation 2.35 back into the NSE yields

$$\frac{\partial \mathbf{u}}{\partial t} - \mathbf{f}_s = -\nabla \tilde{p} + \frac{1}{Re_\tau}\nabla^2 \mathbf{u} \tag{2.36}$$

where we have absorbed the irrotational part of the nonlinear forcing into a modified pressure term $\tilde{p} = p - \xi$. As before, we can eliminate $\tilde{p}$ (and hence the irrotational forcing) and write this (Fourier-transformed) equation in terms of $\hat{v}$ and $\hat{\eta}$ as

$$-i\omega \begin{pmatrix} \hat{v} \\ \hat{\eta} \end{pmatrix} + \begin{pmatrix} \left(k^2 - \mathcal{D}^2\right)^{-1} & 0 \\ 0 & 1 \end{pmatrix} \begin{pmatrix} \mathcal{L}_{OS} & 0 \\ ik_z U_y & \mathcal{L}_{SQ} \end{pmatrix} \begin{pmatrix} \hat{v} \\ \hat{\eta} \end{pmatrix} = \begin{pmatrix} \hat{f}_{v_s} \\ \hat{f}_{\eta_s} \end{pmatrix}, \tag{2.37}$$

where $\hat{f}_{\eta_s} = ik_z \hat{f}_{u_s} - ik_x \hat{f}_{w_s}$. Comparing Equation 2.37 with Equation 2.6 (multiplied by M^{-1}), it is immediately evident that the expression for the nonlinear forcing components in the velocity/vorticity formulation greatly simplify to

$$\begin{pmatrix} \hat{g}_v \\ \hat{g}_\eta \end{pmatrix} = M^{-1} B \hat{\mathbf{f}} = \begin{pmatrix} \hat{f}_{v_s} \\ \hat{f}_{\eta_s} \end{pmatrix}. \tag{2.38}$$

Therefore, a consequence of removing the pressure is that only the solenoidal components of the nonlinear forcing are 'active' in driving the velocity/vorticity fluctuations. From the relation in Equation 2.38 and Equation 2.29, $\hat{f}_{v_s}$ drives the OS components, and $\hat{f}_{\eta_s}$ drives the SQ components. We illustrate these ideas with the block diagram shown in Figure 2.2.

2.3 2D/3C resolvent formulation

Motivated by previous work analyzing the emergence of streamwise-constant streaks, the scale interactions which give rise to them, and their connections to the self-sustaining process of turbulent shear flows (Waleffe, 1997; Hall and Sherwin, 2010;

Farrell and Ioannou, 2012; Thomas et al., 2014), we augment our current framework to study these ideas through a resolvent lens. We express the velocity and pressure fields as Fourier modes in the streamwise direction and in time

$$\begin{bmatrix} \mathbf{u}(x,y,z,t) \\ p(x,y,z,t) \end{bmatrix} = \iint_{-\infty}^{\infty} \begin{bmatrix} \hat{\mathbf{u}}(k_x,\omega;y,z) \\ \hat{p}(k_x,\omega;y,z) \end{bmatrix} e^{i(k_x x-\omega t)} \mathrm{d}k_x \mathrm{d}\omega \tag{2.39}$$

where the corresponding two-dimensional, three component (2D/3C) mean velocity field is given by $\hat{\mathbf{u}}(k_x = \omega = 0; y, z) = [U(y,z), V(y,z), W(y,z)]^T$. Substituting Equation 2.39 into the NSE yields the following set of equations for the fluctuations:

$$\begin{cases} \left[-i\omega + ik_x U + \frac{k_x^2}{Re_\tau}\right]\hat{u} + U_y\hat{v} + U_z\hat{w} + ik_x\hat{p} + V\hat{u}_y + W\hat{u}_z - \frac{1}{Re_\tau}\left[\hat{u}_{yy} + \hat{u}_{zz}\right] = \hat{f}_u \\ \left[-i\omega + ik_x U + \frac{k_x^2}{Re_\tau} + V_y\right]\hat{v} + V_z\hat{w} + \hat{p}_y + V\hat{v}_y + W\hat{v}_z - \frac{1}{Re_\tau}\left[\hat{v}_{yy} + \hat{v}_{zz}\right] = \hat{f}_v \\ \left[-i\omega + ik_x U + \frac{k_x^2}{Re_\tau} + W_z\right]\hat{w} + W_y\hat{v} + \hat{p}_z + V\hat{w}_y + W\hat{w}_z - \frac{1}{Re_\tau}\left[\hat{w}_{yy} + \hat{w}_{zz}\right] = \hat{f}_w \\ ik_x\hat{u} + \hat{v}_y + \hat{w}_z = 0. \end{cases} \tag{2.40}$$

The corresponding mean momentum equations are

$$\begin{cases} VU_y + WU_z + \frac{\partial\langle p\rangle}{\partial x} - \frac{1}{Re_\tau}\left(U_{yy} + U_{zz}\right) = \langle f_u\rangle \\ VV_y + WV_z + \frac{\partial\langle p\rangle}{\partial y} - \frac{1}{Re_\tau}\left(V_{yy} + V_{zz}\right) = \langle f_v\rangle \\ VW_y + WW_z + \frac{\partial\langle p\rangle}{\partial z} - \frac{1}{Re_\tau}\left(W_{yy} + W_{zz}\right) = \langle f_w\rangle \\ V_y + W_z = 0, \end{cases} \tag{2.41}$$

with $\langle\ \rangle$ denoting an average over x and t. The mean forcing components expressed in terms of the Reynolds stresses are

$$\begin{cases} \langle f_u\rangle = -\frac{\partial\langle uv\rangle}{\partial y} - \frac{\partial\langle uw\rangle}{\partial z} \\ \langle f_v\rangle = -\frac{\partial\langle vv\rangle}{\partial y} - \frac{\partial\langle vw\rangle}{\partial z} \\ \langle f_w\rangle = -\frac{\partial\langle vw\rangle}{\partial y} - \frac{\partial\langle ww\rangle}{\partial z}. \end{cases} \tag{2.42}$$

Notably, from Equation 2.41, the mean V and W momentum equations are decoupled from the mean U momentum equation. From the mean continuity equation, we can define the streamfunction Ψ such that

$$V = -\Psi_z, \quad W = \Psi_y. \tag{2.43}$$

Consequently, we can recast the mean momentum equations as

$$\begin{aligned} &\Psi_z\left[\Psi_{yyy} + \Psi_{yzz}\right] - \Psi_y\left[\Psi_{zzz} + \Psi_{yyz}\right] + \frac{1}{Re_\tau}\left[\Psi_{yyyy} + \Psi_{zzzz} + 2\Psi_{yyzz}\right] \\ &= \langle f_v\rangle_z - \langle f_w\rangle_y, \end{aligned} \tag{2.44}$$

$$-\Psi_z U_y + \Psi_y U_z + \frac{\partial \langle p \rangle}{\partial x} - \frac{1}{Re_\tau}\left(U_{yy} + U_{zz}\right) = \langle f_u \rangle. \tag{2.45}$$

Thus, the solution to the mean momentum equations amounts to first solving a nonlinear equation for Ψ and using this result to solve a linear equation for U. Returning to the equations for the fluctuations, we can, as before, eliminate the pressure and express the equations in terms of the fluctuating vertical velocity $\hat{v}$ and normal vorticity $\hat{\eta} = \hat{u}_z - ik_x\hat{w}$. Following the notation of Farrell and Ioannou, 2012, we define $\Delta = \partial_{yy}^2 + \partial_{zz}^2 - k_x^2$, $\Delta_2 = \partial_{zz}^2 - k_x^2$ and express the governing equations as

$$-i\omega \begin{pmatrix} -\Delta & 0 \\ 0 & 1 \end{pmatrix} \begin{pmatrix} \hat{v} \\ \hat{\eta} \end{pmatrix} + \begin{pmatrix} \mathcal{L}_{OS}^{2D} & \mathcal{L}_{C_1} \\ \mathcal{L}_{C_2} & \mathcal{L}_{SQ}^{2D} \end{pmatrix} \begin{pmatrix} \hat{v} \\ \hat{\eta} \end{pmatrix} = B\hat{\mathbf{f}} \tag{2.46}$$

where

$$\begin{aligned} \mathcal{L}_{OS}^{2D} = {} & ik_x U\Delta + ik_x U_{zz} + 2ik_x U_z\partial_z - ik_x U_{yy} + 2ik_x U_z\partial_{yyz}^3\Delta_2^{-1} + 2ik_x U_{yz}\partial_{yz}^2\Delta_2^{-1} \\ & - \frac{1}{Re_\tau}\Delta^2 - \left(\Psi_{yyz} + \Psi_{zzz}\right)\partial_y + 2\left(\Psi_{yyz} + \Psi_{zzz}\right)\partial_{yzz}^3\Delta_2^{-1} - \left(\Psi_{yyy} + \Psi_{yzz}\right)\partial_z \\ & - 2\Psi_{zz}\partial_{yyz}^3\Delta_2^{-1} + 2\Psi_{yz}\partial_{yzz}^3\Delta_2^{-1} - \Psi_z\Delta\partial_y - 2\Psi_{zz}\partial_{yz}^2 - \Psi_{yyyz} - \Psi_{yzzz} - \Psi_{yz}\Delta \\ & + \Psi_{yyy}\partial_z\Delta + 2\Psi_{yz}\partial_{zz}^2 + \Psi_{yyzz}\partial_{yz}^2\Delta_2^{-1} + \Psi_{zzzz}\partial_{yz}^2\Delta_2^{-1} + \Psi_{zz}\partial_{yz}^2\Delta\Delta_2^{-1} \end{aligned} \tag{2.47}$$

$$\begin{aligned} \mathcal{L}_{C_1} = {} & -2k_x^2 U_z\partial_y\Delta_2^{-1} - 2k_x^2 U_{yz}\Delta_2^{-1} + 2ik_x\left(\Psi_{yyz} + \Psi_{zzz}\right)\partial_z\Delta_2^{-1} - 2ik_x\Psi_{zz}\partial_{yy}^2\Delta_2^{-1} \\ & + 2ik_x\Psi_{yz}\partial_{yz}^2\Delta_2^{-1} + ik_x\Psi_{yyzz}\Delta_2^{-1} + ik_x\Psi_{zzzz}\Delta_2^{-1} + ik_x\Psi_{zz}\Delta\Delta_2^{-1} \end{aligned} \tag{2.48}$$

$$\mathcal{L}_{C_2} = -U_z\partial_y + U_{yz} + U_y\partial_z - U_{zz}\partial_{yz}^2\Delta_2^{-1} + ik_x\Psi_{yyzz}\partial_{yy}^2\Delta_2^{-1} \tag{2.49}$$

$$\mathcal{L}_{SQ}^{2D} = ik_x U - ik_x U_{zz}\Delta_2^{-1} + \Psi_{yz} - \Psi_z\partial_y + \Psi_y\partial_z - \Psi_{zz}\partial_{yz}^2\Delta_2^{-1} - \frac{1}{Re_\tau}\Delta \tag{2.50}$$

$$B^{2D} = \begin{pmatrix} -ik_x\partial_y & \Delta_2 & -\partial_{yz}^2 \\ \partial_z & 0 & -ik_x \end{pmatrix}. \tag{2.51}$$

The corresponding OS and SQ operators are significantly more complicated for the 2D/3C case; it should be noted that when $V(y,z) = W(y,z) = 0$ and $U(y,z) = U(y)$, the operators reduce down to the standard form found in Equation 2.7. It should also be emphasized that terms involving Ψ are often neglected (Farrell and Ioannou, 2012; Schmid and Henningson, 2000) based on the assumption that $U(y,z) \gg V(y,z), W(y,z)$; here, no such assumption is invoked. Equation 2.46 is recast into the input/output form

$$\begin{pmatrix} \hat{v} \\ \hat{\eta} \end{pmatrix} = \mathcal{H}^{2D}(k_x,\omega) \begin{pmatrix} \hat{g}_v \\ \hat{g}_\eta \end{pmatrix} \tag{2.52}$$

where the resolvent operator is given by

$$\mathcal{H}^{2D}(k_x, \omega) = (-i\omega + {L_1}^{2D})^{-1}, \tag{2.53}$$

where

$$L_1^{2D} = \left[M^{2D}\right]^{-1} L^{2D}, \tag{2.54}$$

$$M^{2D} = \begin{pmatrix} -\Delta & 0 \\ 0 & 1 \end{pmatrix}, \tag{2.55}$$

$$L^{2D} = \begin{pmatrix} \mathcal{L}_{OS}^{2D} & \mathcal{L}_{C_1} \\ \mathcal{L}_{C_2} & \mathcal{L}_{SQ}^{2D} \end{pmatrix}, \tag{2.56}$$

$$\begin{pmatrix} \hat{g}_v \\ \hat{g}_\eta \end{pmatrix} = \left[M^{2D}\right]^{-1} B\hat{\mathbf{f}} = \hat{\mathbf{g}} \tag{2.57}$$

The wall-normal operators are discretized with Chebyshev points as before; additionally, Fourier differentiation matrices (Weideman and Reddy, 2000) are used for the differential operators in the spanwise direction. The dimensions of $\mathcal{H}^{2D}$ are $2N_yN_z \times 2N_yN_z$ where N_y is the number of wall-normal discretization points and N_z is the number of discretization points in the spanwise direction. We perform a SVD of the (scaled) operator

$$\mathcal{H}_S^{2D} = Q^{2D}\mathcal{H}^{2D}\left[Q^{2D}\right]^{-1} = \Psi\Sigma\Phi^H, \tag{2.58}$$

where Q^{2D} is a weight matrix based on the analogous inner product defined in Equation 2.15 where now $\mathcal{M}^{2D} = \Delta_2^{-1}M^{2D}$. Low-dimensional representations of the velocity field are obtained as

$$\begin{pmatrix} \hat{v}(k_x, \omega; y, z) \\ \hat{\eta}(k_x, \omega; y, z) \end{pmatrix} \approx \sum_{j=1}^{N} \sigma_j(k_x, \omega)\chi_j(k_x, \omega)\hat{\psi}_j(k_x, \omega; y, z) \tag{2.59}$$

where the weight χ_j represents the projection of the nonlinear forcing onto the j^{th} input mode

$$\chi_j(k_x, \omega) = \langle \hat{\mathbf{g}}(k_x, \omega), \hat{\phi}_j(k_x, \omega)\rangle_W. \tag{2.60}$$

We demonstrate in §3.2 the utility of this formulation, particularly for lower branch ECS solutions, in representing such flows and elucidating the scale interactions that sustain them.

2.4 Nonlinear term and interaction coefficients

We briefly outline the details concerning the computation of the nonlinear forcing term. We then make connections to the nonlinear weights χ formulated in Sections §2.1 and §2.2 and express its computation in terms of the so-called interaction coefficient (Sharma and McKeon, 2013a; McKeon et al., 2013).

2.4.1 Computation of nonlinearity

Recall, for an incompressible flow field, the nonlinear term can be expressed as

$$\mathbf{u} \cdot \nabla \mathbf{u} = \nabla \cdot \left(\mathbf{u}\mathbf{u}^T \right). \tag{2.61}$$

Notably, the nonlinear term is quadratic. When we transform to the Fourier domain, this implies that we will be considering the interaction of modes that are triadically consistent, satisfying the relationship

$$\mathbf{k}_a + \mathbf{k}_b = \mathbf{k}_c. \tag{2.62}$$

We therefore can express the computation of the nonlinearity in Equation 2.61 as a convolution over triadically consistent Fourier modes

$$\hat{\mathbf{f}}(\mathbf{k}_c; y) = \sum_{\substack{\mathbf{k}_a + \mathbf{k}_b = \mathbf{k}_c \\ \mathbf{k}_a, \mathbf{k}_b \neq \mathbf{0}}} -\nabla_c \cdot \left(\hat{\mathbf{u}}(\mathbf{k}_a) \hat{\mathbf{u}}^T(\mathbf{k}_b) \right), \tag{2.63}$$

where the gradient operator is given by $\nabla_c = \left[ik_{x_c}, \frac{\partial}{\partial y}, ik_{z_c} \right]^T$. We exclude the interactions that involve the mean mode ($\mathbf{k} = 0$) as those are accounted for in the resolvent operator. As discussed in Canuto et al., 1988, the convolution sum in Equation 2.63 is not the most efficient way to calculate the nonlinear term. A less computationally expensive approach is to compute it pseudospectrally by first forming the nonlinearity in the physical domain and appropriately de-aliasing (3/2 rule) when transforming to the Fourier domain. Indeed, this approach is used to compute the nonlinear forcing for the numerical solutions studied in this thesis; however, the convolution in Equation 2.63 remains helpful in identifying particular interactions between triads. Additionally, we find it useful in the development of the interaction coefficient which we describe in the next section.

2.4.2 Interaction coefficient

We wish to connect the computation of the nonlinear forcing to the singular basis obtained from the resolvent operator. We will begin with the traditional resolvent formulation described in Section §2.1 and then extend the results to the OS/SQ framework described in §2.2.

Recall, from Equation 2.22, we can approximate the velocity of two Fourier modes

$\mathbf{k}_a$ and $\mathbf{k}_b$ as

$$\begin{cases} \hat{\mathbf{u}}(\mathbf{k}_a) \approx \sum_{p=1}^{N} \sigma_p(\mathbf{k}_a)\chi_p(\mathbf{k}_a)\tilde{\psi}_p(\mathbf{k}_a) \\ \hat{\mathbf{u}}(\mathbf{k}_b) \approx \sum_{q=1}^{N} \sigma_q(\mathbf{k}_b)\chi_q(\mathbf{k}_b)\tilde{\psi}_q(\mathbf{k}_b) \end{cases} \tag{2.64}$$

in which $\tilde{\psi} = C\hat{\psi}$, where we have used the operator C (defined in Equation 2.25, evaluated at the appropriate $\mathbf{k}$) to transform from normal velocity/vorticity $\hat{\psi} = \left[\psi_v, \psi_\eta\right]^T$ to the primitive velocity components $\tilde{\psi} = [\psi_u, \psi_v, \psi_w]^T$. Substituting Equation 2.64 into Equation 2.63 yields

$$\hat{\mathbf{f}}(\mathbf{k}_c; y) \approx \sum_{\substack{\mathbf{k}_a+\mathbf{k}_b=\mathbf{k}_c \\ \mathbf{k}_a,\mathbf{k}_b\neq\mathbf{0}}} \left\{ \sum_{p=1}^{N}\sum_{q=1}^{N} -\sigma_p(\mathbf{k}_a)\sigma_q(\mathbf{k}_b)\nabla_c \cdot \left(\tilde{\psi}_p(\mathbf{k}_a)\tilde{\psi}_q^T(\mathbf{k}_b)\right) \chi_p(\mathbf{k}_a)\chi_q(\mathbf{k}_b) \right\}. \tag{2.65}$$

Thus, we express the forcing at wavenumber $\mathbf{k}_c$ as a convolution over all triadically consistent modes $\mathbf{k}_a$ and $\mathbf{k}_b$, while simultaneously summing over N singular modes used to represent the respective velocity fields. Now, we can relate the expression in 2.65 to the weight χ using Equation 2.23

$$\begin{aligned} \chi_j(\mathbf{k}_c) &= \langle \hat{\mathbf{g}}(\mathbf{k}_c), \hat{\phi}_j(\mathbf{k}_c)\rangle_W \\ &= \langle -M_c^{-1}B_c\hat{\mathbf{f}}(\mathbf{k}_c), \hat{\phi}_j(\mathbf{k}_c)\rangle_W \\ &= \sum_{\substack{\mathbf{k}_a+\mathbf{k}_b=\mathbf{k}_c \\ \mathbf{k}_a,\mathbf{k}_b\neq\mathbf{0}}} \sum_{p=1}^{N}\sum_{q=1}^{N} \mathcal{N}_{jpq}(\mathbf{k}_a,\mathbf{k}_b)\chi_p(\mathbf{k}_a)\chi_q(\mathbf{k}_b) \end{aligned} \tag{2.66}$$

where we have used Equation 2.14 to express $\hat{\mathbf{g}}$ in term of $\hat{\mathbf{f}}$ and the interaction coefficient $\mathcal{N}$ is given by

$$\mathcal{N}_{jpq}(\mathbf{k}_a,\mathbf{k}_b) = \sigma_{a_p}\sigma_{b_q}\langle -M_c^{-1}B_c \left\{ \nabla_c \cdot \left(\tilde{\psi}_p(\mathbf{k}_a)\tilde{\psi}_q^T(\mathbf{k}_b)\right)\right\}, \hat{\phi}_j(\mathbf{k}_c)\rangle_W. \tag{2.67}$$

Notably, Equation 2.67 is only a function of the singular basis vectors, singular values, and differential operators. Thus, $\mathcal{N}$ can be computed once the basis is defined (i.e. once a mean profile $U(y)$ is specified). Consequently, from Equation 2.66, the unknown weights (across all wavenumbers and singular orders) are expressed as a large system of coupled, quadratic (algebraic) equations.

2.4.3 OS/SQ interaction coefficient

We now wish to extend the preceding formulation to the OS/SQ decomposition presented in Section §2.2. We begin by expressing the velocity field as a sum of OS

and SQ fields,

$$\mathbf{u} = \mathbf{u}_{\text{os}} + \mathbf{u}_{\text{sq}}, \tag{2.68}$$

where $\mathbf{u}_{\text{os}} = [u_{\text{os}}, v_{\text{os}}, w_{\text{os}}]^T$, $\mathbf{u}_{\text{sq}} = [u_{\text{sq}}, 0, w_{\text{sq}}]^T$. Consequently, we can express the nonlinear forcing in Equation 2.61 as the sum of four terms

$$\nabla \cdot \left(\mathbf{u}\mathbf{u}^T\right) = \nabla \cdot \left(\mathbf{u}_{\text{os}}\mathbf{u}_{\text{os}}^T\right) + \nabla \cdot \left(\mathbf{u}_{\text{sq}}\mathbf{u}_{\text{sq}}^T\right) + \nabla \cdot \left(\mathbf{u}_{\text{os}}\mathbf{u}_{\text{sq}}^T\right) + \nabla \cdot \left(\mathbf{u}_{\text{sq}}\mathbf{u}_{\text{os}}^T\right), \tag{2.69}$$

where each term can be expressed in the Fourier domain as their corresponding convolution sums:

$$\begin{cases} \hat{\mathbf{f}}^{\,\text{os/os}}(\mathbf{k}_c) = \displaystyle\sum_{\substack{\mathbf{k}_a+\mathbf{k}_b=\mathbf{k}_c \\ \mathbf{k}_a,\mathbf{k}_b\neq\mathbf{0}}} -\nabla_c \cdot \left(\hat{\mathbf{u}}_{\text{os}}(\mathbf{k}_a)\hat{\mathbf{u}}_{\text{os}}^T(\mathbf{k}_b)\right) \\ \hat{\mathbf{f}}^{\,\text{sq/sq}}(\mathbf{k}_c) = \displaystyle\sum_{\substack{\mathbf{k}_a+\mathbf{k}_b=\mathbf{k}_c \\ \mathbf{k}_a,\mathbf{k}_b\neq\mathbf{0}}} -\nabla_c \cdot \left(\hat{\mathbf{u}}_{\text{sq}}(\mathbf{k}_a)\hat{\mathbf{u}}_{\text{sq}}^T(\mathbf{k}_b)\right) \\ \hat{\mathbf{f}}^{\,\text{os/sq}}(\mathbf{k}_c) = \displaystyle\sum_{\substack{\mathbf{k}_a+\mathbf{k}_b=\mathbf{k}_c \\ \mathbf{k}_a,\mathbf{k}_b\neq\mathbf{0}}} -\nabla_c \cdot \left(\hat{\mathbf{u}}_{\text{os}}(\mathbf{k}_a)\hat{\mathbf{u}}_{\text{sq}}^T(\mathbf{k}_b)\right) \\ \hat{\mathbf{f}}^{\,\text{sq/os}}(\mathbf{k}_c) = \displaystyle\sum_{\substack{\mathbf{k}_a+\mathbf{k}_b=\mathbf{k}_c \\ \mathbf{k}_a,\mathbf{k}_b\neq\mathbf{0}}} -\nabla_c \cdot \left(\hat{\mathbf{u}}_{\text{sq}}(\mathbf{k}_a)\hat{\mathbf{u}}_{\text{os}}^T(\mathbf{k}_b)\right). \end{cases} \tag{2.70}$$

As before, we can approximate the OS and SQ velocity fields in terms of singular basis vectors using Equation 2.32,

$$\begin{cases} \hat{\mathbf{u}}_{\text{os}}(\mathbf{k}_a) \approx \displaystyle\sum_{p=1}^{N} \sigma_{\text{os}_p}(\mathbf{k}_a)\chi_{\text{os}_p}(\mathbf{k}_a)\tilde{\psi}_{\text{os}_p}(\mathbf{k}_a) \\ \hat{\mathbf{u}}_{\text{os}}(\mathbf{k}_b) \approx \displaystyle\sum_{q=1}^{N} \sigma_{\text{os}_q}(\mathbf{k}_b)\chi_{\text{os}_q}(\mathbf{k}_b)\tilde{\psi}_{\text{os}_q}(\mathbf{k}_b), \end{cases} \tag{2.71}$$

$$\begin{cases} \hat{\mathbf{u}}_{\text{sq}}(\mathbf{k}_a) \approx \displaystyle\sum_{p=1}^{N} \sigma_{\text{sq}_p}(\mathbf{k}_a)\chi_{\text{sq}_p}(\mathbf{k}_a)\tilde{\psi}_{\text{sq}_p}(\mathbf{k}_a) \\ \hat{\mathbf{u}}_{\text{sq}}(\mathbf{k}_b) \approx \displaystyle\sum_{q=1}^{N} \sigma_{\text{sq}_q}(\mathbf{k}_b)\chi_{\text{sq}_q}(\mathbf{k}_b)\tilde{\psi}_{\text{sq}_q}(\mathbf{k}_b). \end{cases} \tag{2.72}$$

Substituting Equations 2.71-2.72 into Equation 2.70 and using the definition of the weights in Equation 2.33, we obtain the following expressions:

$$\begin{aligned}\chi_{\mathrm{os}_j}(\mathbf{k}_c) = \sum_{\substack{\mathbf{k}_a+\mathbf{k}_b=\mathbf{k}_c \\ \mathbf{k}_a,\mathbf{k}_b\neq\mathbf{0}}} \sum_{p=1}^{N}\sum_{q=1}^{N} \Big\{ & \mathcal{A}^{\mathrm{os/os}}_{jpq}(\mathbf{k}_a,\mathbf{k}_b)\chi_{\mathrm{os}_p}(\mathbf{k}_a)\chi_{\mathrm{os}_q}(\mathbf{k}_b) \\ & + \mathcal{A}^{\mathrm{sQ/sQ}}_{jpq}(\mathbf{k}_a,\mathbf{k}_b)\chi_{\mathrm{sQ}_p}(\mathbf{k}_a)\chi_{\mathrm{sQ}_q}(\mathbf{k}_b) \\ & + \mathcal{A}^{\mathrm{os/sQ}}_{jpq}(\mathbf{k}_a,\mathbf{k}_b)\chi_{\mathrm{os}_p}(\mathbf{k}_a)\chi_{\mathrm{sQ}_q}(\mathbf{k}_b) \\ & + \mathcal{A}^{\mathrm{sQ/os}}_{jpq}(\mathbf{k}_a,\mathbf{k}_b)\chi_{\mathrm{sQ}_p}(\mathbf{k}_a)\chi_{\mathrm{os}_q}(\mathbf{k}_b) \Big\},\end{aligned} \tag{2.73}$$

$$\begin{aligned}\chi_{\mathrm{sQ}_j}(\mathbf{k}_c) = \sum_{\substack{\mathbf{k}_a+\mathbf{k}_b=\mathbf{k}_c \\ \mathbf{k}_a,\mathbf{k}_b\neq\mathbf{0}}} \sum_{p=1}^{N}\sum_{q=1}^{N} \Big\{ & \mathcal{B}^{\mathrm{os/os}}_{jpq}(\mathbf{k}_a,\mathbf{k}_b)\chi_{\mathrm{os}_p}(\mathbf{k}_a)\chi_{\mathrm{os}_q}(\mathbf{k}_b) \\ & + \mathcal{B}^{\mathrm{sQ/sQ}}_{jpq}(\mathbf{k}_a,\mathbf{k}_b)\chi_{\mathrm{sQ}_p}(\mathbf{k}_a)\chi_{\mathrm{sQ}_q}(\mathbf{k}_b) \\ & + \mathcal{B}^{\mathrm{os/sQ}}_{jpq}(\mathbf{k}_a,\mathbf{k}_b)\chi_{\mathrm{os}_p}(\mathbf{k}_a)\chi_{\mathrm{sQ}_q}(\mathbf{k}_b) \\ & + \mathcal{B}^{\mathrm{sQ/os}}_{jpq}(\mathbf{k}_a,\mathbf{k}_b)\chi_{\mathrm{sQ}_p}(\mathbf{k}_a)\chi_{\mathrm{os}_q}(\mathbf{k}_b) \Big\}.\end{aligned} \tag{2.74}$$

The corresponding interaction coefficients are defined in the compact form

$$\begin{aligned}\mathcal{A}^{\mathrm{XX/YY}}_{jpq}(\mathbf{k}_a,\mathbf{k}_b) &= \sigma_{\mathrm{XX}_p}(\mathbf{k}_a)\sigma_{\mathrm{YY}_q}(\mathbf{k}_b)\langle -M_c^{-1}B_c\left\{\nabla_c\cdot\left(\tilde{\psi}_{\mathrm{XX}_p}(\mathbf{k}_a)\tilde{\psi}^T_{\mathrm{YY}_q}(\mathbf{k}_b)\right)\right\},\hat{\phi}_{\mathrm{os}_j}(\mathbf{k}_c)\rangle_W \\ \mathcal{B}^{\mathrm{XX/YY}}_{jpq}(\mathbf{k}_a,\mathbf{k}_b) &= \sigma_{\mathrm{XX}_p}(\mathbf{k}_a)\sigma_{\mathrm{YY}_q}(\mathbf{k}_b)\langle -M_c^{-1}B_c\left\{\nabla_c\cdot\left(\tilde{\psi}_{\mathrm{XX}_p}(\mathbf{k}_a)\tilde{\psi}^T_{\mathrm{YY}_q}(\mathbf{k}_b)\right)\right\},\hat{\phi}_{\mathrm{sQ}_j}(\mathbf{k}_c)\rangle_W,\end{aligned} \tag{2.75}$$

where XX/YY takes on all four permutations of $\{OS, SQ\}/\{OS, SQ\}$. Comparing Equations 2.73-2.74 to 2.66, we see the introduction of a second basis (one for OS and one for SQ) results in eight interaction coefficients as opposed to just one. However, it should be emphasized that once a mean profiled is defined, each of the interaction coefficients can be computed (and in theory need only be computed once). Furthermore, we again stress that Equations 2.73-2.74 represent a system of coupled, quadratic equations in the unknown weights. In §3.3, we will leverage this simplicity (in the sense that we are dealing with quadratic algebraic equations) to develop efficient strategies for computing the weights of ECS solutions knowing only the mean velocity profile of the solution.

Chapter 3

ANALYSIS OF EXACT COHERENT STATES

We apply the tools developed in the previous chapter to the analysis of exact coherent states. In particular, we analyze traveling wave solutions in Poiseuille flow (characterized by wavespeed c^+), as well as equilibria and periodic orbits in Couette flow[1]. We first show the ability of the 1D resolvent to provide low-dimensional representations of these solutions, with emphasis on the improvement attained using the modified OS/SQ approach. We next augment these results with the insights provided by the 2D/3C resolvent framework. We then highlight the underlying scale interactions which sustain these solutions. Finally, we consolidate all these results to develop novel and efficient approaches to computing ECS solutions[2].

3.1 Low dimensional representation via 1D resolvent analysis

We begin with the traveling wave solutions of Park and Graham, 2015 before turning our attention to the equilibria/periodic orbits of Gibson et al., 2008. We summarize the relevant parameters of these solutions in Table 3.1.

Solution	Flow	L_x/h	L_z/h	N_x	N_z	N_y	c^+	Re	Re_τ
P4L	Poiseuille	π	$\pi/2$	24	24	81	25	2750	85
P4U	Poiseuille	π	$\pi/2$	24	24	81	14.2	1650	85
EQ1	Couette	1.75π	0.8π	32	32	35	0	400	24
EQ2	Couette	1.75π	0.8π	32	32	35	0	400	35
P19.02	Couette	1.75π	1.2π	32	32	49	N/A	400	35
P87.89	Couette	1.75π	1.2π	32	32	49	N/A	400	35

Table 3.1: Geometrical parameters and relevant flow properties for the various ECS solutions analyzed. Here, Re is based on the laminar centerline / wall velocity.

3.1.1 Traveling waves in Poiseuille flow

We demonstrate the efficacy of the singular modes obtained from the SVD of the resolvent operator as an efficient basis for capturing certain quantities of interest

[1] Data for the traveling wave solutions was provided by M.D. Graham and J.S. Park (Park and Graham, 2015). Couette solutions were obtained from the online database of J. Gibson (channelflow.org). Portions of the analysis of the traveling waves have been published as a part of Rosenberg and McKeon, 2018

[2] Some of the results presented in §3.3 arose via collaboration with M.A. Ahmed and A.S. Sharma, University of Southampton.

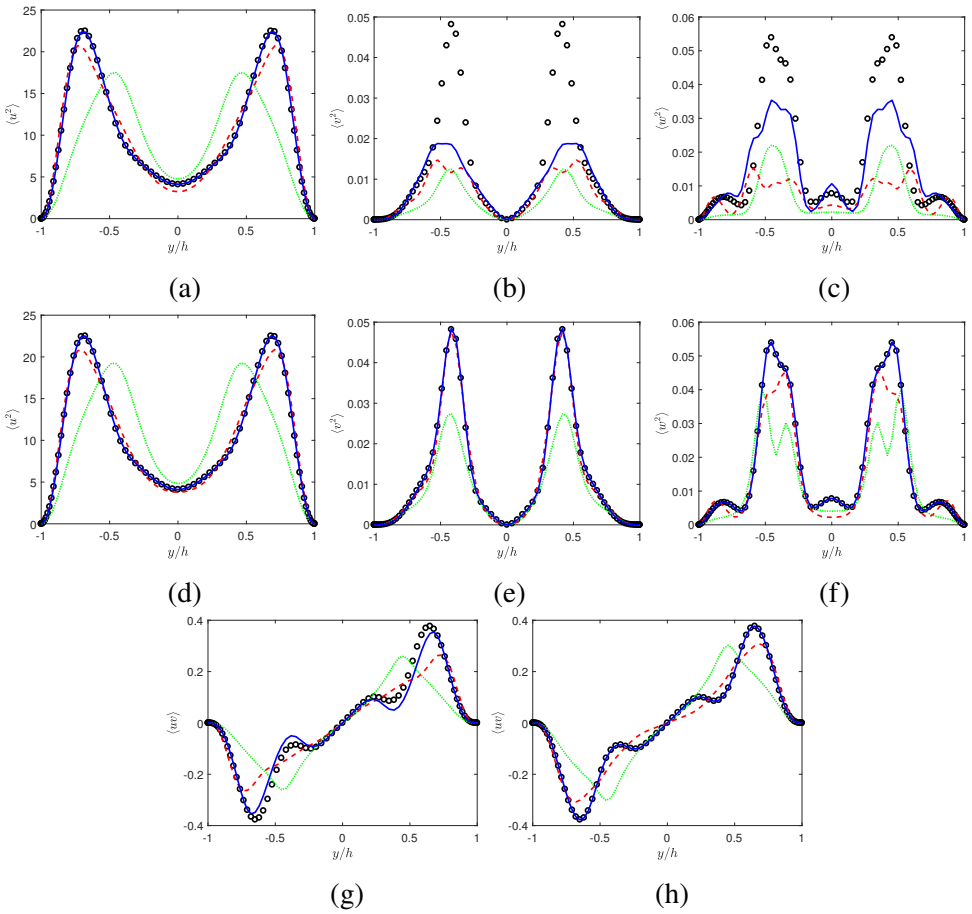

Figure 3.1: Reynolds stress profiles for P4L (open circles) and their approximations using $N_p = 1$ (dotted), $N_p = 3$ (dashed), and $N_p = 10$ (solid) singular modes for (a),(d) $\langle u^2 \rangle$, (b),(e) $\langle v^2 \rangle$, (c),(f) $\langle w^2 \rangle$, (g),(h) $\langle uv \rangle$. The top row and bottom left panel correspond to the traditional approach, and the middle row and bottom right panel correspond to the modified OS/SQ approach. All quantities are in inner units.

by projecting the P4 solutions onto these modes across all wavenumber-frequency space. We present results in terms of N_p singular pairs for the P4 solutions due to the imposed wall-normal symmetry and the fact that the SVD yields symmetric/antisymmetric pairs.

We plot the Reynolds stresses captured for increasing N_p using the expressions in Equation 2.22 for the traditional resolvent approach (Sharma et al., 2016) and Equation 2.32 in which we split the OS and SQ contributions to the velocity/vorticity. We note the latter uses twice the number of singular modes (at the same rank) as the former, except for v which only has OS contributions. Figure 3.1 shows the $\langle u^2 \rangle$, $\langle v^2 \rangle$, $\langle w^2 \rangle$, and $\langle uv \rangle$ Reynolds stresses captured for P4L. While the traditional approach captures $\langle u^2 \rangle$ quite well (and indeed $\langle u^2 \rangle$ dominates the total kinetic

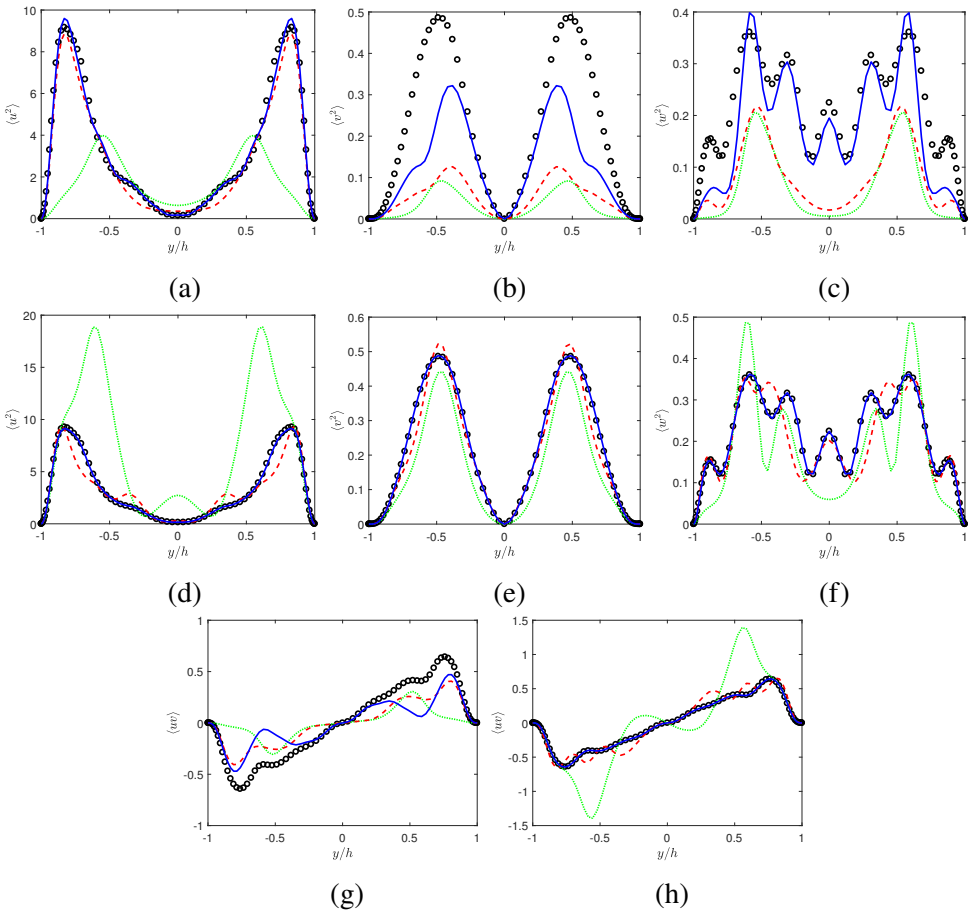

Figure 3.2: Reynolds stress profiles for P4U (open circles) and their approximations using $N_p = 1$ (dotted), $N_p = 3$ (dashed), and $N_p = 10$ (solid) singular modes for (a),(d) $\langle u^2 \rangle$, (b),(e) $\langle v^2 \rangle$, (c),(f) $\langle w^2 \rangle$, (g),(h) $\langle uv \rangle$. The top row and bottom left panel correspond to the traditional approach, and the middle row and bottom right panel correspond to the modified OS/SQ approach. All quantities are in inner units.

energy), the remaining components are not as well approximated with a small number of singular modes. In fact, even using twice the number of singular modes ($N_p = 20$) still does not yield complete convergence (see Appendix). However, with the modified OS/SQ approach, we see with as little as $N_p = 3$ singular mode pairs, $\langle u^2 \rangle$ and $\langle v^2 \rangle$ are almost completely captured, and with $N_p = 10$ all components are fully captured. The significance of the accurate low-dimensional representation of $\langle v^2 \rangle$, which was visibly lacking using the traditional approach, will be expanded upon shortly. Similarly, Figure 3.2 shows the Reynolds stresses for P4U. We again observe with the traditional approach a low-dimensional representation of $\langle u^2 \rangle$ while the remaining components converge much less rapidly. Notably, $\langle uv \rangle$ is poorly represented; this component is especially important as it acts to sustain the

mean velocity (see Equation 2.4) which is at the core of the resolvent operator. In contrast, the modified OS/SQ approach yields a rapid convergence to the true values, with a complete capturing of all components with $N_p = 10$. The large initial overshoot of the $\langle u^2 \rangle$ Reynolds stress (with simultaneous close matching of $\langle v^2 \rangle$) also suggests a potential competing effect between OS and SQ contributions to the vorticity; we will return to this notion shortly. It is interesting that despite the increased spatial complexity of the P4U solution (Park and Graham, 2015), it is still well approximated by roughly the same number of singular pairs as the P4L solution.

The new decomposition technique appears to provide not only a low-dimensional representation of the output, but also of the input forcing as well; for these coherent solutions, this is perhaps unsurprising. Figure 3.3 shows the variance of the forcing components $\langle {f_{v_s}}^2 \rangle$ and $\langle {f_{\eta_s}}^2 \rangle$ captured for the P4L and P4U solutions. The forcing requires slightly more singular modes to be fully captured, particularly for the P4U solution; however, in comparison to the solenoidal forcing captured using the previous technique (see Appendix), this approach yields a much more compact representation. We also include in the appendix a comparison of the full forcing $-\mathbf{u} \cdot \nabla \mathbf{u}$ and the solenoidal components.

3.1.2 OS/SQ contributions

It is noteworthy to further examine the OS/SQ contributions to the Reynolds stresses, in particular $\langle u^2 \rangle$ as it dominates the energy, and $\langle uv \rangle$ as it sustains the mean velocity. Following the decomposition in Equation 2.68, we can express the total variance of u as

$$\langle u^2 \rangle = \langle {u_{\text{os}}}^2 \rangle + \langle {u_{\text{sq}}}^2 \rangle + 2\langle u_{\text{os}} u_{\text{sq}} \rangle. \tag{3.1}$$

In a similar manner, we can decompose $\langle uv \rangle$ as

$$\langle uv \rangle = \langle u_{\text{os}} v \rangle + \langle u_{\text{sq}} v \rangle. \tag{3.2}$$

In Figure 3.4, we plot these contributions with respect to the full $\langle u^2 \rangle$ and $\langle uv \rangle$ for P4L and P4U. We see the P4L solution is driven almost exclusively by OS modes, which is to say that the dynamics are largely driven by $\hat{v}$. Consequently, when we return to Figure 3.1, the fact that the traditional approach captures $\langle u^2 \rangle$ so well but $\langle v^2 \rangle$ so poorly reflects its inability to do justice to the underlying dynamics. This further bolsters the superiority of the bases obtained from the OS/SQ approach to not only provide a low-order representation of the velocity field but also to

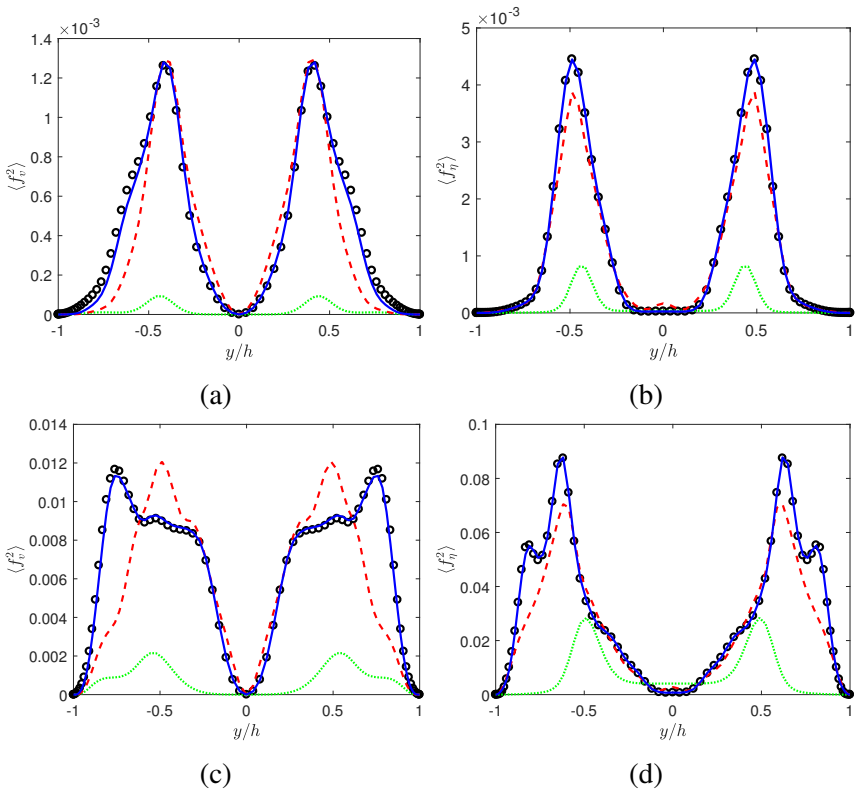

Figure 3.3: Forcing variance profiles for P4L (open circles, top row) and P4U (open circles, bottom row) and their approximations via the modified OS/SQ approach using $N_p = 1$ (dotted), $N_p = 5$ (dashed), and $N_p = 15$ (solid) singular modes for (a),(c) $\langle {f_v}^2 \rangle$, and (b),(d) $\langle {f_\eta}^2 \rangle$. All quantities are in inner units.

more accurately reflect the driving mechanisms present in the flow. While $\langle u^2 \rangle$ has very small contributions from SQ modes, it was found that the contributions to $\langle w^2 \rangle$ were more significant and may explain the slightly slower convergence in comparison to $\langle u^2 \rangle$ and $\langle v^2 \rangle$ seen in Figure 3.1. Interestingly, for the P4U solution, the contributions from OS and SQ modes are almost equal in magnitude and very strongly anti-correlated. This behavior is consistent with the observed results in Figure 3.2; an initially strong response from OS modes is eventually balanced by SQ modes as N_p increases (see Appendix for comparison of OS and SQ singular values). This competing effect between OS and SQ modes also seems to lend further support to the benefit of using separate bases for these two families of modes. We will now demonstrate how the utility of this approach extends to solutions in Couette flow as well.

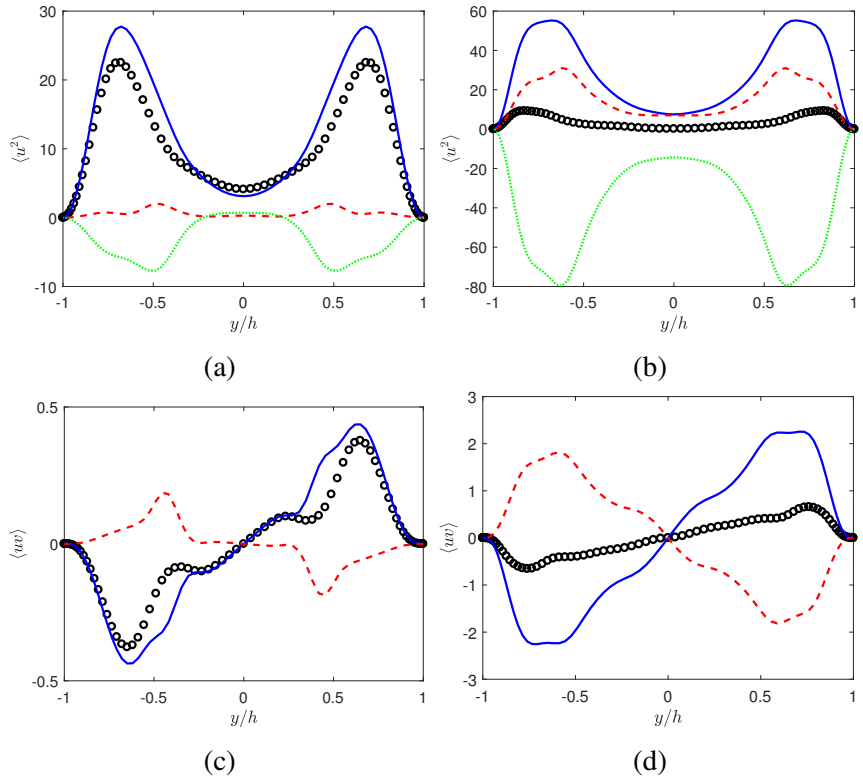

Figure 3.4: Top row: the contributions to the total $\langle u^2 \rangle$ Reynolds stress (open circles) from OS modes (solid line), SQ modes (dashed line), and their covariance (dotted line) for (a) P4L and (b) P4U. Bottom row: the contributions to the total $\langle uv \rangle$ Reynolds stress (open circles) from OS modes (solid line), SQ modes (dashed line) for (c) P4L and (d) P4U.

3.1.3 Equilibria and periodic orbits in Couette flow

In a similar manner to the previous section, we will project the EQ1 and EQ2 equilibrium solutions and the periodic orbits P19.02 and P87.89 onto the singular basis obtained from the 1D resolvent operator. For conciseness, we will restrict our attention to the modified OS/SQ approach and briefly highlight its ability to provide low-dimensional representations of these flows. Figure 3.5 shows the Reynolds stresses for EQ1 and EQ2 using an increasing number of singular modes. As with the P4 solutions, we observe a very rapid convergence to the true stress values. Needing roughly 10 singular modes per Fourier mode, this represents a reduction in the wall-normal degrees of freedom of approximately 70% (with respect to the $N_y = 35$ used in the simulation). Figure 3.6 shows the projections for P19.02 and P87.89. These periodic orbits have statistics that are very similar to EQ2; unsurprisingly, they are also well approximated by about 10 singular modes. We should note that only a small number of frequencies contributed significantly to

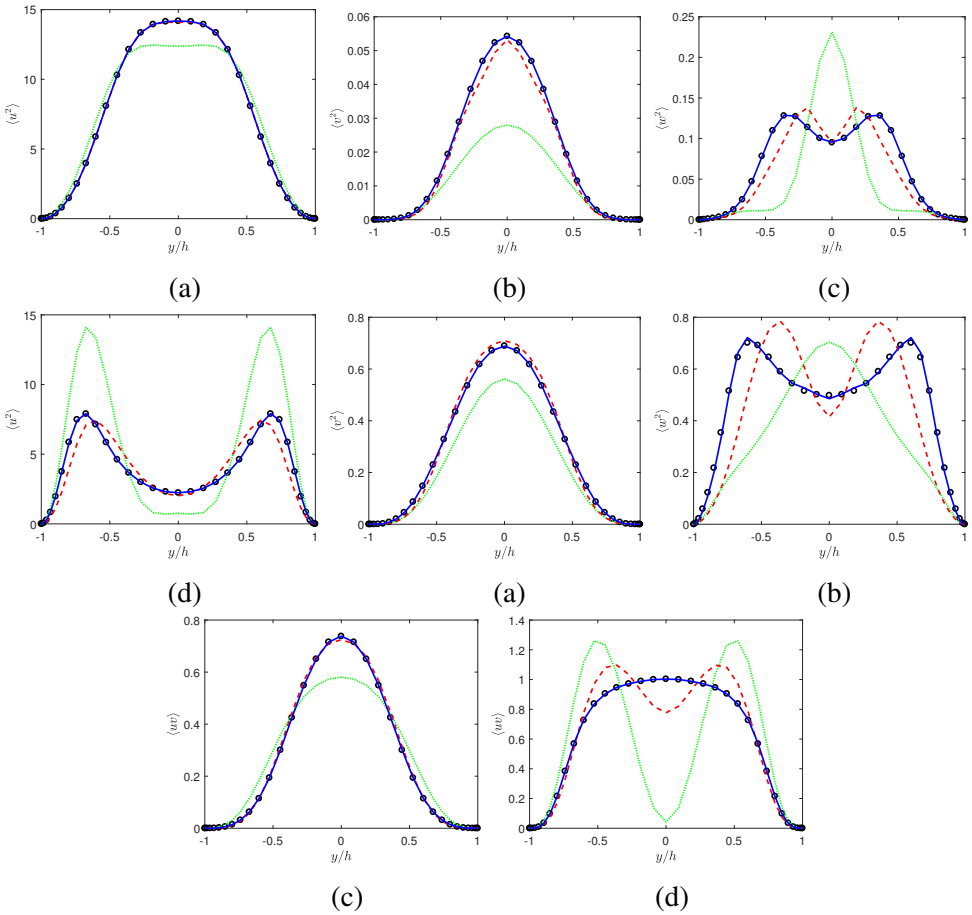

Figure 3.5: Reynolds stress profiles for EQ1 and EQ2 (open circles) and their approximations using $N = 1$ (dotted), $N = 3$ (dashed), and $N = 10$ (solid) singular modes for (a),(d) $\langle u^2 \rangle$, (b),(e) $\langle v^2 \rangle$, (c),(f) $\langle w^2 \rangle$, (g),(h) $\langle uv \rangle$. The top row and bottom left panel correspond to EQ1, and the middle row and bottom right panel correspond to EQ2; here, all projections are made using the modified OS/SQ approach. All quantities are in inner units.

the kinetic energy, namely the zero frequency component and the fundamental frequency corresponding to the period of the solution. While we do not report the results here, we also observed the same qualitative behavior for the Couette solutions in terms of the OS/SQ contributions to the Reynolds stresses.

Now that we've demonstrated the success of the modified OS/SQ approach for a variety of ECS solutions, we will now to turn our attention to the 2D resolvent analysis to showcase what further insights can be gained.

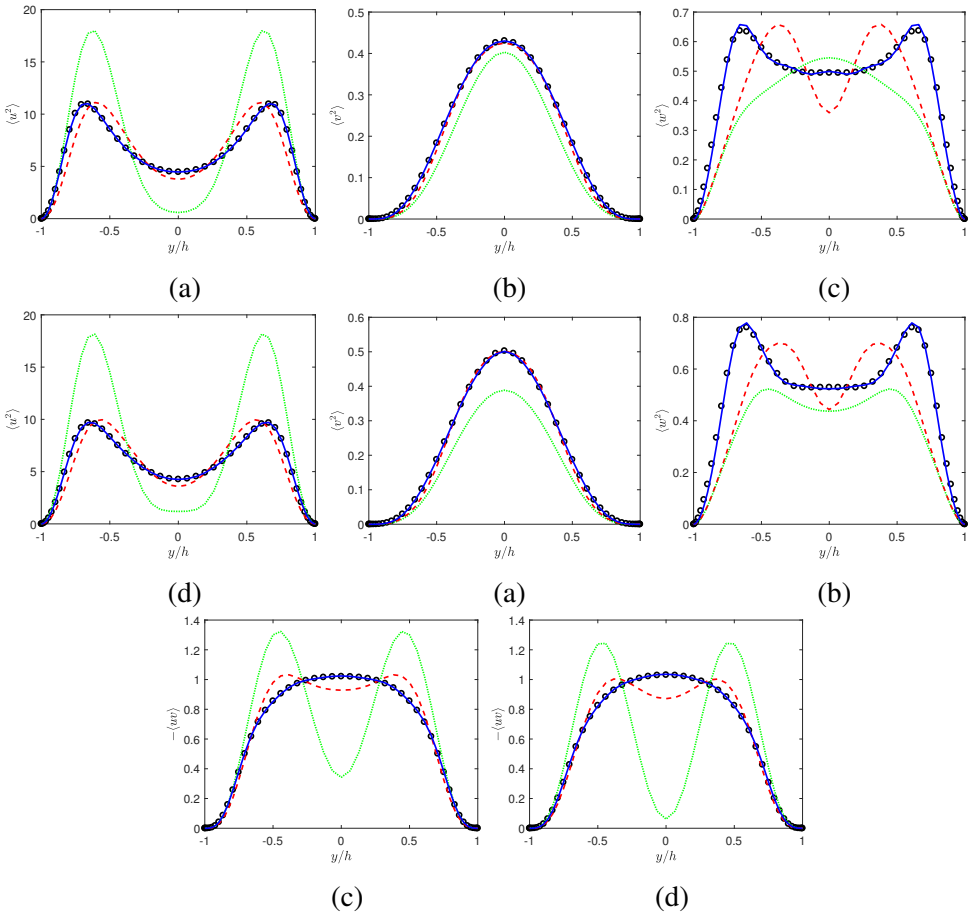

Figure 3.6: Reynolds stress profiles for the periodic orbits P19.02 and P87.89 (open circles) and their approximations using $N = 1$ (dotted), $N = 3$ (dashed), and $N = 10$ (solid) singular modes for (a),(d) $\langle u^2 \rangle$, (b),(e) $\langle v^2 \rangle$, (c),(f) $\langle w^2 \rangle$, (g),(h) $\langle uv \rangle$. The top row and bottom left panel correspond to P19.02, and the middle row and bottom right panel correspond to P87.89; here, all projections are made using the modified OS/SQ approach. All quantities are in inner units.

3.2 Low dimensional representation via 2D/3C resolvent analysis

In this section, we will focus on the equilibrium solutions in Couette flow, though we have verified the arguments presented herein apply more generally to solutions in Poiseuille flow as well (see Appendix). We will make use of the 2D/3C framework presented in §2.3, and in particular, the approximation of the velocity field in terms of singular modes defined in Equation 2.59. Instead of plotting integrated results in the form of statistics, we will focus on how well we can capture individual Fourier modes. As we will show shortly, the key to modeling most of these flows boils down to capturing the Fourier mode corresponding to the fundamental streamwise wavenumber (i.e. the wavenumber associated with the length of the simulation box).

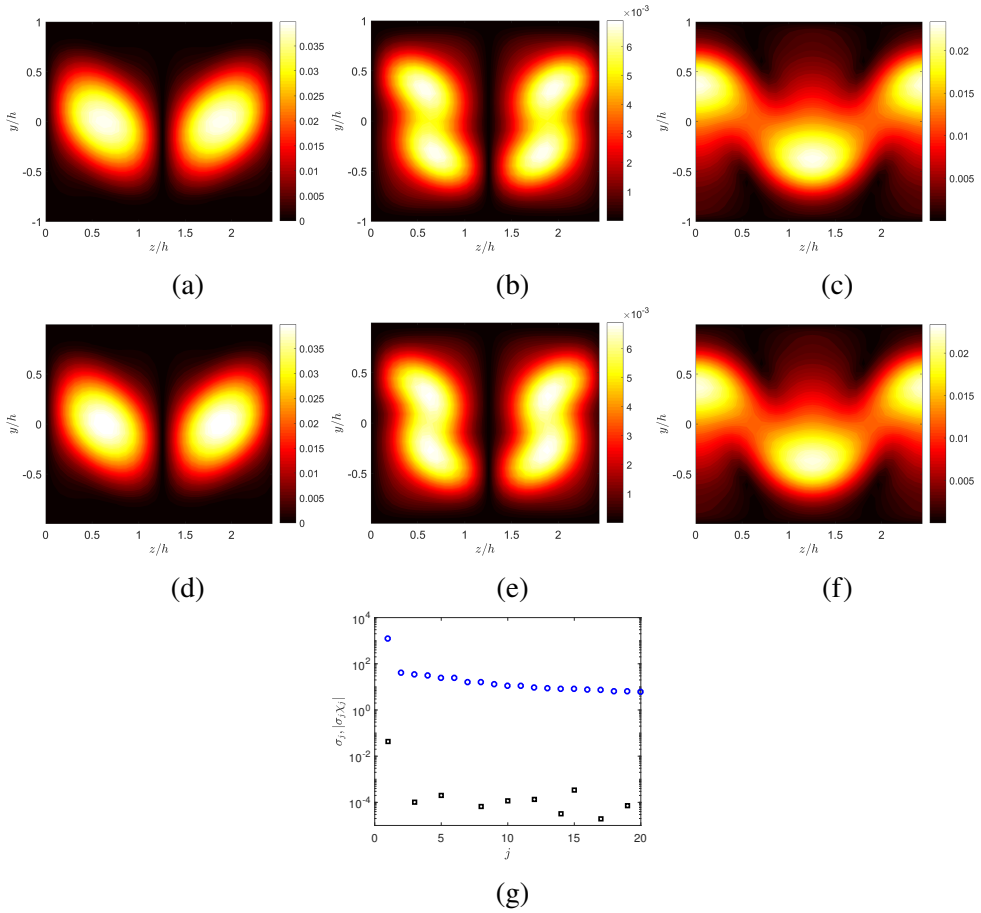

Figure 3.7: The amplitude of the fundamental streamwise Fourier mode $\hat{\mathbf{u}}(k_x = 1.14, \omega = 0; y, z)$ for EQ1, with the top row corresponding to the true value and the middle row corresponding to the projection onto the leading response mode for (a),(d) $\hat{u}(y, z)$,(b),(e) $\hat{v}(y, z)$, (c),(f) $\hat{w}(y, z)$, along with (g) the first 20 singular values σ_j (open circles) and the product $|\sigma_j \chi_j|$ (squares).

3.2.1 2D/3C analysis of equilibria

In Figure 3.7, we show the amplitude of the $\hat{u}$, $\hat{v}$, and $\hat{w}$ components of the fundamental Fourier streamwise wavenumber for EQ1 as well as the projection onto the leading singular mode,

$$\hat{\mathbf{u}}(k_x = 1.14, \omega = 0) \approx \sigma_1 \chi_1 \tilde{\psi}_1. \tag{3.3}$$

To a very good approximation, this Fourier mode is captured with a single response mode. Also shown in Figure 3.7 is a plot of the first 20 singular values and the magnitude of the product $|\sigma\chi|$. Notably, σ_1 is almost 2 orders of magnitude larger than σ_2. This is suggestive of why this Fourier mode is so well approximated with

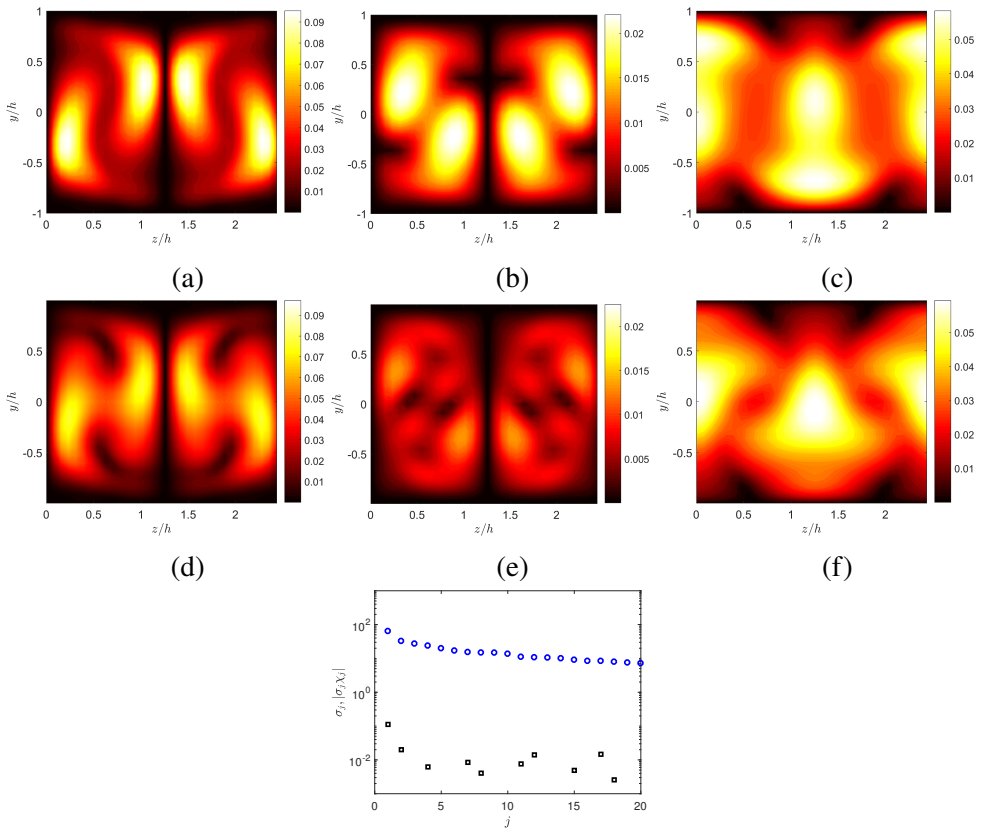

Figure 3.8: The amplitude of the fundamental streamwise Fourier mode $\hat{\mathbf{u}}(k_x = 1.14, \omega = 0; y, z)$ for EQ2, with the top row corresponding to the true value and the middle row corresponding to the projection onto the leading response mode for (a),(d) $\hat{u}(y, z)$,(b),(e) $\hat{v}(y, z)$, (c),(f) $\hat{w}(y, z)$, along with (g) the first 20 singular values σ_j (open circles) and the product $|\sigma_j \chi_j|$ (squares).

the leading response mode, further supported by the fact that $|\sigma_1 \chi_1| \gg |\sigma_2 \chi_2|$. The lower branch traveling wave solution P4L also exhibited a similar behavior (see Appendix).

In Figure 3.8, we again show the amplitude of the $\hat{u}$, $\hat{v}$, and $\hat{w}$ components of the fundamental Fourier streamwise wavenumber but now for the upper branch solution EQ2. We also show the projection onto the leading response mode, as well a plot of the first 20 singular values and the magnitude of the product $|\sigma \chi|$. In contrast to EQ1, the leading response mode does not give an accurate approximation of the Fourier mode. This may be in part attributed to the fact that there is not a dominant singular value; in Figure 3.8 we see σ_1 is only about a factor of 2 larger than σ_2. In a related manner, other upper branch solutions (including P4U) demonstrated this type of behavior. Moreover, the periodic solutions P19.02 and P87.89, which shared

statistical similarities of EQ2, were also not amenable to approximation using the just the leading response mode. We will seek to further explain these results in terms of the relevant scale interactions.

3.2.2 Identifying scale interactions

We alluded earlier to the fact that the fundamental streamwise Fourier mode plays a prominent role in the ECS solutions. We will now quantify this claim as it relates to the 2D/3C mean velocity and how these solutions self-sustain. Recall from Equation 2.63, we can express the forcing for a particular Fourier mode as a convolution over all triadically-consistent scales. When we consider the mean forcing, which acts to sustain the mean velocity, we are concerned with interactions of the form

$$\hat{\mathbf{f}}(\mathbf{k}=\mathbf{0}) = \sum_{\mathbf{k}_a=-\mathbf{k}_b} -\nabla\cdot\left(\hat{\mathbf{u}}(\mathbf{k}_a)\hat{\mathbf{u}}^T(\mathbf{k}_b)\right), \tag{3.4}$$

which can be approximated in terms of just the fundamental streamwise Fourier mode $\hat{\mathbf{u}}(k_x = 1.14, \omega = 0) \equiv \hat{\mathbf{u}}_f$ (where the subscript $_f$ denotes fundamental) as

$$\hat{\mathbf{f}}(\mathbf{k}=\mathbf{0}) \approx -\nabla\cdot\left(\hat{\mathbf{u}}_f\hat{\mathbf{u}}_f^{*T}\right). \tag{3.5}$$

To evaluate the validity of this approximation, we plot the mean forcing components using the expressions in Equations 3.4 and 3.5 for EQ1 and EQ2, as shown in Figure 3.9. We see that considering just the interaction of the fundamental streamwise Fourier mode is an exceedingly good approximation for EQ1. We emphasize this notion is not original to this analysis as other authors have appreciated this fact in the context of vortex-wave interaction (Waleffe, 1997; Hall and Sherwin, 2010), and we will expand further upon these ideas shortly; however, that the fundamental mode can be so well approximated from the leading response mode of the resolvent operator for lower branch solutions we believe to be a novel contribution. Although not quite as good as the results obtained for EQ1, we see most of the mean forcing for EQ2 is driven by the fundamental streamwise Fourier mode; however, clearly higher harmonics need to be considered. Though we only plot results for EQ1 and EQ2, we again remark that this appears to be a representative result for lower and upper branch solutions (see Appendix).

Given the prominent role that the fundamental streamwise Fourier mode plays in sustaining the mean, we may then ask which scale interactions are important in sustaining the fundamental mode. For the following discussion, we will restrict our attention to EQ1. Clearly, from Figure 3.7, the SVD of the resolvent operator is

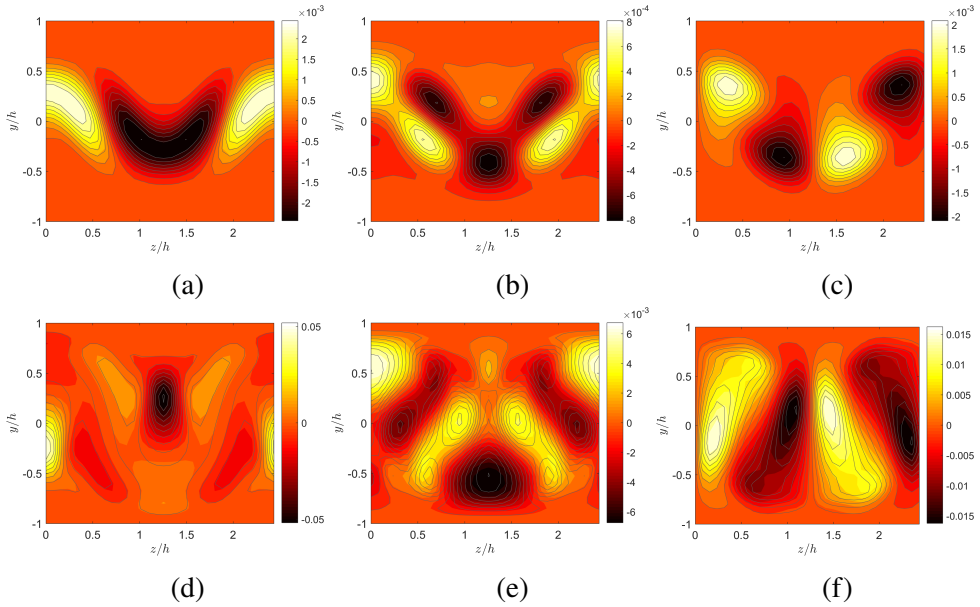

Figure 3.9: The mean forcing components for EQ1 (top row) and EQ2 (bottom row). The color denotes the true value (i.e. the convolution over all wavenumbers) and the contour lines represent the interaction of only the fundamental streamwise wavenumber with its complex conjugate for the (a,d) u-component, (b,e) v-component, (c,f) w-component.

able to pick out a highly amplified response mode with the correct spatial support. Therefore, the only role of the nonlinearity in this context is to set the correct amplitude of this response mode (via the weight χ_1 in Equation 3.3, which is the only effective unknown). We can, as was done for the mean, postulate that the nonlinear forcing for the fundamental streamwise mode is dominated by a single triadic interaction. Adopting the compact notation $\hat{\mathbf{u}}(k_x = 1.14, \omega = 0) \equiv \hat{\mathbf{u}}_f$ and $\hat{\mathbf{u}}(k_x = 2.28, \omega = 0) \equiv \hat{\mathbf{u}}_h$ (where the subscript $_h$ denotes harmonic), we can approximate the forcing as

$$\hat{\mathbf{f}}(k_x = 1.14, \omega = 0) \equiv \hat{\mathbf{f}}_f \approx -\nabla \cdot \left(\hat{\mathbf{u}}_f^* \hat{\mathbf{u}}_h^T \right). \tag{3.6}$$

Given that we can accurately predict the spatial structure of $\hat{\mathbf{u}}_f$ from the resolvent as $\hat{\mathbf{u}}_f \approx \sigma_1 \chi_1 \tilde{\psi}_1$ (and consequently $\hat{\mathbf{u}}_f^*$ from Hermitian symmetry), if we could somehow model the first harmonic $\hat{\mathbf{u}}_h$, we might be able to close the system (i.e. compute χ_1). One obvious choice would be to approximate the harmonic with the leading response mode of the resolvent, which is shown in figure 3.10 along with the true amplitude of the Fourier mode. We see the leading projection very poorly represents the velocity field. We again argue that the lack of a dominant singular value (also plotted in Figure 3.10) may have suggested this to be the case. However,

another option to approximate the harmonic would be to again consider the dominant scale interactions at play. Leveraging our knowledge of the role of the fundamental streamwise mode, we could the approximate the forcing for the harmonic as

$$\hat{\mathbf{f}}(k_x = 2.28, \omega = 0) \equiv \hat{\mathbf{f}}_h \approx -\nabla \cdot \left(\hat{\mathbf{u}}_f \hat{\mathbf{u}}_f^T \right). \tag{3.7}$$

With this representation of the forcing, we can directly pass it through the resolvent operator $\mathcal{H}^{2D}(k_x = 2.28, \omega = 0)$ to compute $\hat{\mathbf{u}}_h$ as

$$\hat{\mathbf{u}}_h \approx C\mathcal{H}^{2D} \left\{ M^{-1} B \hat{\mathbf{f}}_h \right\}, \tag{3.8}$$

where, if we use the approximation for $\hat{\mathbf{u}}_f$ in Equation 3.3 to compute the forcing $\hat{\mathbf{f}}_h$, yields

$$\hat{\mathbf{u}}_h \approx -\sigma_1^2 \chi_1^2 C\mathcal{H}^{2D} \left\{ M^{-1} B \left[\nabla \cdot \left(\tilde{\psi}_1 \tilde{\psi}_1^T \right) \right] \right\}. \tag{3.9}$$

To validate these assumptions about the relevant scale interactions, we plot the amplitude of the $\hat{u}$, $\hat{v}$, and $\hat{w}$ components for the harmonic $\hat{\mathbf{u}}(k_x = 2.28, \omega = 0)$ in Figure 3.11 using the expression in Equation 3.9. Referencing the true amplitude shown in Figure 3.10 (top row), we see the approximation based on Equation 3.9 accurately captures the amplitude of this Fourier mode. Thus, while the SVD of the resolvent may fail to provide an accurate low-dimensional basis for a particular Fourier mode, it may still be possible to leverage the knowledge of the dominant scale interactions to accurately model the mode. Interestingly, this type of result has also been demonstrated in low-Reynolds number cylinder flow (Symon, 2018). Returning to the notion of computing χ_1, we recall it is formally defined as

$$\chi_1 = \langle M^{-1} B \hat{\mathbf{f}}_f, \hat{\phi}_1 \rangle_w. \tag{3.10}$$

If we approximate $\hat{\mathbf{f}}_f$ as is done in Equation 3.6 and additionally approximate $\hat{\mathbf{u}}_f^*$ (which is proportional to χ_1^*) and $\hat{\mathbf{u}}_h$ (which is proportional to χ_1^2) using Equations 3.3 and 3.9 respectively, we can express the forcing in the form

$$\hat{\mathbf{f}}_f = |\chi_1|^2 \chi_1 \hat{\mathbf{f}}'_f, \tag{3.11}$$

where $\hat{\mathbf{f}}'_f = \hat{\mathbf{f}}'_f(\tilde{\psi}_1, \sigma_1, M, B, C, \mathcal{H}^{2D})$. Consequently, we can compute the amplitude of χ_1 as

$$|\chi_1| = \left[\frac{1}{\langle M^{-1} B \hat{\mathbf{f}}'_f, \hat{\phi}_1 \rangle_w} \right]^{1/2}. \tag{3.12}$$

Notably, this quantity can be computed with knowledge of only the mean velocity. If we compare the value generated by Equation 3.12 to the true value computed by explicitly calculating the full nonlinear forcing, the discrepancy for EQ1 is $\approx 10\%$ which is quite good given the limited information utilized.

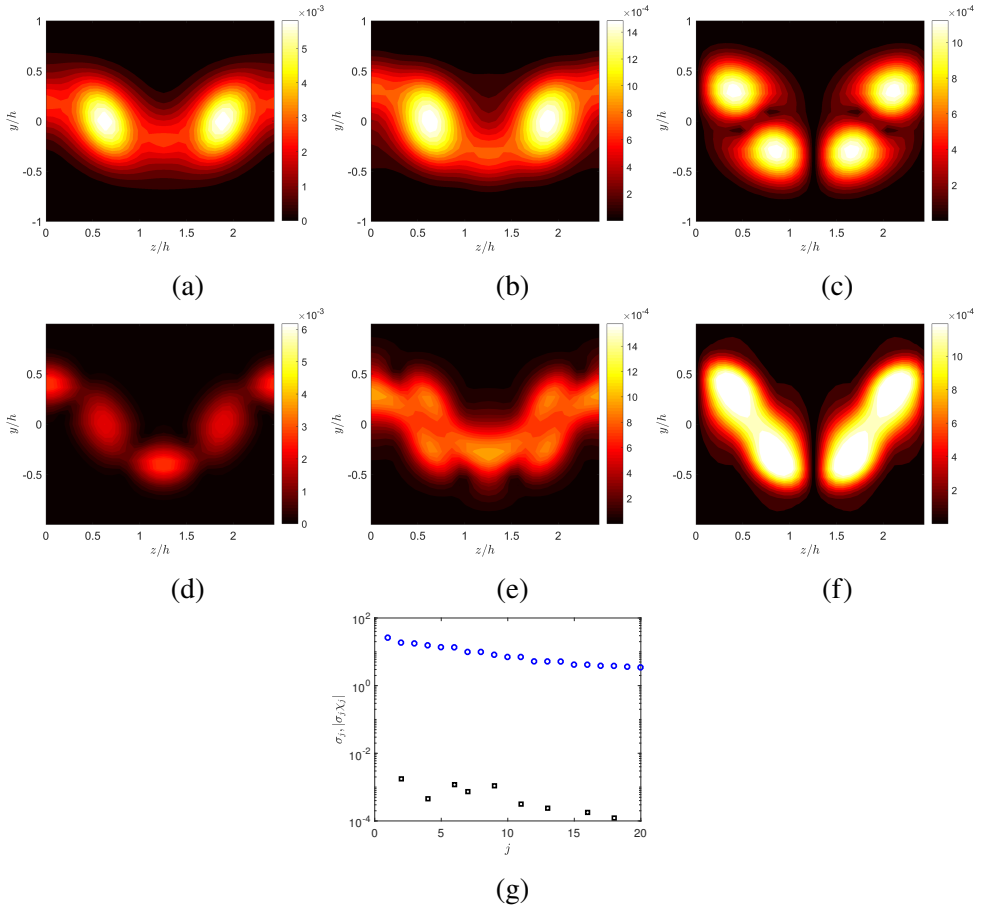

Figure 3.10: The amplitude of the Fourier mode $\hat{\mathbf{u}}(k_x = 2.28, \omega = 0; y, z)$ for EQ1 with the top row corresponding to the true value and the middle row corresponding to the projection onto the leading response mode for (a),(d) $\hat{u}(y, z)$,(b),(e) $\hat{v}(y, z)$, (c),(f) $\hat{w}(y, z)$, along with (g) the first 20 singular values σ_j (open circles) and the product $|\sigma_j \chi_j|$ (squares).

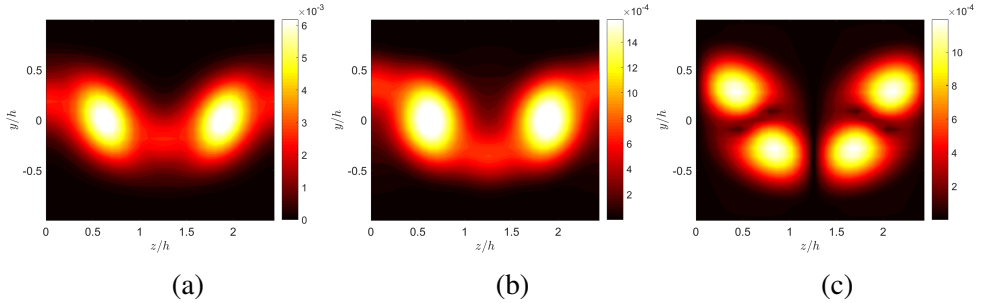

Figure 3.11: The amplitude of the Fourier mode $\hat{\mathbf{u}}(k_x = 2.28, \omega = 0; y, z)$ for EQ1 computed by passing the forcing generated by the interaction of the leading response mode for $(k_x = 1.14, \omega = 0)$ through the resolvent operator (see Equation 3.9): (a) $\hat{u}(y, z)$,(b) $\hat{v}(y, z)$ and (c) $\hat{w}(y, z)$.

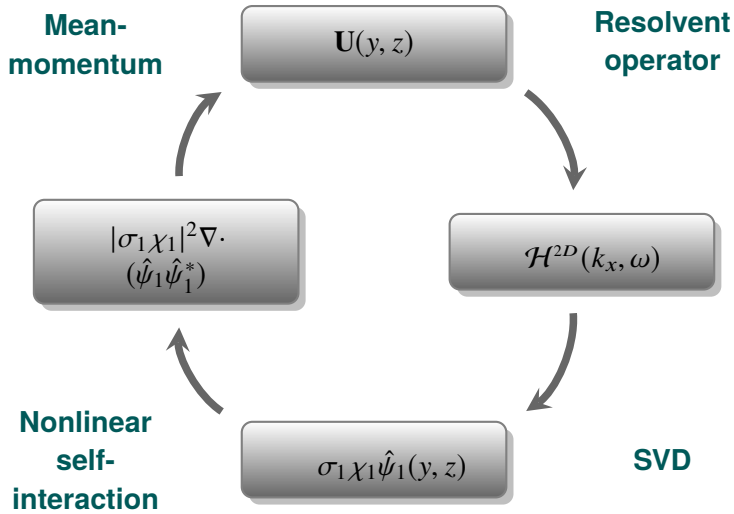

Figure 3.12: An adaptation of the self-sustaining process (Waleffe, 1997) through the lens of resolvent analysis.

3.2.3 Connections to the self-sustaining process

To briefly summarize, we demonstrated for EQ1 that the 2D/3C mean velocity is sustained via the self-interaction of the fundamental streamwise Fourier mode. In turn, the spatial structure of the fundamental mode can be predicted from the leading response mode of the resolvent operator (where the mean velocity is an input). The only effective unknown is the amplitude of the leading response mode, which is set by the nonlinear forcing. We showed that the relevant interactions giving rise to the forcing were dominated by the fundamental mode and the first harmonic, where the harmonic is in turn (to a good approximation) generated via the self-interaction of the fundamental mode. Thus, unequivocally the description of this solution is rooted deeply in the behavior of the fundamental mode. We illustrate this idea in Figure 3.12, where we have adapted the vision of the self-sustaining process proposed by Waleffe, 1997 through the lens of resolvent analysis. Though we do not report further results here, we again remark that the aforementioned description appears to hold for lower branch solutions in general (see Appendix). We will show in §3.3 how we can use these ideas and the 2D/3C resolvent framework to compute lower branch solutions in Couette flow. Unfortunately, it appears these types of ideas of cannot be applied to upper branch solutions because they are not amenable to approximation with a single response mode and the underlying scale interactions are more complicated. However, we will also show in §3.3 how we can start from a lower branch solution and utilize the tools from §2.2 and §2.4 to compute very good approximations of the corresponding upper branch solution.

3.3 Implications for computation of ECS

We will describe two new approaches to computing ECS utilizing the tools developed in the previous sections. The first method will use the 2D/3C resolvent framework and the process described in Figure 3.12. The second method, in light of the improvement attained from the modified OS/SQ decomposition, will attempt to solve directly for the unknown weights in terms of the interaction coefficients described in §2.4. We will utilize Channelflow to verify the validity of the solutions we generate. We will present results for equilibria in Couette flow and comment on possible extensions of these methods to other flows of interest.

3.3.1 Computing solutions starting from laminar

Recall that the underlying assumption in resolvent analysis is *a priori* knowledge of the mean velocity. Arguably, this is sometimes a strong assumption, particularly in the 2D/3C case. As a result, we were interested to see if we could unshackle ourselves from this assumption and start from the laminar profile to arrive at a meaningful result.

Our approach is to use the 2D/3C resolvent framework in conjunction with the self-sustaining loop illustrated in Figure 3.12 to find an equilibrium solution; this is a particularly attractive approach as it has only one unknown amplitude parameter. For the sake of comparison, we will consider the same box size and Reynolds number as the previously analyzed equilibria (see Table 3.1). We begin at the top of the loop by specifying an initial laminar profile: $U(y,z) = y$, $V(y,z), W(y,z) = \mathbf{0}$. We feed this into the 2D resolvent operator to compute the leading response mode $\tilde{\psi}_1$. Next we specify the amplitude of the response mode: here we found it more suitable to specify the total amplitude $A = |\chi_1\sigma_1|$ instead of $|\chi_1|$. Once this is specified, we compute the self-interaction of this mode to generate the mean forcing and then solve the mean momentum Equations 2.44-2.45 to compute a new mean $\mathbf{U}(y,z)$. We then repeat this process (holding A constant) and see if we converge to an (approximate) solution given by

$$\mathbf{u}(x,y,z) = \mathbf{U}(y,z) + \left(|A|\tilde{\psi}\boldsymbol{e}^{ik_x x} + c.c.\right), \tag{3.13}$$

where c.c. denotes the complex conjugate. Figure 3.13 shows the mean velocity $\mathbf{U}(y,z)$ for 3 iterations ((a)-(c)) of this procedure using an amplitude of $A = 0.06$; we will discuss shortly criterion for selecting A. The L2 norm percentage difference between the mean fields in (b) and (c) is roughly 3%. The corresponding amplitudes of the u, v, and w components of the fundamental streamwise mode are shown in

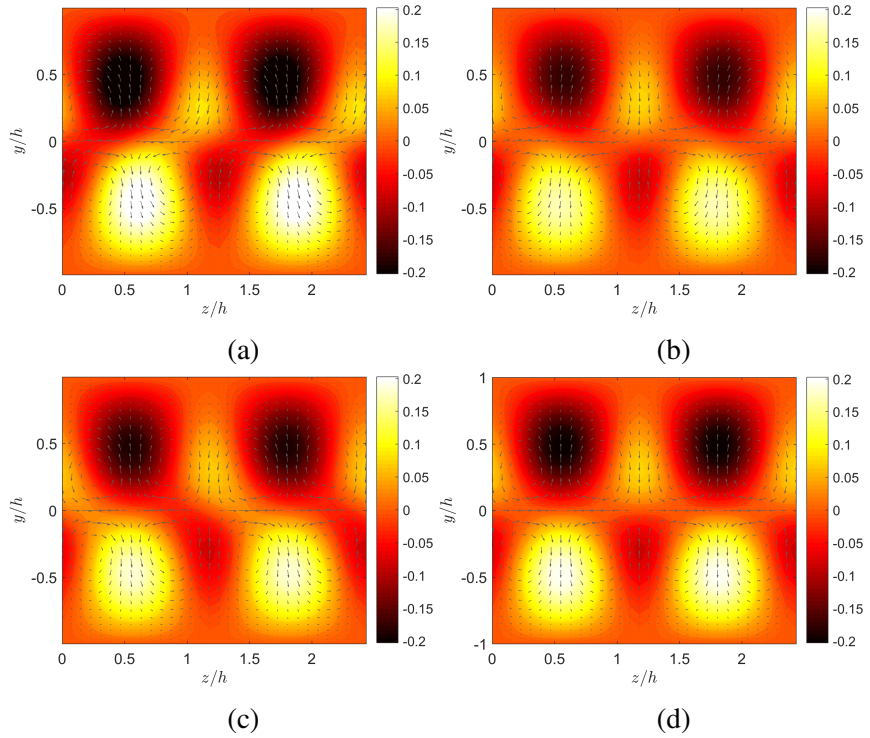

Figure 3.13: The mean velocity computed using an iterative procedure based on the 2D resolvent operator and an initial laminar profile. Here the color contours are the streamwise velocity (deviation from laminar) and the vector arrows represent the spanwise/wall-normal velocity for (a) iteration 1, (b) iteration 2, (c) iteration 3, and (d) the converged mean computed using Channelflow. This solution corresponds to the previously computed EQ7 (Gibson et al., 2009).

Figure 3.14 in the first 3 rows. If we then take the velocity field from iteration 3, place it in the form given in Equation 3.13, and feed this as an initial guess to Channelflow, we arrive at the solution shown in Figures 3.13(d) and 3.14(j)-(l). It is worth noting this particular solution has already been computed, and corresponds to EQ7 (Gibson et al., 2009). Clearly, the iterative procedure provides an extremely good approximation to the true solution. We again emphasize we arrived at this approximate solution needing only to specify a single parameter, $|A|$. Additionally, we have several criteria to guide the search for $|A|$. A value of $|A|$ that is too small will not yield a field that significantly differs from laminar; similarly, a value too large will not lead to convergence within the loop illustrated in Figure 3.12. Furthermore, from our analysis in §3.2, we know the mean velocity (which is computed based on $|A|$) and the associated resolvent operator should yield a dominant leading singular value for this type of solution. Finally, for a given $|A|$, we can compare the associated value of $|\chi_1| = \frac{|A|}{\sigma_1}$ with the value given in Equation 3.12 as another self-consistency

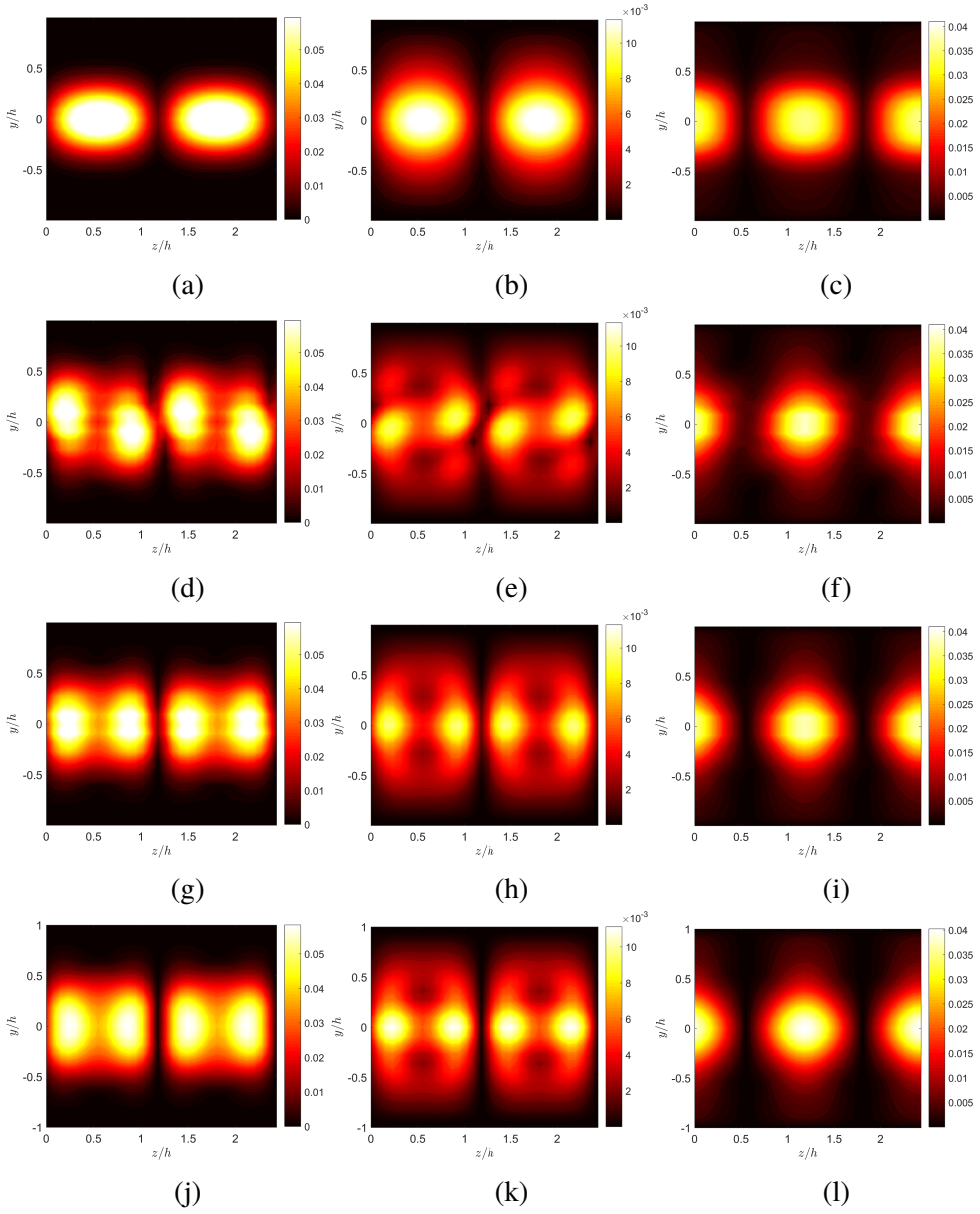

Figure 3.14: The amplitude of the u-component (left column), v-component (middle column), and w-component (right column) of the fundamental streamwise Fourier mode computed using an iterative procedure based on the 2D resolvent operator and an initial laminar profile. The first row (a-c) corresponds to the first iteration, (d-f) to the second iteration, (g-i) the third iteration, and (j-l) represents the converged field computed using Channelflow with iteration 3 (and the associated mean $\mathbf{U}(y, z)$) as an input.

check. It would also be noteworthy to perform a weakly nonlinear analysis (Herbert, 1977) as another means of determining the amplitude behavior of these types of solutions. This framework can easily be applied to a variety of flows, such as Poiseuille flow or pipe-flow, with the small caveat that a non-zero wavespeed needs be considered. As there are methods to find new solutions based on an existing solution (Ahmed and Sharma, 2017), this approach may serve as a useful initial tool to find solutions for flows where the laminar solution is known.

3.3.2 Solving in coefficient space

Now we return to the 1D resolvent framework to discuss a second solution method based on the concept of interaction coefficients introduced in §2.4. We will restrict our attention to the modified OS/SQ approach given its success in representing ECS solutions. If we assume we know the mean velocity of a particular solution, the only unknowns in our formulation are the (complex) weights χ_{os} and χ_{sq} (across all wavenumber/frequency space and singular modes). From Hermitian symmetry, we need only consider the positive streamwise wavenumbers (including $k_x = 0$). Suppose now that we stack all of these unknowns into a single column vector γ,

$$\gamma = \begin{bmatrix} \chi_{\mathrm{os}} \\ \chi_{\mathrm{sq}} \end{bmatrix}. \tag{3.14}$$

Recall from Equations 2.73 and 2.74 that the each weight is expressed as a sum of quadratic terms that involves the interaction coefficients and other weights that are triadically linked. We can recast these equations symbolically as a zero equation by defining the residual r,

$$r(\gamma) = \gamma - S(\gamma), \tag{3.15}$$

where S represents the sums on the right-hand side of Equations 2.73-2.74. Thus, Equation 3.15 represents a large system of coupled quadratic equations. However, the weights that drive this residual to zero must also generate the assumed mean (which was used to compute the interaction coefficients) in order to be self-consistent. We can incorporate this mean constraint by appending the residual vector as

$$r(\gamma) = \begin{bmatrix} \gamma - S(\gamma) \\ \langle f_u \rangle - f_{u_0}(\gamma) \\ f_{w_0}(\gamma) \end{bmatrix}. \tag{3.16}$$

Here, $\langle f_u \rangle$ is known and related to the mean streamwise velocity via Equation 2.4, and $f_{u_0}(\gamma)$ is the corresponding mean u-forcing generated from the weights γ. We

also enforce that the mean w-forcing $f_{w_0}(\gamma)$ is zero so that there is no mean spanwise velocity. The mean v-forcing is connected to the mean pressure (which we assume we don't know *a priori*) and therefore do not place any constraints on it.

With the residual vector $r(\gamma)$, one method to solve for γ is to pose the following optimization problem in which we minimize the sum of the squares of the residuals:

$$\min_{\gamma} \; f(\gamma) = \frac{1}{2} r(\gamma)^T r(\gamma) = \frac{1}{2} ||r(\gamma)||_2^2. \tag{3.17}$$

Here we include quadrature points with the mean constraint so that the residual has a well-defined norm. Suppose now we approximate $f(\gamma)$ in some neighborhood of γ^* using a second-order Taylor-expansion as

$$f(\gamma^* + \Delta\gamma) \approx f(\gamma^*) + \nabla f(\gamma^*)^T \Delta\gamma + \frac{1}{2} \Delta\gamma^T \nabla^2 f(\gamma^*) \Delta\gamma. \tag{3.18}$$

Here, the gradient $\nabla f(\gamma)$ is

$$\nabla f(\gamma) = J(\gamma)^T r(\gamma) \tag{3.19}$$

where the Jacobian J is

$$J_{ij} = \frac{\partial r_i}{\partial \gamma_j} \tag{3.20}$$

and $\nabla^2 f(\gamma)$, henceforth referred to as the Hessian $H(\gamma)$, can be approximated (ignoring 2nd order derivatives of $r(\gamma)$) as

$$\nabla^2 f(\gamma) \equiv H(\gamma) \approx J(\gamma)^T J(\gamma). \tag{3.21}$$

Consequently, we can rewrite the optimization problem in Equation 3.17 as

$$\min_{\Delta\gamma} \; \left\{ f(\gamma^*) + \nabla f(\gamma^*)^T \Delta\gamma + \frac{1}{2} \Delta\gamma^T H(\gamma^*) \Delta\gamma \right\}, \tag{3.22}$$

which yields the updated guess (after setting the partial derivative of the objective function with respect to $\Delta\gamma$ to 0)

$$\begin{aligned} \gamma &= \gamma^* + \Delta\gamma \\ \Delta\gamma &= -H(\gamma^*)^{-1} \nabla f(\gamma^*). \end{aligned} \tag{3.23}$$

This approach is known as the Gauss-Newton method (Bjorck, 1996). A slightly modified approach, known as a trust-region method, instead considers the constrained optimization problem

$$\begin{aligned} \min_{\Delta\gamma} \quad & \left\{ f(\gamma^*) + \nabla f(\gamma^*)^T \Delta\gamma + \frac{1}{2} \Delta\gamma^T H(\gamma^*) \Delta\gamma \right\} \\ \text{subject to} \quad & ||\Delta\gamma|| \leq \delta_t \end{aligned} \tag{3.24}$$

where δ_t quantifies the region of trust (i.e. how well the local quadratic model approximates f(γ)). An iterative sub-problem is solved to adjust δ_t to determine the optimal step $\Delta\gamma$. There exist well-established algorithms (Moré and Sorensen, 1983) to solve this optimization problem. The trust-region method is known to be more robust in comparison to Gauss-Newton, especially for initial guesses that are far from the solution, and thus we focus on this approach. We utilize the built-in MATLAB function *fminunc* to solve the formal optimization problem defined in Equation 3.17 and use its trust-region algorithm to solve the corresponding optimization problem defined in Equation 3.24. The function needs as an input an initial guess of the weights γ^*; here, we select from a random uniform distribution. Additionally, we pass along to the algorithm within *fminunc* the residual $f(\gamma^*)$, the gradient $\nabla f(\gamma^*)$, and the Hessian $H(\gamma^*)$. The latter two need not be explicitly passed through as they can be evaluated numerically via finite differences within the function. However, we are in the fortunate position that we can compute these quantities based on analytical expressions (Equations 2.73-2.74). This provides a significant savings in computational cost. Lastly, we specify the stopping criterion $|f^{i+1}(\gamma) - f^i(\gamma)| < 1\text{e}{-12}$ where i denotes the iteration number.

Application to EQ1

We now demonstrate this optimization-based coefficient solver for EQ1. The only data we assume known *a priori* is the 1D mean velocity $U(y)$. With this, we can pre-compute the interaction coefficients in Equation 2.75. For proof of principle, we will utilize our prior analysis to restrict ourselves to a subset of wavenumbers to reduce the overall number of unknowns: here we use $N_{k_x} = 4$ (positive, including 0) streamwise Fourier modes, $N_{k_z} = 12$ spanwise Fourier modes, and use $N = 10$ singular modes per wavenumber pair. This results in a total number of unknowns on the order of ≈ 2000. We visualize the results of the optimization algorithm by plotting the streamwise-averaged mean velocity $\mathbf{U}(y, z)$ for multiple iterations, as shown in Figure 3.15. We see the mean field morphs from the random initial guess to a well-converged field in 16 iterations. In Figure 3.16, we show the sum of the squares of the residual vector as a function of iteration count, approaching a value of $O(1\text{e}{-12})$ before reaching the stopping criterion. To validate this guess of the solution, we input the velocity field at the last iteration into Channelflow. Figure 3.16 also shows the mean velocity $\mathbf{U}(y, z)$ computed from Channelflow; it is nearly indistinguishable from the mean field of the final iteration in 3.15 with the L2-norm difference between the fields being $O(1\text{e}{-5})$. Finally, in Figure 3.17

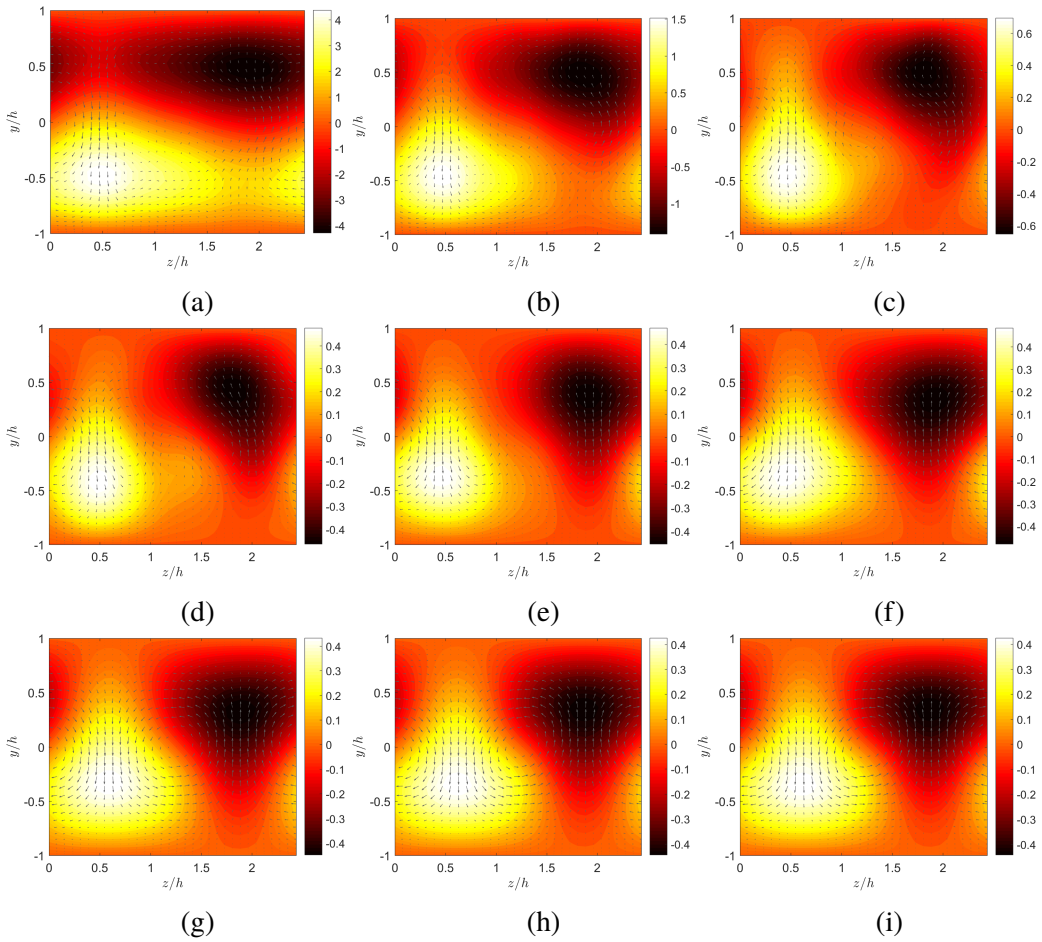

Figure 3.15: The mean velocity field of EQ1 computed using the coefficient solver described in section. Here the color contours are the streamwise velocity (deviation from laminar) and the vector arrows represent the spanwise/wall-normal velocity: (a) the initial field based on a random guess of the weights, (b)-(i) iterations 1, 2, 3, 4, 5, 10, 13, and 16 respectively.

we compare the variance profiles for the optimization solution and the true values from the Channelflow solution and again observe, for all intents and purposes, near-perfect matching between the two. We emphasize that while we enforced matching of $\langle uv \rangle$ via the mean constraint, the other profiles are purely predictions based on the optimization solution. From the results presented, we can confidently claim we have found an extremely good approximate solution to the NSE whose computation required only knowledge of the 1D mean velocity.

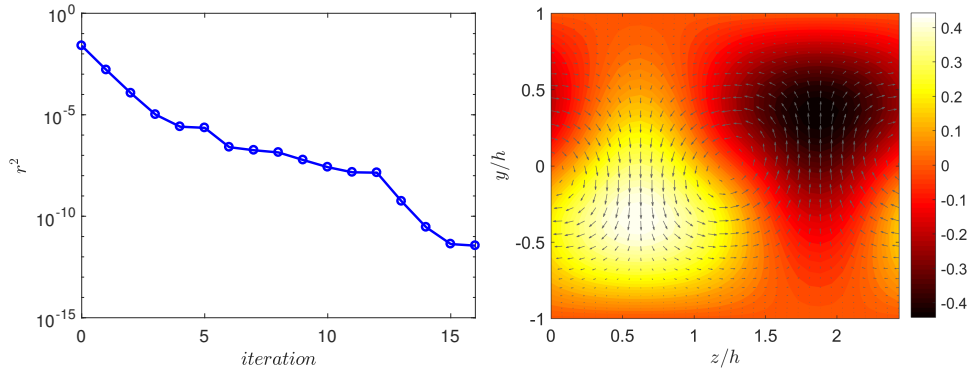

(a) (b)

Figure 3.16: The (a) sum of the squares of the residual vector as a function of iteration count and (b) the converged mean velocity profile for EQ1 computed using the field from the final iteration of the coefficient solver as an input into Channelflow.

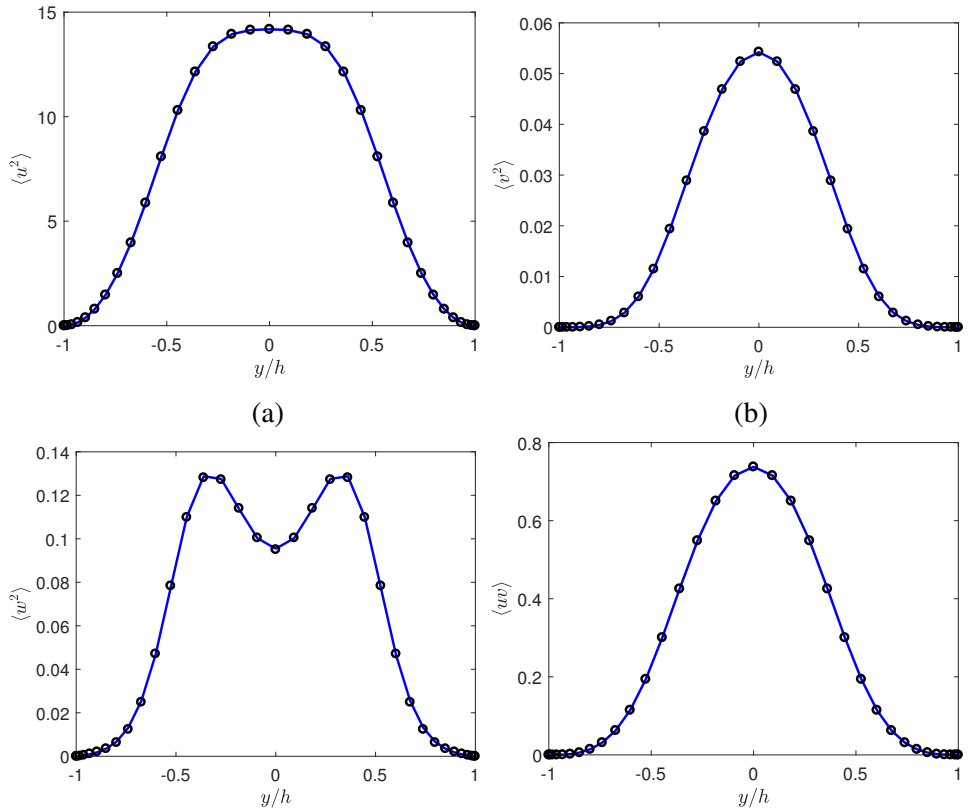

(a) (b)

(c) (d)

Figure 3.17: Reynolds stress profiles for EQ1 (open circles) and the values based on the solution generated from the coefficient-solver (line) for (a) $\langle u^2 \rangle$, (b) $\langle v^2 \rangle$, (c) $\langle w^2 \rangle$, (d) $\langle uv \rangle$. All quantities are in inner units.

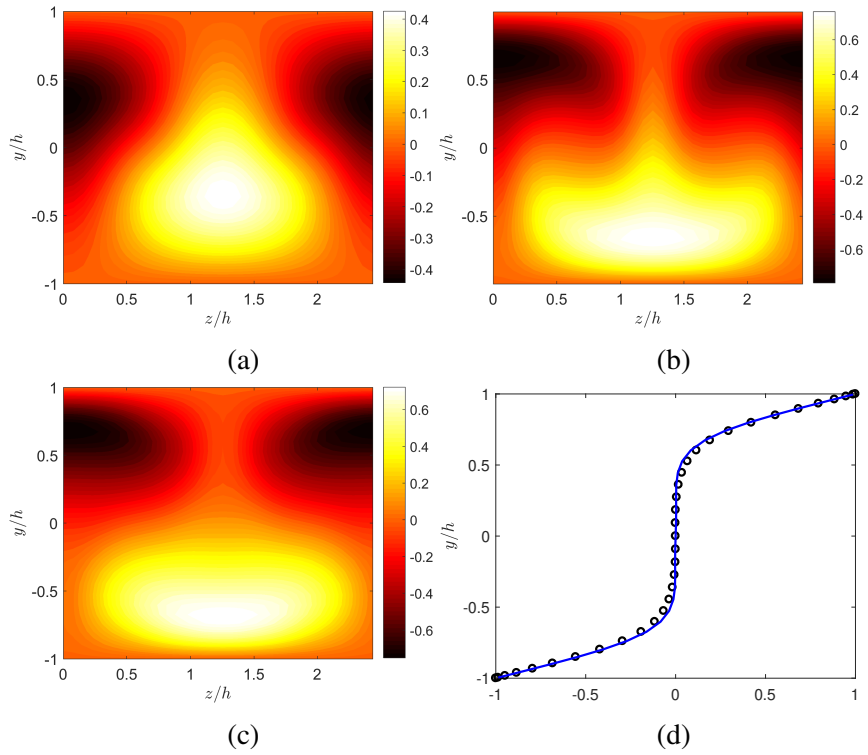

Figure 3.18: The mean streamwise velocity (deviation from laminar) for (a) EQ1, (b) a guess for the upper-branch (EQ2) mean based on overly-amplified EQ1 mean-forcing, (c) the true mean of EQ2, and (d) the corresponding 1-D mean profile (open circles- true profile, line- guess).

Jumping from lower branch to upper branch

We now wish to demonstrate a second use of the coefficient solver in the context of establishing a connection between lower and upper branch solutions. As discussed in the Introduction, these solutions arise in pairs due to a bifurcation at a critical Reynolds number. If a solution on one of the branches is known, it can be continued back in Reynolds number to the bifurcation point as a means to compute solutions on the other branch. This can sometimes be an expensive process. We are interested more fundamentally in the question of how, for a fixed Reynolds number, the structure of the lower branch solution is related to its upper branch counterpart. Put another way, we ask if we can predict some of the properties (statistical or structural) of the upper branch solution based on the lower branch solution.

We focus on the mean velocity, as this is the pertinent piece of information used in resolvent analysis. We observed in §3.2 that the 2D/3C resolvent framework correctly identified the structure of the highly-amplified fundamental streamwise mode for lower branch solutions; the role of the nonlinearity was to effectively

saturate this amplified mode to the right amplitude such that it could self-interact and sustain the mean velocity. We were curious to explore the effect on the mean velocity in the case that this saturated amplitude was somehow offset; we hypothesized (and will confirm empirically shortly) that the upper branch might be linked to an overly-excited lower branch. We propose investigating this via a slightly modified version of the mean momentum equations

$$\begin{aligned}&\Psi_z\left[\Psi_{yyy}+\Psi_{yzz}\right]-\Psi_y\left[\Psi_{zzz}+\Psi_{yyz}\right]+\frac{1}{Re_\tau}\left[\Psi_{yyyy}+\Psi_{zzzz}+2\Psi_{yyzz}\right]\\&=\alpha\left(\langle f_v\rangle_z-\langle f_w\rangle_y\right),\end{aligned}\tag{3.25}$$

$$-\Psi_z U_y+\Psi_y U_z-\frac{1}{Re_\tau}\left(U_{yy}+U_{zz}\right)=\langle f_u\rangle,\tag{3.26}$$

where we have introduced the scalar $\alpha > 1$ to model an over-amplified mean forcing (here, we leave the mean-u forcing unchanged). We demonstrate this model for the pair EQ1 and EQ2. We solve Equations 3.25-3.26 using the mean forcing for EQ1 and compare the mean velocity field generated to that of EQ2. Figure 3.18 shows this comparison of $U(y, z)$ using a value of $\alpha = 7$, along with a comparison of the 1D profile for the true EQ2 solution and the guess generated from the over-amplified EQ1 solution. We observe strong quantitative agreement between the two, particularly for the 1D profile. Of course, in this process we leveraged the fact that we knew the mean velocity for EQ2 to select the appropriate value of α; nonetheless, we consider this a very interesting result given the simplicity of the model proposed in Equation 3.25. In general, for the discussion above and for what we describe subsequently, one would need to perform a line search to find the appropriate value of α. Though not reported here, we observed similar success of this model for other lower/upper branch pairs (see Appendix).

The implication of this approach is that we may be able to find good approximations to the upper branch 1D mean profile based on the lower branch solution. Once we have a guess for the 1D mean, we can utilize the coefficient solver to attempt to solve for the fluctuating field. We demonstrate this, and to some degree the robustness of the coefficient solver, by using the approximate EQ2 mean profile from Figure 3.18(d). As before, in Figure 3.19 we plot the mean field $\mathbf{U}(y, z)$ for multiple iterations. We see the initial field, based on a random guess of the weights, eventually converges to a field resembling EQ2. In Figure 3.20, we show the sum of the squares of the residuals as a function of iteration count. As with the plot for EQ1 in Figure 3.16, we observe an initial rapid decrease in the residual norm; we confirmed this is mostly driven by the mean constraint. We again used the velocity

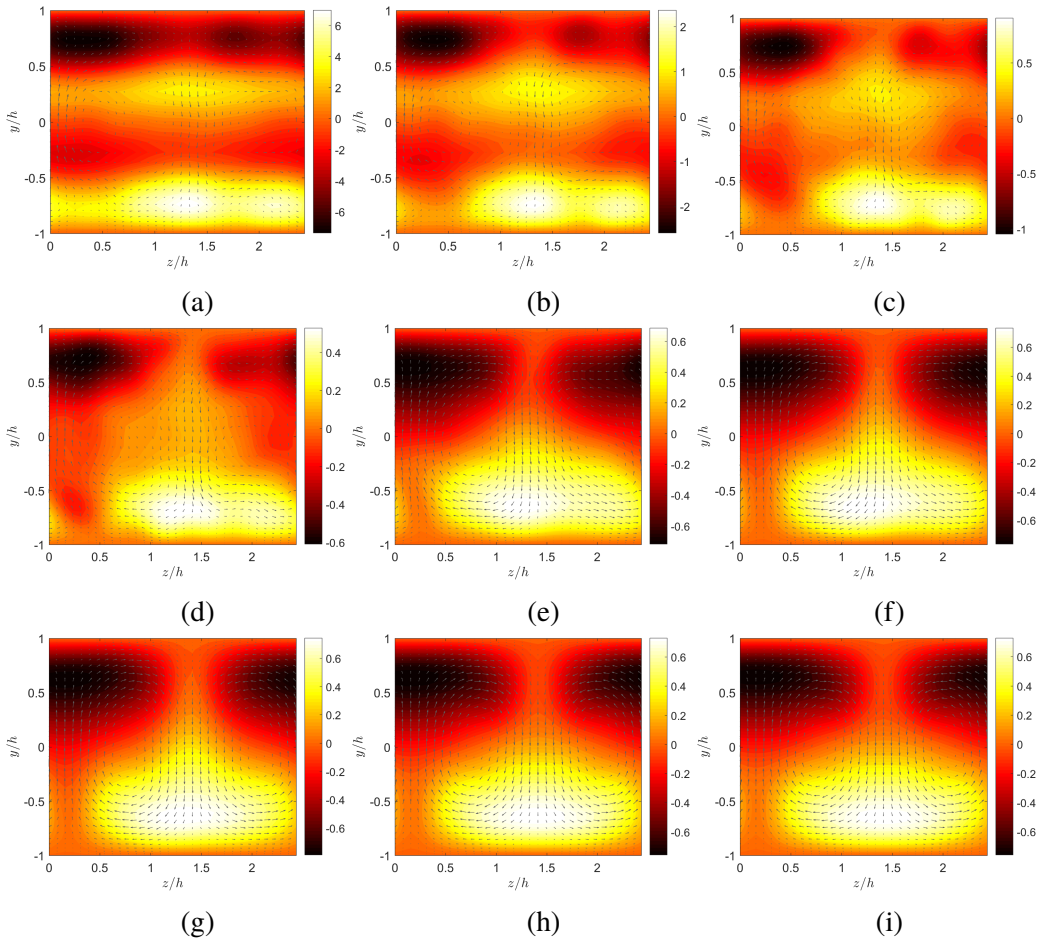

Figure 3.19: The mean velocity field of EQ2 computed using the coefficient solver described in section based on the guess for 1D mean profile show in figure 3.18(d). Here the color contours are the streamwise velocity (deviation from laminar) and the vector arrows represent the spanwise/wall-normal velocity: (a) the initial field based on a random guess of the weights, (b)-(i) iterations 1, 2, 3, 7, 10, 15, 25, and 42 respectively.

field at the final iteration as an input into Channelflow to confirm it converged to the true solution. Also shown in Figure 3.20 is the mean flow obtained from Channelflow; we note its strong quantitative resemblance to Figure 3.19(i). Finally, we compare the statistics from the optimization solution at the final iteration to those of the true solution in Figure 3.21. Broadly speaking, the coefficient solver is able to closely match the true values. We confirmed, by using the true EQ2 mean profile for the coefficient solver, that the small discrepancies observed in the statistics could be partly attributed to the use of the approximate mean (see Appendix). One possible remedy would be to slightly relax the mean constraint; this is a topic of on-going work to improve the robustness of the solver. In addition, one could increase the

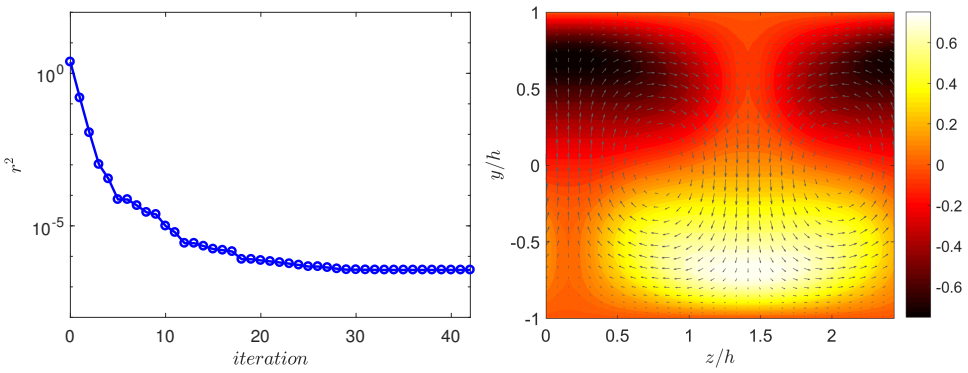

(a) (b)

Figure 3.20: The (a) sum of the squares of the residual vector as a function of iteration count and (b) the converged mean velocity profile for EQ2 (a) computed using the field from the final iteration of the coefficient solver as an input into Channelflow. Note the mean profile is shifted in the spanwise direction relative to the profile in Figure 3.18.

number of singular modes and wavenumbers used to improve the convergence of the residual norm.

Future applications

Looking forward, there are several promising directions for this approach. As has been mentioned previously, the mean profile for EQ2 (and the periodic orbits P19.02 and P87.89) is very similar to the corresponding turbulent profile. Conveniently, in many cases, there exist good models of the turbulent mean velocity for a variety of flows, such as through eddy-viscosity models (Reynolds and Tiederman, 1967). Thus we may use the turbulent profile as a starting point to discover solutions. While we only showed results for equilibria, the coefficient solver approach can also easily be extended to find traveling waves and periodic orbits (though these would require a guess or *a priori* knowledge of the wavespeed or period respectively). Overall, we find it an exciting prospect to generate accurate representations of solutions to the NSE leveraging knowledge only of the mean velocity.

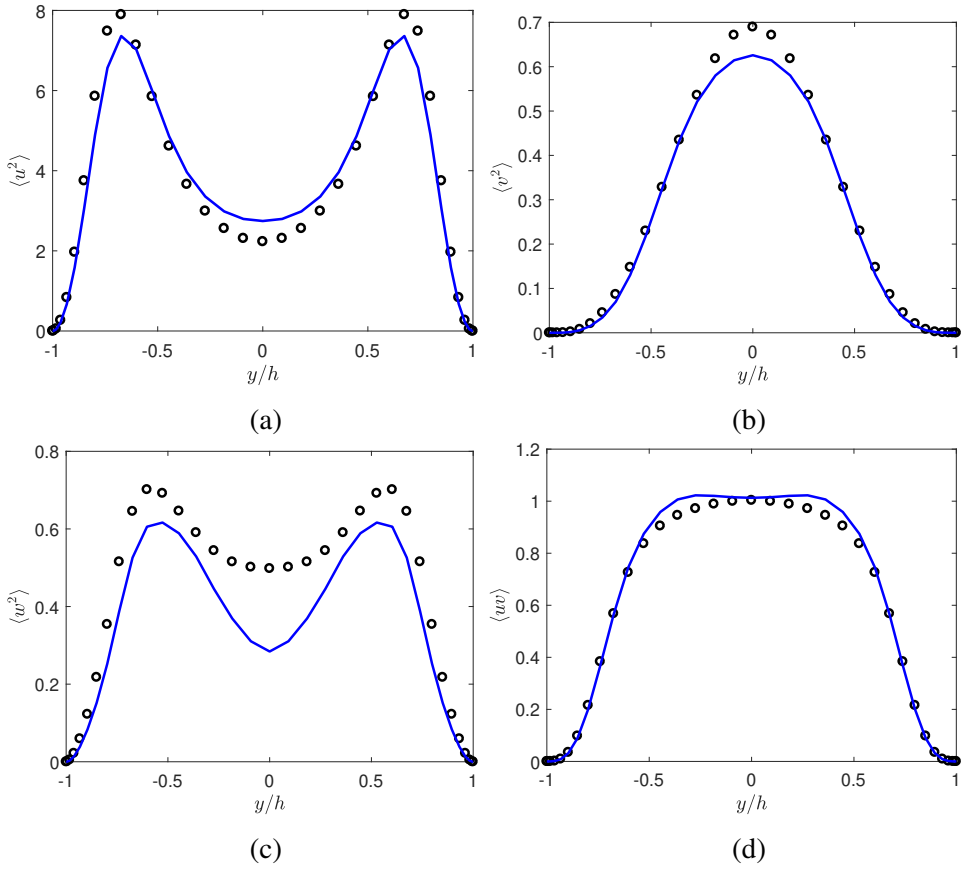

Figure 3.21: Reynolds stress profiles for EQ2 (open circles) and the values based on the solution generated from the coefficient-solver (line) for (a) $\langle u^2 \rangle$, (b) $\langle v^2 \rangle$, (c) $\langle w^2 \rangle$, (d) $\langle uv \rangle$. All quantities are in inner units.

Chapter 4

ANALYSIS OF TURBULENT CHANNEL FLOW

We utilize a constant-time step DNS[1] of a low-Reynolds number turbulent channel flow and characterize the spectral (wavenumber and frequency) content of the velocity/vorticity and forcing fields. In addition, we utilize ideas from §2.2 to plot spectra and statistics for OS/SQ modes. We also explore the behavior of the spectra as a function of wavespeed. We conclude with a brief discussion of future directions for the analysis of this dataset.

4.1 Computation of power spectra

The incompressible NSE were solved numerically in the form of evolution equations for the Laplacian of the wall-normal velocity Δv and the wall-normal vorticity η (Kim et al., 1987; Del Alamo and Jiménez, 2003) in a periodic box of dimensions $L_x/h = 12\pi$ and $L_z/h = 4\pi$ for a friction Reynolds number of $Re_\tau \approx 180$. A comparison of the mean profile and velocity statistics of the present DNS with the database of Del Alamo and Jiménez, 2003 is found in the appendix for validation purposes. The simulation was run for a total time of $Tu_\tau/h \approx 85$; at a sampling time interval of $\Delta t_s u_\tau/h = 0.01482$ ($\Delta t^+ \approx 2.75$), the solution $\Delta\hat{v}(k_x, k_z, y), \hat{\eta}(k_x, k_z, y)$ was saved resulting in a total of ≈ 5800 time snapshots. A summary of the relevant geometrical and discretization parameters is found in Table 4.1. The choice of these

L_x/h	L_z/h	N_x	N_z	N_y	$\frac{\Delta t_s u_\tau}{h}$	$\frac{Tu_\tau}{h}$	Re_τ
12π	4π	512	339	97	0.01482	85	186

Table 4.1: Geometrical parameters and relevant flow properties for the turbulent channel.

time parameters was largely driven in an attempt to resolve the energetic frequency content of the velocity field as outlined in McKeon et al., 2013. Due to the wide range of spatial and temporal scales, it is difficult to fully resolve all fields without generating enormous amounts of data; for the results we will present herein, these

[1]The DNS was performed by A.L. Duràn as part of the 2016 Center for Turbulence Research summer program at Stanford University. A preliminary analysis of the data is found in Rosenberg et al., 2016. We acknowledge discussions with A.L Duràn and A. Towne which helped shaped the content of this chapter. K. Rosenberg performed the analysis and wrote the discussion for this chapter.

sampling parameters offered an appropriate trade-off between sufficient temporal resolution and tractable dataset size.

We wish to analyze the spectral behavior of the velocity/vorticity fields as well as the nonlinear forcing. With $\Delta\hat{v}(k_x, k_z, y; t)$ and $\hat{\eta}(k_x, k_z, y; t)$, we can recover the primitive velocity components $\hat{\mathbf{u}}(k_x, k_z, y; t)$ using the relation in Equation 2.24. Once we have $\hat{\mathbf{u}}(k_x, k_z, y; t)$, we can compute (at each time step) the nonlinearity $\hat{\mathbf{f}}(k_x, k_z, y; t)$. As mentioned in §2.4.1, we evaluate the nonlinear term pseudospectrally (Canuto et al., 1988) for computational efficiency. In addition, to maintain consistency with the approach utilized in the DNS, we use the rotational form of the nonlinearity

$$\mathbf{f} = \mathbf{u} \times \boldsymbol{\omega} - \frac{1}{2}\nabla \mathbf{u}^2, \tag{4.1}$$

where $\boldsymbol{\omega}$ is the vorticity (not to be confused with the frequency ω). The second term is absorbed into the pressure (which is subsequently eliminated) and need not be computed. In this chapter, we will focus our attention on the solenoidal forcing components f_{v_s} and f_η which arise in the normal velocity/vorticity formulation of the equations; we compute these components by substituting the forcing $\hat{\mathbf{f}}$ computed in Equation 4.1 (Fourier transformed in x and z) into the expression in Equation 2.38.

Once we have all the velocity/vorticity/forcing time-series data of interest (each as a function of (k_x, k_z, y)), we can now compute power spectra for each field. Given the statistical homogeneity in x and z, we are in the fortunate position that we can compute the spectra for each wavenumber pair (k_x, k_z) independently. Let us consider, for a given (k_x, k_z) and wall-normal height, a particular time-series of interest $\Theta(t)$ where Θ is for instance a velocity or forcing component. As is commonly done in the analysis of (non-periodic) time-series data in turbulent flows, we estimate the power spectrum using Welch's method (Welch, 1967). This method divides the time-series into m overlapping windowed segments

$$\Theta_i(t) = \Theta(t)W(t), \tag{4.2}$$

where $W(t)$ is a window function and $i = 1, ..., m$ denotes the segment index. Here we use a Hanning window with 50% overlap and $m = 10$ overlapping segments. The power spectrum is then computed as

$$P_{\Theta\Theta}(\omega) = \frac{1}{m}\sum_{i=1}^{m} \hat{\Theta}_i(\omega)\hat{\Theta}_i^*(\omega) \tag{4.3}$$

where $\hat{\Theta}_i(\omega)$ is the discrete Fourier transform of $\Theta_i(t)$. The choice of $m = 10$ was found to yield a good convergence in Equation 4.3 without excessively sacrificing frequency resolution; here, the frequencies take on discrete values between $\omega_{min} = 0$ and $\omega_{max} \approx 211h/u_\tau$ in intervals of $\Delta\omega \approx 0.74h/u_\tau$. It was confirmed that doubling m did not yield significant quantitative differences (see Appendix). The MATLAB function *pwelch* is used to compute (across all wavenumbers and wall-normal heights) $P_{\Theta\Theta}(k_x, k_z, \omega; y)$. In what follows, we will present several 2D views of the power spectrum by integrating over one of the wavenumber/frequency directions. For instance, the 2D $(k_x - \omega)$ spectrum (for a fixed wall-normal height) is computed as

$$P_{\Theta\Theta}(k_x, \omega; y) = \int_{-\infty}^{\infty} P_{\Theta\Theta}(k_x, k_z, \omega; y)\mathrm{d}k_z. \tag{4.4}$$

The corresponding 2D pre-multiplied spectrum is $k_x\omega P_{\Theta\Theta}(k_x, \omega; y)$ with the multiplying factors analogously being $k_z\omega$ and $k_x k_z$ in the $(k_z - \omega)$ and $(k_x - k_z)$ planes respectively. Furthermore, we note the variance is recovered by integrating across all wavenumbers and frequencies,

$$\langle\Theta^2\rangle = \iiint_{-\infty}^{\infty} P_{\Theta\Theta}(k_x, k_z, \omega; y)\mathrm{d}k_x\mathrm{d}k_z\mathrm{d}\omega. \tag{4.5}$$

We will also make use of the cross power spectrum, which is defined as

$$C_{\Theta\Theta}(y_r, y_s; \omega) = \frac{1}{m}\sum_{i=1}^{m} \hat{\Theta}_i(y_r; \omega)\hat{\Theta}_i^*(y_s; \omega), \tag{4.6}$$

where y_r and y_s denote the wall-normal location for a given index. This is similarly calculated in MATLAB using the function *cpsd*.

4.1.1 Forcing Spectra

We begin by presenting results for the forcing components f_{v_s} and f_η. We reiterate that, to the author's knowledge, a direct characterization of the nonlinear forcing from DNS of a turbulent channel has not been previously performed. To get a sense of where the forcing is concentrated across the height of the channel, we first plot the variance of these components $\langle {f_{v_s}}^2\rangle$, $\langle {f_\eta}^2\rangle$ as shown in Figure 4.1. Both components appear to be active near the wall, with $\langle {f_\eta}^2\rangle$ sharply peaking at $y^+ \approx 15$, the well known wall-normal location associated with the near-wall-cycle (Smits et al., 2011). $\langle {f_{v_s}}^2\rangle$ peaks slightly further away at $y^+ \approx 40$ and has a broader signature across the height of the channel. We next examine the wavenumber/frequency dependence of the power spectra for these forcing components. Of particular interest is the behavior of the forcing in the frequency domain; as discussed in the Introduction,

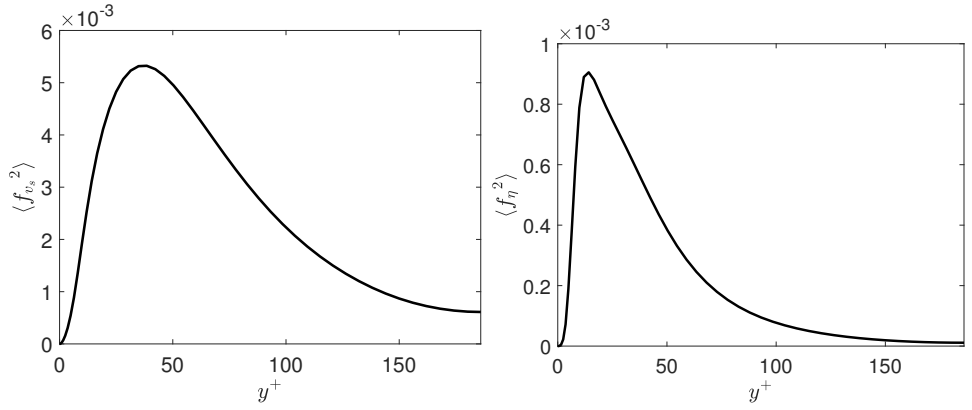

(a) (b)

Figure 4.1: Variance profiles for (a) f_{v_s} and (b) f_η as a function of wall-normal height. All quantities are in inner units.

attempts to the model the forcing term via stochastic methods have evoked varying assumptions on its spectral structure. We will restrict our attention to a fixed wall-normal height of $y^+ \approx 15$. Figure 4.2 shows 2D power spectra in the $k_x - \omega$, $k_z - \omega$, and $k_x - k_z$ planes for f_{v_s} and f_η. Clearly the forcing components have a well-defined structure with a non-trivial variation in the frequency plane. This is consistent with the recent findings of Zare et al., 2017, who found the forcing must be colored in time to accurately reproduce second order statistics. Though they do not report forcing spectra, it would be noteworthy to compare if similar trends are observed. The concentration of the forcing activity along a diagonal in the $k_x - \omega$ plane, particularly prominent for f_{v_s}, indicates the presence of a dominant wavespeed. For point of reference, a dashed line denoting the local mean velocity is also shown in Figure 4.2; it appears the forcing activity occurs at slightly higher wavespeeds relative to this value. The localizing role of the wavespeed will be discussed in further detail later in this chapter for the streamwise velocity. In the wavenumber plane, both forcing components show energetic activity centered around the spanwise length scale of $k_z h \approx 20$ ($\lambda_z^+ \approx 60$) which is slightly more narrow than the classically reported width of $\lambda_z^+ \approx 100$ for the near-wall streaks. While it appears we have mostly resolved the structure of these forcing components, a slightly higher sampling frequency is required to fully capture all the content. In the $k_x - \omega$ plane, based on the Nyquist sampling frequency f_s and using the mean centerline velocity U_{cl} as a bounding wavespeed, we might expect aliasing effects beyond a wavenumber of $k_x = \frac{\pi f_s}{U_{cl}} \approx 12$. While small spurious effects are observed with the forcing spectra for high k_x (see Figure 4.2(a)), they are less pronounced in

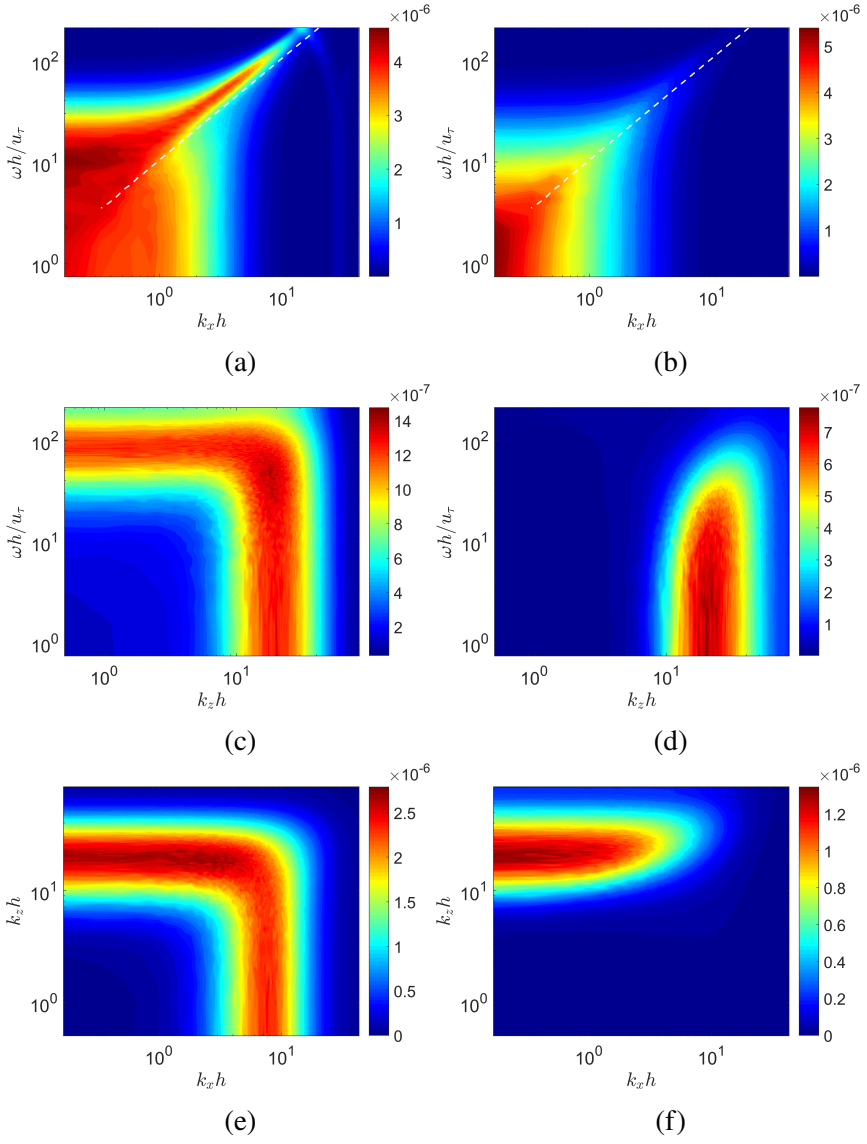

Figure 4.2: 2D spectra at a fixed wall normal height of $y^+ \approx 15$ for f_{v_s} (left column) and f_η (right column) plotted in the (a),(b) k_x-ω plane, (c),(d) k_z-ω plane, and the (e),(f) k_x-k_z plane. The dashed line in the k_x-ω plane denotes the wavespeed of the local mean $U(y^+ \approx 15)$.

the velocity and vorticity spectra presented in the next section, and so we believe the influences to be minimal. Future studies will utilize a higher sampling frequency to confirm these notions; we emphasize that the DNS time-step was sufficiently small such that the actual simulation was not corrupted by aliasing effects.

4.2 OS/SQ spectra

Given the utility of the decomposition of the velocity field into OS/SQ modes for the ECS solutions, we were curious to explore if any of the observed trends were also seen in a fully turbulent flow. We recall that we express the total wall-normal vorticity as the sum of the OS and SQ components

$$\eta = \eta_{\text{os}} + \eta_{\text{sq}}, \tag{4.7}$$

which are defined (in the Fourier domain) as

$$\begin{aligned} \hat{\eta}_{\text{os}}(k_x, k_z, \omega; y) &= -ik_z \mathcal{H}_{\eta\eta}(k_x, k_z, \omega) U_y \hat{v}(k_x, k_z, \omega; y) \\ \hat{\eta}_{\text{sq}}(k_x, k_z, \omega; y) &= \mathcal{H}_{\eta\eta}(k_x, k_z, \omega) \hat{f}_\eta(k_x, k_z, \omega; y), \end{aligned} \tag{4.8}$$

where $\mathcal{H}_{\eta\eta}$ is defined in Equation 2.27. We can then express the corresponding power spectra as

$$\begin{aligned} P_{\eta_{\text{os}}\eta_{\text{os}}}(k_x, k_z, \omega; y) &= diag\left\{\mathcal{G}(k_x, k_z, \omega) C_{vv}(k_x, k_z, \omega; y) \mathcal{G}(k_x, k_z, \omega)^H\right\} \\ P_{\eta_{\text{sq}}\eta_{\text{sq}}}(k_x, k_z, \omega; y) &= diag\left\{\mathcal{H}_{\eta\eta}(k_x, k_z, \omega) C_{f_\eta f_\eta}(k_x, k_z, \omega; y) \mathcal{H}_{\eta\eta}(k_x, k_z, \omega)^H\right\}, \end{aligned} \tag{4.9}$$

where C_{vv} and $C_{f_\eta f_\eta}$ are the cross spectra of v and f_η respectively, $\mathcal{G}$ is given by

$$\mathcal{G}(k_x, k_z, \omega) = -ik_z \mathcal{H}_{\eta\eta}(k_x, k_z, \omega) U_y, \tag{4.10}$$

and diag {} denotes keeping only the diagonal elements. Thus, independently for all (k_x, k_z) pairs, we first compute the cross spectra terms and then form the matrices $\mathcal{H}_{\eta\eta}$ and $\mathcal{G}$ at each discrete frequency; computation of these matrices requires the turbulent mean $U(y)$ which we obtain directly from the simulation.

In Figure 4.3, we plot the 2D (pre-multiplied) power spectra in the $k_x - \omega$, $k_z - \omega$, and $k_x - k_z$ planes for the total wall-normal vorticity η and the η_{os}, η_{sq} components at a fixed-wall normal height of $y^+ \approx 15$. We observe that both the OS and SQ components are larger in magnitude than the total vorticity, with η_{os} being the dominant component. Despite the slightly different amplitudes, the OS and SQ components appear to have very similarly shaped spectra. Interestingly, we see the peak in the OS/SQ spectra with regards to streamwise wavenumber is shifted towards smaller values (longer wavelengths) relative to full vorticity. We note that η_{os} is generated by the interaction of v with the mean shear via the lift-up effect (see Equation 4.8), an effect known (in a linear context) to give rise to highly-amplified streamwise-elongated structures; this may possibly explain the observed shift to

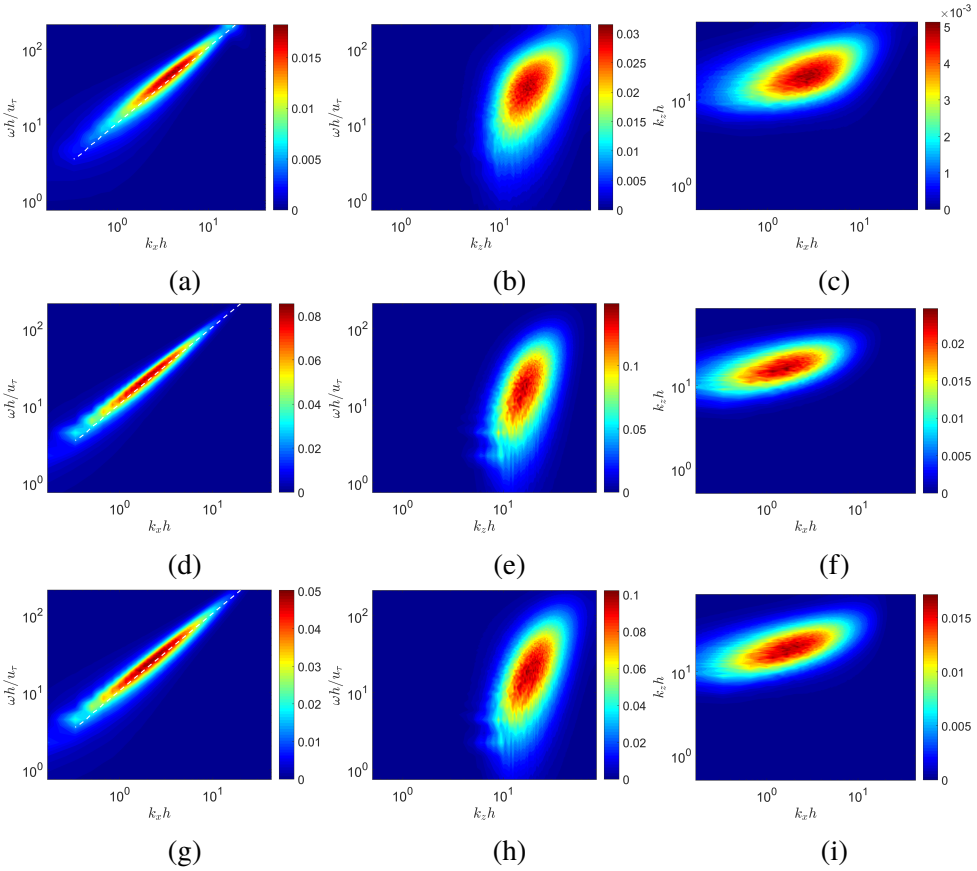

Figure 4.3: 2D pre-multiplied spectra at a fixed wall normal height of $y^+ \approx 15$ for η (top row), η_{os} (middle row), and η_{sq} (bottom row) plotted in the (a),(d),(g) k_x-ω plane, (b),(e),(h) k_z-ω plane, and the (c),(f),(i) k_x-k_z plane. The dashed line in the k_x-ω plane denotes the wavespeed of the local mean $U(y^+ \approx 15)$.

longer wavelengths. Consequently, we posit the OS vorticity, amplified via a linear mechanism, must be suppressed to a certain extent by the SQ vorticity (i.e. the phase between them is important). We support this claim further by plotting the contributions to the variance of the vorticity from OS/SQ modes across the height of the channel,

$$\langle \eta^2 \rangle = \langle {\eta_{os}}^2 \rangle + \langle {\eta_{sq}}^2 \rangle + 2\langle \eta_{os}\eta_{sq} \rangle, \tag{4.11}$$

as seen in Figure 4.4. Similar to the results observed in Figure 3.4 for P4U, we see a necessarily strong anti-correlation between the OS/SQ modes to balance the large generation of vorticity from OS modes. Recasting Equations 4.7-4.8 in a slightly different form, we have

$$\hat{\eta} = \mathcal{H}_{\eta\eta}\left(\hat{f}_\eta - ik_z U_y \hat{v}\right). \tag{4.12}$$

Given the similarity in the shape of the OS/SQ spectra, it stands to reason from the expression above that the two terms in the parentheses (the first one generating

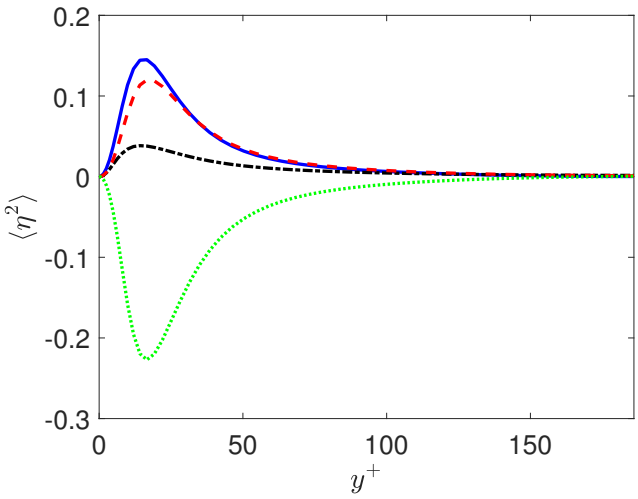

(a)

Figure 4.4: Contributions to the total $\langle \eta^2 \rangle$ (dash-dot line) from OS modes (solid line), SQ modes (dashed line), and twice their covariance (dotted line). All quantities are in inner units.

η_{SQ} and the second one η_{OS}) might also share a similar spectral signature. This is an intriguing prospect from a modeling perspective as it may suggest the forcing spectra can be directly related to the velocity spectra. In Figure 4.5, we plot the 2D spectra of this second term in parentheses (i.e. $k_z^2 U_y^2 P_{vv}$) at $y^+ \approx 15$ in the wavenumber-frequency planes. While the magnitudes are slightly different, we note the striking similarity between $k_z^2 U_y^2 P_{vv}$ and $P_{f_\eta f_\eta}$ from figure 4.2 (right column). Interestingly, a similar connection between the forcing spectra and the kinetic energy spectra has been observed for a turbulent jet (Towne et al., 2017b).

4.3 Identifying energetic wavespeeds

The role of wavespeed in turbulent flows has been of interest both in experimental and theoretical contexts. In experimental measurements, Taylor's hypothesis (Taylor, 1938) is often invoked to convert from the temporal domain to the spatial domain under the assumption of a constant convection velocity associated with the turbulent mean. In classical linear stability analysis, traveling wave disturbances are known to localize around the critical layer, the location where the wavespeed of the disturbance matches that of the base flow. Recent works by McKeon and Sharma, 2010 and Hall and Sherwin, 2010 have demonstrated the relevance of critical layers in turbulent flows.

Here, we are interested in identifying the energetically relevant wavespeeds from

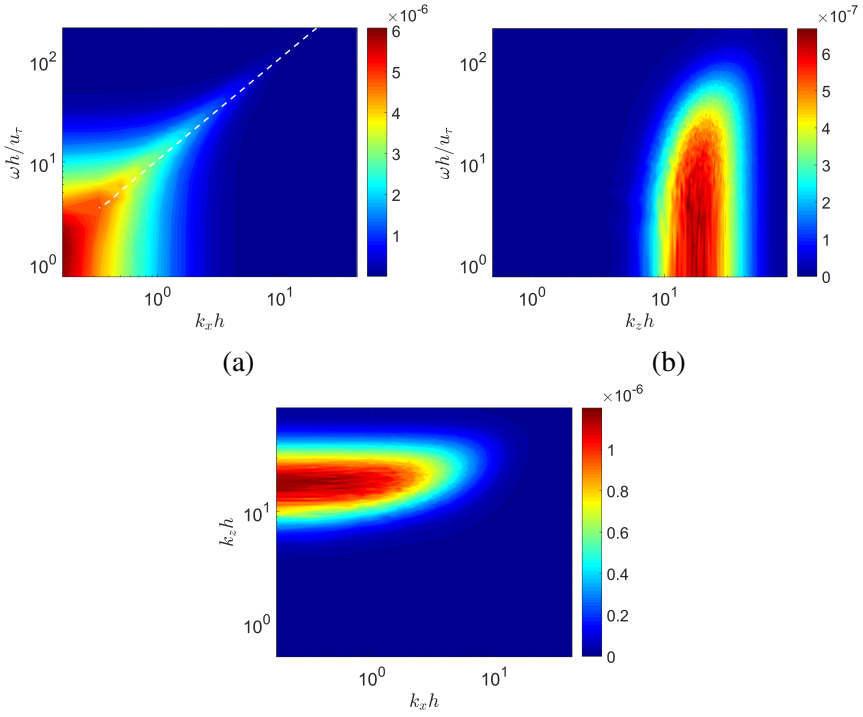

Figure 4.5: 2D spectra at $y^+ \approx 15$ of $k_z^2 {U_y}^2 P_{vv}$ plotted in the (a) k_x-ω plane, (b) k_z-ω plane, and the (c) k_x-k_z plane. The dashed line in the k_x-ω plane denotes the wavespeed of the local mean $U(y^+ \approx 15)$. We note its similarity in structure to the spectra of f_η shown in Figure 4.2.

velocity spectra, and their variation across the height of the channel. We will focus on the streamwise velocity, as this has been the most studied experimentally and numerically. In Figure 4.6, we plot the 2D (pre-multiplied) spectra $P_{uu}(k_x, \omega)$ for various wall-normal heights. We also superimpose on each plot a dashed line corresponding to the local mean velocity. We note that the energetic activity very close to the wall is concentrated at wavespeeds that are larger than the local mean. This is consistent with the observations of Del Álamo and Jiménez, 2009 and the associated breakdown in the validity of Taylor's hypothesis. As we move further away from the wall, the energy becomes increasingly confined to a smaller range of wavespeeds and is centered about the local mean. Similar trends were also observed in the experimental measurements of $P_{uu}(k_x, \omega)$ in a turbulent boundary layer by LeHew et al., 2011.

To get an integrated sense of the energetic wavespeeds across the height of the

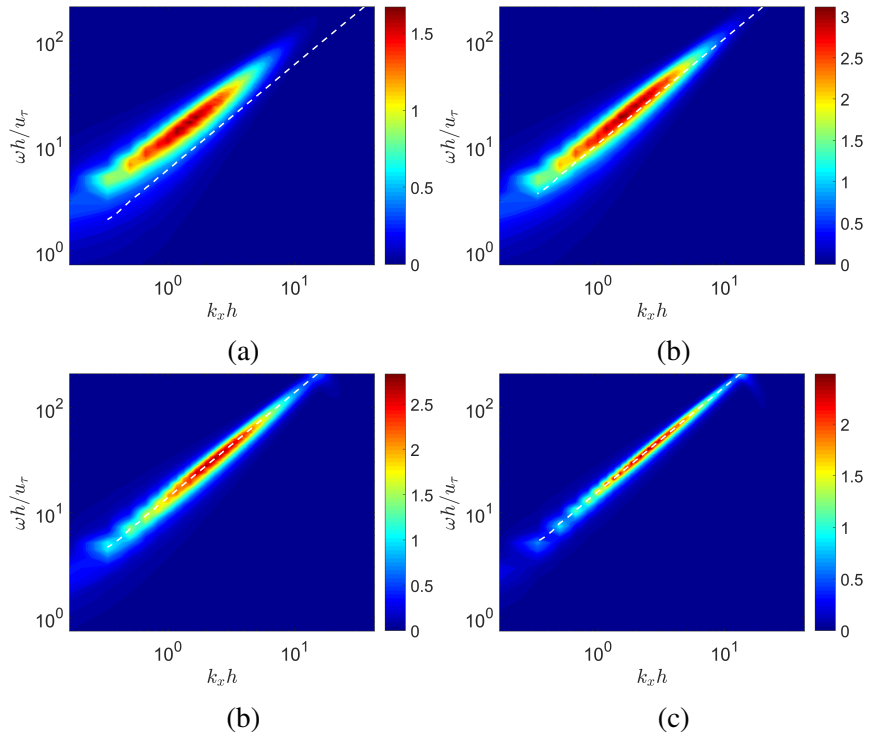

Figure 4.6: 2D pre-multiplied power spectrum of the streamwise velocity in the k_x-ω plane for (a) $y^+ \approx 6$, (b) $y^+ \approx 15$, (c) $y^+ \approx 31$, and (d) $y^+ \approx 64$. The dashed lines denote the wavespeed corresponding to the local mean velocity at each wall-normal height.

channel, we compute the 1D spectrum $P_{uu}(c; y)$ as

$$P_{uu}(c; y) = \iint_{-\infty}^{\infty} k_x P_{uu}(k_x, k_z, c; y) \mathrm{d}k_x \mathrm{d}k_z. \tag{4.13}$$

The k_x in the integrand arises from the change of variable from ω to $c = \frac{\omega}{k_x}$ such that when $P_{uu}(c; y)$ is integrated across wavespeed it returns the variance $\langle u^2 \rangle$. We obtain $P_{uu}(k_x, k_z, c; y)$ by interpolating the computed power spectrum $P_{uu}(k_x, k_z, \omega; y)$ onto a common wavespeed vector for each (k_x, ω) pair; here we use 288 linearly-spaced wavespeeds between 0 and the mean centerline velocity. In Figure 4.7, we plot $P_{uu}(c; y)$ and superimpose on it the turbulent mean velocity. Consistent with results presented in Figure 4.6, we observe a wide range of active wavespeeds close to the wall with the well-known peak at $y^+ \approx 15$ and a subsequent narrowing of active wavespeeds further from the wall. We note the 1D spectrum $P_{uu}(c; y)$ has also been reported in Zare et al., 2017 for the same Reynolds number and in Moarref et al., 2013 for $Re_\tau = 2000$. However, we emphasize both of these were model-based computations; we believe the direct computation of $P_{uu}(c; y)$ from DNS data has not been previously reported. Interestingly, there appear to be discrepancies between

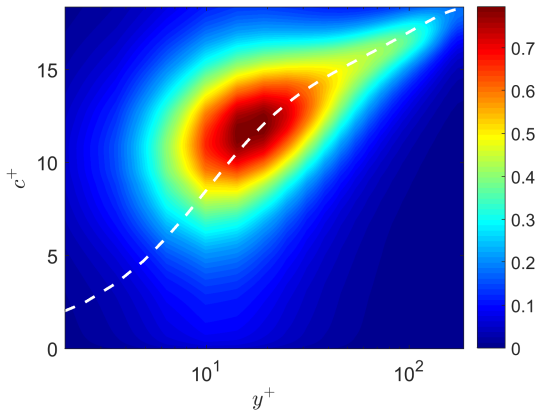

(a)

Figure 4.7: The 1D power spectrum of the streamwise velocity as a function of wavespeed c^+ and wall-normal height y^+ with the mean profile (dashed line) superimposed.

the model-based computations and the spectrum presented in Figure 4.7 and thus merits further investigation. Given the availability of data for the other velocity components that is often difficult to obtain from experiments, we also report the 1D spectra for v, w, and uv as a function of wavespeed in Figure 4.8. We observe that the energetically dominant wavespeeds appear to be slightly faster in comparison to u, particularly for v. We also note the energetic activity appears to be highly localized around the mean velocity; from a modeling perspective, this seems to bolster the argument that the wavespeed c, as opposed to the frequency ω, may be more a relevant parameter in the analysis of turbulent flows as suggested in Moarref et al., 2013.

4.4 Future directions

In this chapter, we focused on characterizing the spectra of the velocity/vorticity and forcing fields in the full wavenumber/frequency domain as these had not been thoroughly analyzed in the literature, especially for the forcing. As mentioned previously, it would be noteworthy to further compare these results to the recent model-based developments of Zare et al., 2017.

Looking forward, we are interested in computing reduced-order representations of these flow fields using techniques such as resolvent analysis, proper orthogonal decomposition, and the recently proposed spectral proper orthogonal decomposition (Towne et al., 2017a). In addition, we think it would be worthwhile to perform these decompositions in light of the proposed split into OS and SQ modes as

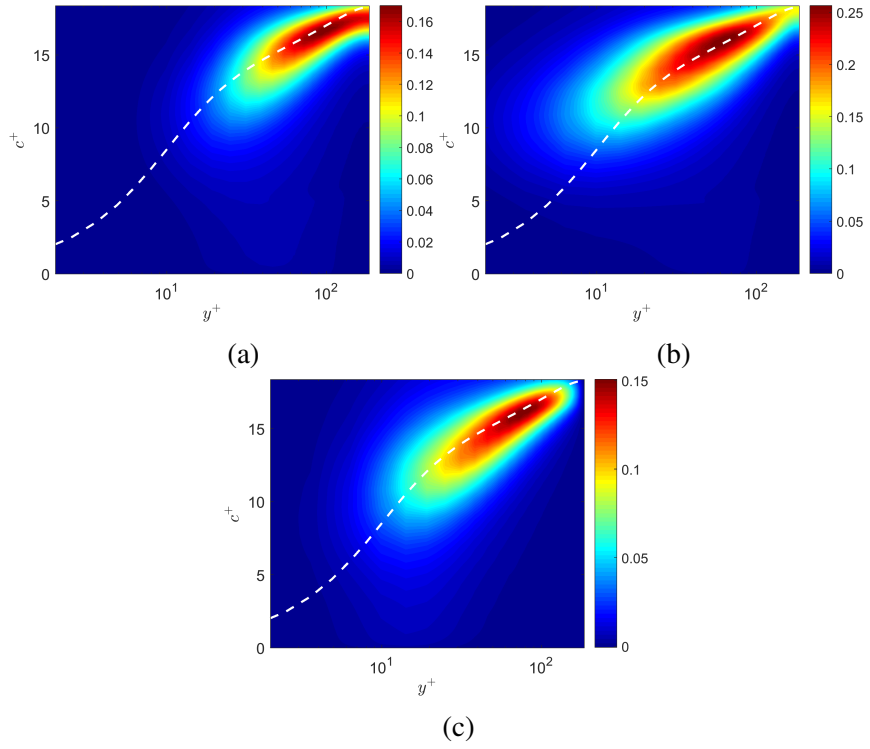

Figure 4.8: The 1D power spectra of the (a) wall-normal velocity v, (b) spanwise velocity w, and (c) Reynolds shear stress $\langle uv \rangle$ as a function of wavespeed c^+ and wall-normal height y^+ with the mean profile (dashed line) superimposed.

a possible means to improve the convergence of these low-order representations. Interestingly, this has been previously explored in a somewhat related context for POD by transforming into a coordinate system locally aligned with the wavenumber vector (Juttijudata et al., 2005). In this coordinate system, the decomposition into the so-called 'plus-modes' (aligned with the wave vector) and 'minus-modes' (perpendicular to the wave vector) (Moser et al., 1983) appeared to provide improved convergence properties with respect to the traditional POD approach. In general, a thorough comparison of the various data-driven and operator-driven techniques (Taira et al., 2017), particularly in light of the availability of frequency-resolved data, would be a valuable contribution to the continuing development of low-order models of turbulent channel flow.

Chapter 5

CONCLUSIONS AND FUTURE WORK

This thesis focused on the advancement of the resolvent framework to model wall-bounded turbulent flows. Herein we summarize the key contributions and make suggestions for possible future studies.

The first key contribution was the splitting of the decomposition of the resolvent operator into a family of OS and SQ response modes, an approach whose motivation stemmed from the analogous formulation in classical linear stability. Using various ECS solutions (equilibria, traveling waves, and periodic orbits) in Poiseuille and Couette flow, we clearly demonstrated the improved compact representation of the velocity field gained with the modified OS/SQ approach in comparison with the traditional method. Notably, we were able to obtain a low-dimensional representation of the wall-normal velocity v which had been visibly lacking with the previous approach. We also showed, using a Helmholtz decomposition of the nonlinear forcing, the significance of the solenoidal component for incompressible flows. The notion of only the solenoidal forcing component being 'active' in a sense, as illustrated in Figure 2.2, may have interesting implications in terms of modeling Reynolds stresses, as touched upon by Jimènez, 2016.

The next contribution was an extension of the resolvent framework to the analysis of 2D/3C mean flows. Though the associated resolvent operator was significantly more complicated, its decomposition led to some interesting results. Namely, it revealed for lower branch ECS that the fundamental streamwise Fourier mode could be accurately represented by the leading response mode of the resolvent operator; furthermore, the interaction of this single mode with itself could sustain the mean profile and thus close the system. It was observed that the dominance of the associated leading singular value (often an order of magnitude larger than the second singular value) enabled this representation with a single response mode. For upper branch ECS, a strong separation in singular values was not observed and thus did not allow for accurate representation with the leading mode; we attributed this behavior as partly due to the slightly more complicated scale interactions which sustain these solutions.

We then demonstrated with these contributions various novel methods to compute

ECS. With the 2D/3C resolvent framework, we showed we could compute an accurate representation of an ECS solution starting from a laminar profile using an iterative procedure (rooted in the vision of the self-sustaining process) which required the specification of a single unknown parameter. From the 1D analysis and the efficient basis obtained from the OS/SQ decomposition, we developed a method based on interaction coefficients to solve for the unknown weights using only knowledge of the mean profile. While we focused our results on equilibria in Couette flow, these techniques can easily be extended to the computation of periodic orbits in various geometries and is a topic of ongoing work. We also demonstrated interesting connections between the mean profiles of the lower and upper branch solution and suggested a simple model to jump from one to the other. This procedure, coupled with the coefficient solver, could potentially provide significant computational savings as it would avoid the need to continue the solutions back to their bifurcation point. Moreover, these resolvent-based solution methods, which do not require explicit time-integration of the NSE, may prove to be more efficient going forward in the computation of ECS for higher Reynolds numbers.

Finally, the last key contribution was a direct characterization of the nonlinear forcing in a turbulent channel flow via a constant time-step DNS. By analyzing the power spectra of the forcing, we observed a clear signature in the wavenumber/frequency planes confirming notions about the underlying structure of the forcing as suggested by Zare et al., 2017. We also computed spectra of the OS/SQ components of the vorticity and observed similar competing effects between the two that were also present in the ECS solutions. Also from this decomposition, we were able to establish a possible connection between the spectra of the wall-normal vorticity forcing and wall-normal velocity spectra which could serve useful for modeling purposes. Looking forward, the OS/SQ decomposition in general may prove useful in the analysis of fully turbulent flows and their low dimensional representation, and thus remains a subject of ongoing work.

BIBLIOGRAPHY

Ahmed, M.A. and Sharma, A.S. (2017). "New equilibrium solution branches of plane Couette flow discovered using a project-then-search method". In: *arXiv preprint arXiv:1706.05312*.

Aubry, N., Holmes, P., Lumley, J.L., and Stone, E. (1988). "The dynamics of coherent structures in the wall region of a turbulent boundary layer". In: *Journal of Fluid Mechanics* 192, pp. 115–173.

Barkley, D. (2006). "Linear analysis of the cylinder wake mean flow". In: *EPL (Europhysics Letters)* 75.5, p. 750.

Beneddine, S., Sipp, D., Arnault, A., Dandois, J., and Lesshafft, L. (2016). "Conditions for validity of mean flow stability analysis". In: *Journal of Fluid Mechanics* 798, pp. 485–504.

Bjorck, Ake (1996). *Numerical methods for least squares problems*. Siam.

Butler, K.M. and Farrell, B.F. (1992). "Three-dimensional optimal perturbations in viscous shear flow". In: *Physics of Fluids A: Fluid Dynamics* 4.8, pp. 1637–1650.

Canuto, Claudio, Hussaini, M Yousuff, Quarteroni, Alfio, Thomas Jr, A, et al. (1988). *Spectral methods in fluid dynamics*. Springer Science & Business Media.

Choi, Haecheon and Moin, Parviz (1990). "On the space-time characteristics of wall-pressure fluctuations". In: *Physics of Fluids A: Fluid Dynamics* 2.8, pp. 1450–1460.

Del Alamo, J.C. and Jiménez, J. (2003). "Spectra of the very large anisotropic scales in turbulent channels". In: *Physics of Fluids* 15.6, pp. L41–L44.

Del Álamo, J.C. and Jiménez, J. (2006). "Linear energy amplification in turbulent channels". In: *Journal of Fluid Mechanics* 559, pp. 205–213.

Del Álamo, J.C. and Jiménez, J. (2009). "Estimation of turbulent convection velocities and corrections to Taylor's approximation". In: *Journal of Fluid Mechanics* 640, pp. 5–26.

Drazin, P.G. and Reid, W.H. (1981). *Hydrodynamic stability*. Cambridge university press.

Ehrenstein, U. and Koch, W. (1991). "Three-dimensional wavelike equilibrium states in plane Poiseuille flow". In: *Journal of fluid mechanics* 228, pp. 111–148.

Farrell, B.F. (1988). "Optimal excitation of perturbations in viscous shear flow". In: *Physics of Fluids* 31.8, pp. 2093–2102.

Farrell, B.F. and Ioannou, P.J. (1993). "Stochastic forcing of the linearized Navier–Stokes equations". In: *Physics of Fluids A: Fluid Dynamics* 5.11, pp. 2600–2609.

Farrell, B.F. and Ioannou, P.J. (2012). “Dynamics of streamwise rolls and streaks in turbulent wall-bounded shear flow”. In: *Journal of Fluid Mechanics* 708, pp. 149–196.

Farrell, B.F., Ioannou, P.J., Jiménez, J., Constantinou, N.C., Lozano-Durán, A., and Nikolaidis, M. (2016). “A statistical state dynamics-based study of the structure and mechanism of large-scale motions in plane Poiseuille flow”. In: *Journal of Fluid Mechanics* 809, pp. 290–315.

Gayme, D.F., McKeon, B.J., Papachristodoulou, A., Bamieh, B., and Doyle, J.C. (2010). “A streamwise constant model of turbulence in plane Couette flow”. In: *Journal of Fluid Mechanics* 665, pp. 99–119.

Gibson, J.F., Halcrow, J., and Cvitanović, P. (2008). “Visualizing the geometry of state space in plane Couette flow”. In: *Journal of Fluid Mechanics* 611, pp. 107–130.

Gibson, J.F., Halcrow, J., and Cvitanović, P. (2009). “Equilibrium and travelling-wave solutions of plane Couette flow”. In: *Journal of Fluid Mechanics* 638, pp. 243–266.

Hall, P. and Sherwin, S. (2010). “Streamwise vortices in shear flows: harbingers of transition and the skeleton of coherent structures”. In: *Journal of Fluid Mechanics* 661, pp. 178–205.

Herbert, T. (1977). “Die neutrale Fläche der ebenen Poiseuille-Strömung”. PhD thesis.

Hwang, Y. and Cossu, C. (2010). “Linear non-normal energy amplification of harmonic and stochastic forcing in the turbulent channel flow”. In: *Journal of Fluid Mechanics* 664, pp. 51–73.

Ilak, M. and Rowley, C.W. (2008). “Modeling of transitional channel flow using balanced proper orthogonal decomposition”. In: *Physics of Fluids* 20.3, p. 034103.

Jiménez, J. (2013). “How linear is wall-bounded turbulence?” In: *Physics of Fluids* 25.11, p. 110814.

Jiménez, J. (2018). “Coherent structures in wall-bounded turbulence”. In: *Journal of Fluid Mechanics* 842.

Jimènez, J. (2016). “Optimal fluxes and Reynolds stresses”. In: *J. Fluid Mech.* 809, pp. 585–600.

Jovanović, M.R. and Bamieh, B. (2005). “Componentwise energy amplification in channel flows”. In: *Journal of Fluid Mechanics* 534, pp. 145–183.

Juttijudata, Vejapong, Lumley, John L, and Rempfer, Dietmar (2005). “Proper orthogonal decomposition in Squire’s coordinate system for dynamical models of channel turbulence”. In: *Journal of Fluid Mechanics* 534, pp. 195–225.

Kawahara, G., Uhlmann, M., and Van Veen, L. (2012). "The significance of simple invariant solutions in turbulent flows". In: *Annual Review of Fluid Mechanics* 44, pp. 203–225.

Kim, J. (2011). "Physics and control of wall turbulence for drag reduction". In: *Philosophical Transactions of the Royal Society of London A: Mathematical, Physical and Engineering Sciences* 369.1940, pp. 1396–1411.

Kim, J. and Lim, J. (2000). "A linear process in wall-bounded turbulent shear flows". In: *Physics of Fluids* 12.8, pp. 1885–1888.

Kim, J., Moin, P., and Moser, R. (1987). "Turbulence statistics in fully developed channel flow at low Reynolds number". In: *Journal of Fluid Mechanics* 177, pp. 133–166.

Kline, S.J., Reynolds, W.C., Schraub, F.A., and Runstadler, P.W. (1967). "The structure of turbulent boundary layers". In: *Journal of Fluid Mechanics* 30.4, pp. 741–773.

LeHew, J., Guala, M., and McKeon, B.J. (2011). "A study of the three-dimensional spectral energy distribution in a zero pressure gradient turbulent boundary layer". In: *Experiments in fluids* 51.4, pp. 997–1012.

Luhar, M., Sharma, A.S., and McKeon, B.J. (2014). "Opposition control within the resolvent analysis framework". In: *Journal of Fluid Mechanics* 749, pp. 597–626.

Luhar, M., Sharma, A.S., and McKeon, B.J. (2015). "A framework for studying the effect of compliant surfaces on wall turbulence". In: *Journal of Fluid Mechanics* 768, pp. 415–441.

Lumley, J.L. (1967). "The structure of inhomogeneous turbulent flows". In: *Atmospheric turbulence and radio wave propagation*.

Marusic, I., McKeon, B.J., Monkewitz, P.A., Nagib, H.M., Smits, A.J., and Sreenivasan, K.R. (2010). "Wall-bounded turbulent flows at high Reynolds numbers: recent advances and key issues". In: *Physics of Fluids* 22.6, p. 065103.

McKeon, B.J. (2017). "The engine behind (wall) turbulence: perspectives on scale interactions". In: *Journal of Fluid Mechanics* 817.P1.

McKeon, B.J. and Sharma, A.S. (2010). "A critical-layer framework for turbulent pipe flow". In: *Journal of Fluid Mechanics* 658, pp. 336–382.

McKeon, B.J., Sharma, A.S., and Jacobi, I. (2013). "Experimental manipulation of wall turbulence: a systems approach". In: *Physics of Fluids* 25.3, p. 031301.

Moarref, R., Sharma, A.S., Tropp, J.A., and McKeon, B.J. (2013). "Model-based scaling of the streamwise energy density in high-Reynolds-number turbulent channels". In: *Journal of Fluid Mechanics* 734, pp. 275–316.

Moarref, R, Jovanović, MR, Tropp, JA, Sharma, AS, and McKeon, BJ (2014). "A low-order decomposition of turbulent channel flow via resolvent analysis and convex optimization". In: *Physics of Fluids* 26.5, p. 051701.

Moré, Jorge J and Sorensen, Danny C (1983). "Computing a trust region step". In: *SIAM Journal on Scientific and Statistical Computing* 4.3, pp. 553–572.

Moser, R.D., Moin, P., and Leonard, A. (1983). "A spectral numerical method for the Navier-Stokes equations with applications to Taylor-Couette flow". In: *Journal of Computational Physics* 52.3, pp. 524–544.

Nagata, M. (1990). "Three-dimensional finite-amplitude solutions in plane Couette flow: bifurcation from infinity". In: *Journal of Fluid Mechanics* 217, pp. 519–527.

Orr, W. (1907). "The stability or instability of the steady motions of a perfect liquid and of a viscous liquid. Part II: A viscous liquid". In: *Proceedings of the Royal Irish Academy. Section A: Mathematical and Physical Sciences*. Vol. 27. JSTOR, pp. 69–138.

Park, J.S. and Graham, M.D. (2015). "Exact coherent states and connections to turbulent dynamics in minimal channel flow". In: *Journal of Fluid Mechanics* 782, pp. 430–454.

Perot, B. and Moin, P. (1996). "A new approach to turbulence modelling". In: *Proceeding of the CTR Summer Program*. Stanford University, pp. 35–46.

Reddy, S.C. and Henningson, D.S. (1993). "Energy growth in viscous channel flows". In: *Journal of Fluid Mechanics* 252, pp. 209–238.

Reddy, S.C., Schmid, P.J., and Henningson, D.S. (1993). "Pseudospectra of the Orr–Sommerfeld operator". In: *SIAM Journal on Applied Mathematics* 53.1, pp. 15–47.

Reynolds, W.C. and Tiederman, W.G. (1967). "Stability of turbulent channel flow, with application to Malkus's theory". In: *Journal of Fluid Mechanics* 27.2, pp. 253–272.

Rosenberg, K. and McKeon, B.J. (2018). "Efficient representation of exact coherent states of the Navier-Stokes equations using resolvent analysis". In: *Fluid Dynamics Research (to appear)*. DOI: 10.1088/1873-7005/aab1ab.

Rosenberg, K., Saxton-Fox, T., Lozano-Duràn, A., Towne, A., and McKeon, B.J. (2016). "Toward low order models of wall turbulence using resolvent analysis". In: *Proceedings of the CTR Summer Program*. URL: http://resolver.caltech.edu/CaltechAUTHORS:20171128-094432410.

Rowley, C. and Dawson, S. (2017). "Model reduction for flow analysis and control". In: *Annual Review of Fluid Mechanics* 49, pp. 387–417.

Rowley, Clarence W, Mezić, Igor, Bagheri, Shervin, Schlatter, Philipp, and Henningson, Dan S (2009). "Spectral analysis of nonlinear flows". In: *Journal of Fluid Mechanics* 641, pp. 115–127.

Schmid, P.J. and Henningson, D.S. (2000). *Stability and Transition in Shear Flows*. Vol. 142. Springer Science & Business Media.

Schmid, P.J. and Sayadi, T. (2017). "Low-dimensional representation of near-wall dynamics in shear flows, with implications to wall-models". In: *Philosophical Transactions of the Royal Society of London A* 375.2089, p. 20160082.

Schmid, Peter J (2010). "Dynamic mode decomposition of numerical and experimental data". In: *Journal of Fluid Mechanics* 656, pp. 5–28.

Schmidt, O.T., Towne, A., Rigas, G., Colonius, T., and Brès, G.A. (2017). "Spectral analysis of jet turbulence". In: *arXiv preprint arXiv:1711.06296*.

Sharma, A.S. and McKeon, B.J. (2013a). "Closing the loop: an explicit calculation of the nonlinearity in the resolvent formulation of wall turbulence". In: *43rd AIAA Fluid Dynamics Conference*, p. 3118.

Sharma, A.S. and McKeon, B.J. (2013b). "On coherent structure in wall turbulence". In: *Journal of Fluid Mechanics* 728, pp. 196–238.

Sharma, A.S., Moarref, R., McKeon, B.J., Park, J.S., Graham, M.D., and Willis, A.O. (2016). "Low-dimensional representations of exact coherent states of the Navier-Stokes equations from the resolvent model of wall turbulence". In: *Physical Review E* 93.2, p. 021102.

Smits, A.J., McKeon, B.J., and Marusic, I. (2011). "High–Reynolds number wall turbulence". In: *Annual Review of Fluid Mechanics* 43.

Sommerfeld, A. (1908). "Ein beitrag zur hydrodynamischen erklaerung der turbulenten fluessigkeitsbewegungen". In: *Atti del* 4, pp. 116–124.

Symon, S. (2018). "Reconstruction and estimation of flows using resolvent analysis and data-assimilation". PhD thesis. California Institute of Technology.

Taira, K., Brunton, S.L., Dawson, S., Rowley, C., Colonius, T., McKeon, B.J., Schmidt, O.T., Gordeyev, S., Theofilis, V., and Ukeiley, L.S. (2017). "Modal analysis of fluid flows: An overview". In: *AIAA Journal*, pp. 1–29.

Taylor, G.I. (1938). "The spectrum of turbulence". In: *Proceedings of the Royal Society of London. Series A, Mathematical and Physical Sciences*, pp. 476–490.

Thomas, V.L., Lieu, B.K., Jovanović, M.R., Farrell, B.F., Ioannou, P.J., and Gayme, D.F. (2014). "Self-sustaining turbulence in a restricted nonlinear model of plane Couette flow". In: *Physics of Fluids* 26.10, p. 105112.

Towne, A., Colonius, T., Jordan, P., Cavalieri, A.V., and Brès, G.A. (2015). "Stochastic and nonlinear forcing of wavepackets in a Mach 0.9 jet". In: *21st AIAA/CEAS Aeroacoustics Conference*.

Towne, A., Schmidt, O.T., and Colonius, T. (2017a). "Spectral proper orthogonal decomposition and its relationship to dynamic mode decomposition and resolvent analysis". In: *arXiv preprint arXiv:1708.04393*.

Towne, A.S. (2016). "Advancements in jet turbulence and noise modeling: accurate one-way solutions and empirical evaluation of the nonlinear forcing of wavepackets". PhD thesis. California Institute of Technology.

Towne, Aaron, Bres, Guillaume A, and Lele, Sanjiva K (2017b). “A statistical jet-noise model based on the resolvent framework”. In: *23rd AIAA/CEAS Aeroacoustics Conference*, p. 3706.

Trefethen, L.N., Trefethen, A.E., Reddy, S.C., and Driscoll, T.A. (1993). “Hydrodynamic stability without eigenvalues”. In: *Science* 261.5121, pp. 578–584.

Viswanath, Divakar (2007). “Recurrent motions within plane Couette turbulence”. In: *Journal of Fluid Mechanics* 580, pp. 339–358.

Waleffe, F. (1997). “On a self-sustaining process in shear flows”. In: *Physics of Fluids* 9.4, pp. 883–900.

Wang, J., Gibson, J., and Waleffe, F. (2007). “Lower branch coherent states in shear flows: transition and control”. In: *Physical review letters* 98.20, p. 204501.

Weideman, J.A. and Reddy, S.C. (2000). “A MATLAB differentiation matrix suite”. In: *ACM Transactions on Mathematical Software (TOMS)* 26.4, pp. 465–519.

Welch, P. (1967). “The use of fast Fourier transform for the estimation of power spectra: a method based on time averaging over short, modified periodograms”. In: *IEEE Transactions on audio and electroacoustics* 15.2, pp. 70–73.

Wu, J., Ma, H., and Zhou, M. (2007). *Vorticity and vortex dynamics*. Springer Science & Business Media.

Wu, J.Z., Zhou, Y., and Wu, J.M. (1996). “Reduced stress tensor and dissipation and the transport of Lamb vector”. In: *ICASE* Rep. 96-21.

Wu, T., Geng, C., Yao, Y., Xu, C., and He, G. (2017). “Characteristics of space-time energy spectra in turbulent channel flows”. In: *Physical Review Fluids* 2.8, p. 084609.

Zare, A., Jovanović, M.R., and Georgiou, T.T. (2017). “Colour of turbulence”. In: *Journal of Fluid Mechanics* 812, pp. 636–680.

Appendix A

SUPPLEMENTAL FIGURES

A.1 1D resolvent

In Figure A.1 we show the Reynolds stress profiles captured using the traditional approach for up to $N_p = 20$ singular modes. We observe that doubling the number of singular modes used (in comparison to Figure 3.1) still does not yield complete convergence. In Figure A.2, we show the forcing variance captured using the traditional approach for an increasing number of singular modes for the P4L/P4U solutions. In comparison to Figure 3.3 in which the split OS/SQ method is used, we see the traditional approach yields a poor low-dimensional representation of the forcing.

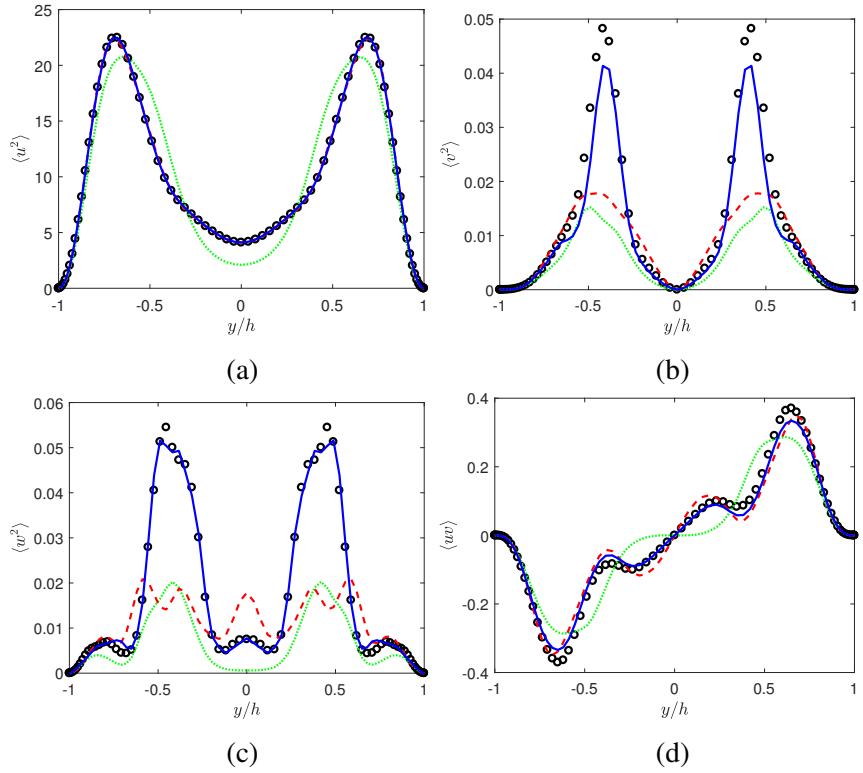

Figure A.1: Reynolds stress profiles for P4L (open circles) and their approximations based on the traditional approach using $N_p = 2$ (dotted), $N_p = 6$ (dashed), and $N_p = 20$ (solid) singular modes for (a),(d) $\langle u^2 \rangle$, (b),(e) $\langle v^2 \rangle$, (c),(f) $\langle w^2 \rangle$, (g),(h) $\langle uv \rangle$. All quantities are in inner units.

In Figure A.3, we show a comparison of the full forcing against the solenoidal

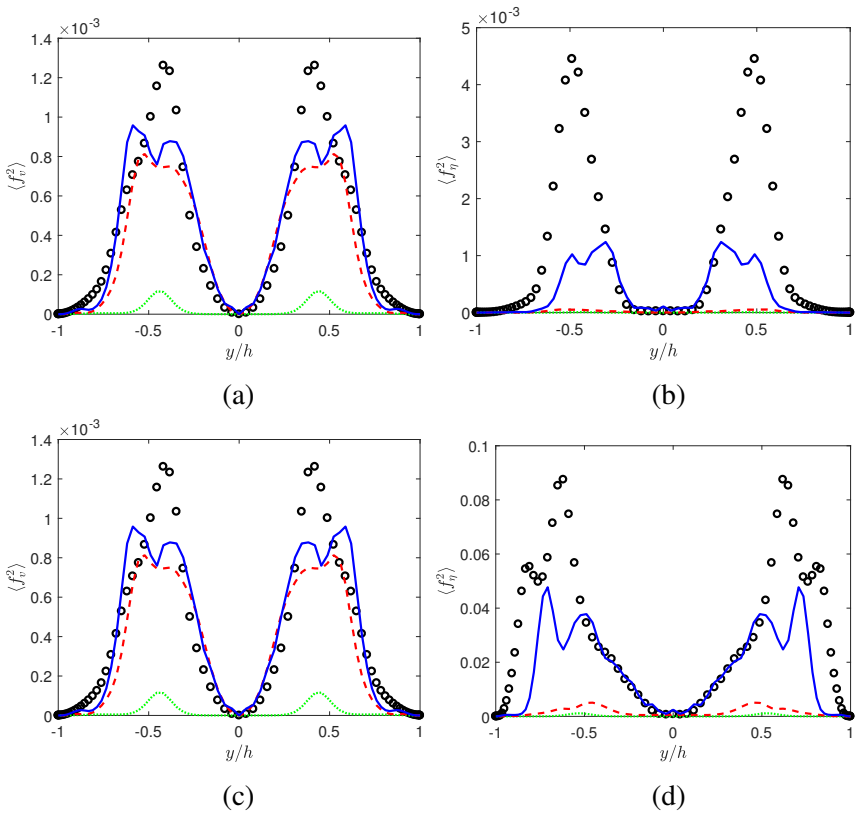

Figure A.2: Forcing variance profiles for P4L (open circles, top row) and P4U (open circles, bottom row) and their approximations via the traditional resolvent approach using $N_p = 1$ (dotted), $N_p = 5$ (dashed), and $N_p = 15$ (solid) singular modes for (a),(c) $\langle {f_v}^2 \rangle$, and (b),(d) $\langle {f_\eta}^2 \rangle$. All quantities are in inner units.

components in the form of variance profiles for the u, v, and w components for P4L and P4U. While the two look quite similar for the u component, the remaining components are quite different.

In Figure A.4, we compare the OS and SQ singular values and weights of P4U for the Fourier modes $(k_x = 0, k_z = 4)$ and$(k_x = 2, k_z = 4)$. We observe that for $(k_x = 0, k_z = 4)$, the response is initially dominated by OS modes and then later by SQ modes. For $(k_x = 2, k_z = 4)$, the response appears to have more uniform contributions from OS and SQ modes.

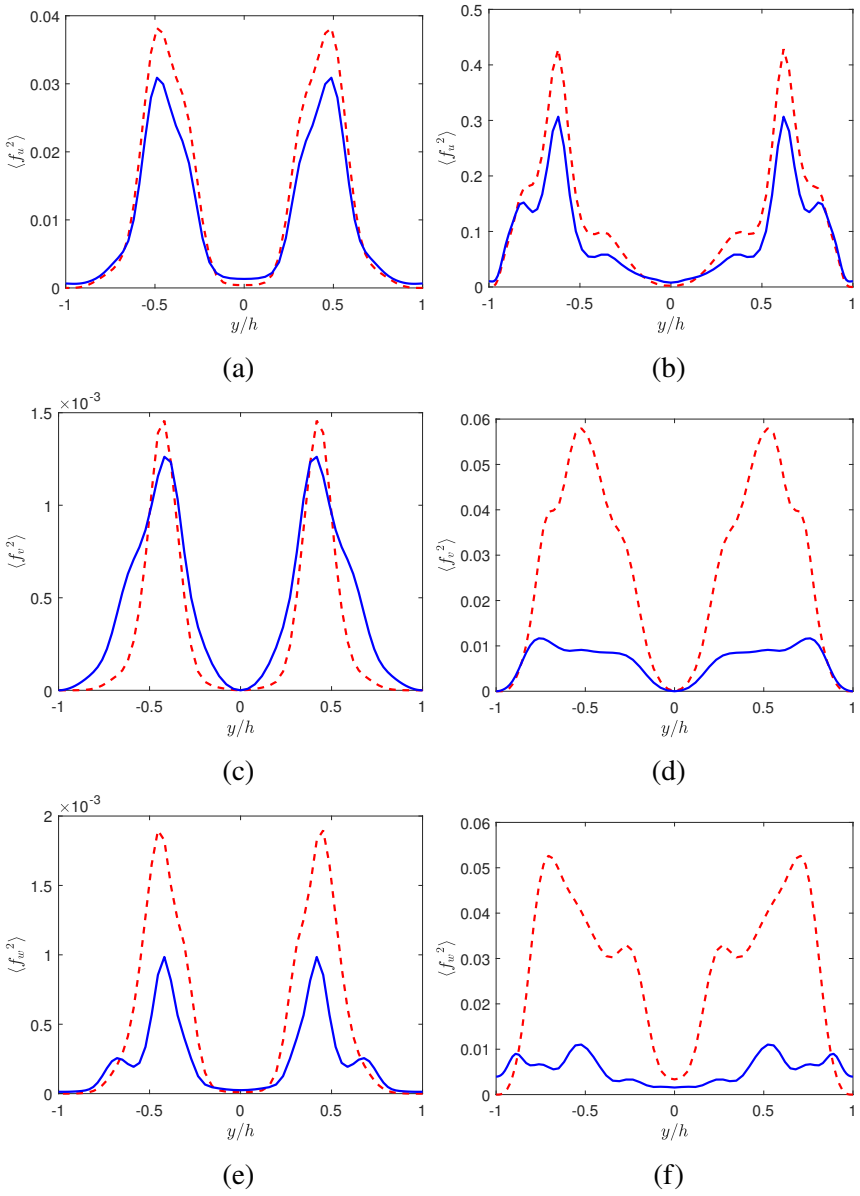

Figure A.3: Forcing variance profiles for P4L (left column) and P4U (right column) comparing the full forcing (dashed line) and the solenoidal component (solid line) for the (a),(b) *u* component, (c),(d) *v* component, and (e),(f) *w* component.

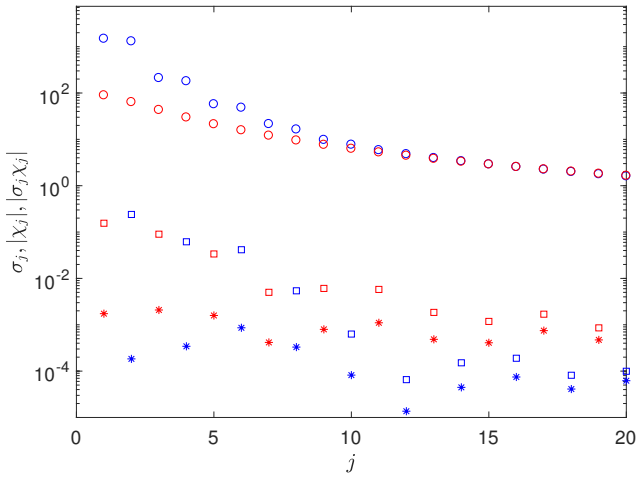

(a)

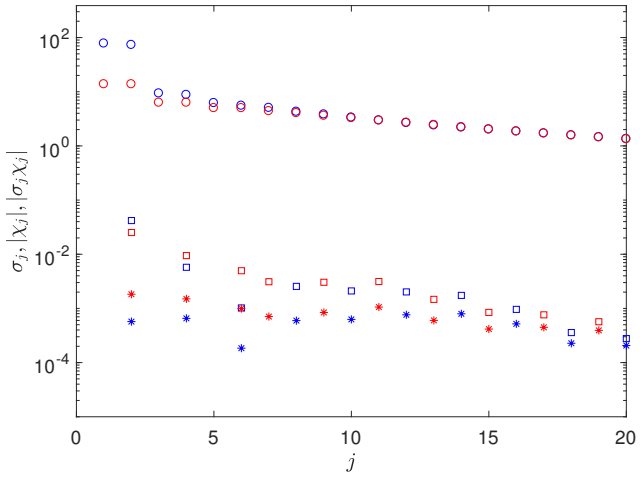

(b)

Figure A.4: Comparison of the singular values σ (circles), the amplitude of the weights $|\chi|$ (stars), and their product $|\sigma\chi|$ (squares) of P4U for OS modes (blue) and SQ modes (red) for the Fourier modes (a) ($k_x = 0, k_z = 4$) and (b) ($k_x = 2, k_z = 4$).

A.2 2D/3C Resolvent

In Figure A.5, we show the amplitude of the $\hat{u}$, $\hat{v}$, and $\hat{w}$ components of the fundamental Fourier streamwise wavenumber for P4L as well as the projection onto the leading singular mode. Also shown is a plot of the first 20 singular values and the magnitude of the product $|\sigma\chi|$. As was the case for EQ1, this lower branch solution is well approximated by its leading response mode.

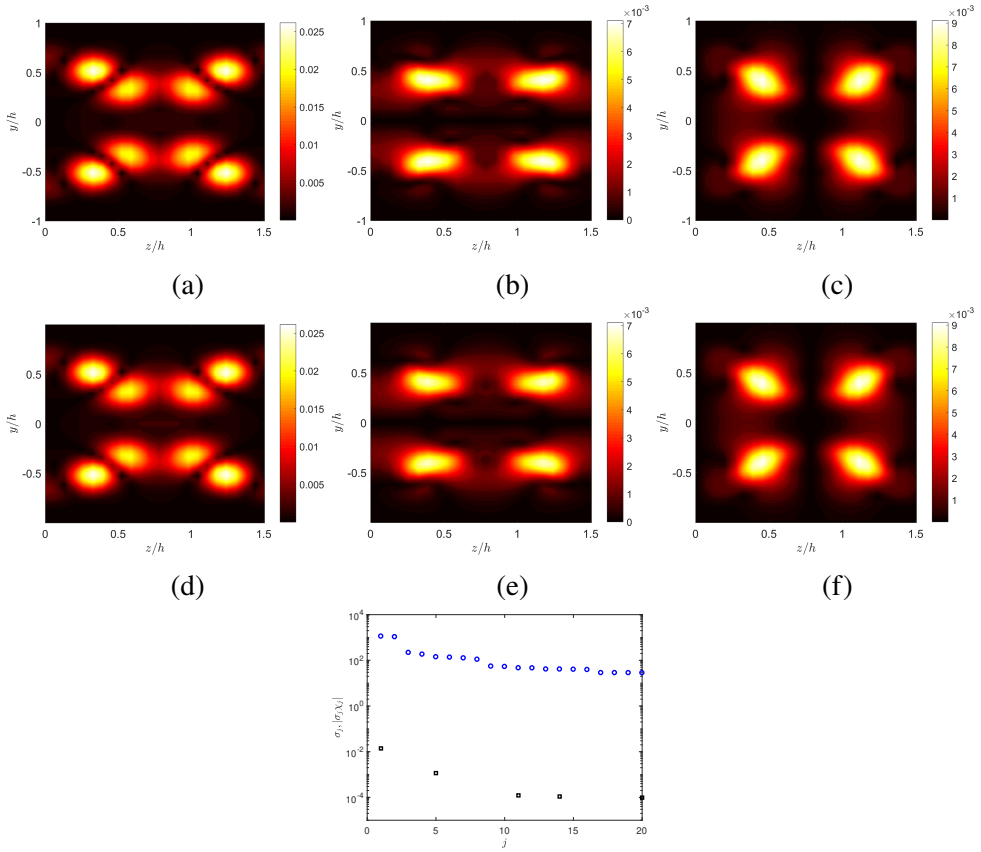

Figure A.5: The amplitude of the fundamental streamwise Fourier mode $\hat{\mathbf{u}}(k_x = 2, \omega = 2c; y, z)$ for P4L, with the top row corresponding to the true value and the middle row corresponding to the projection onto the leading response mode for (a),(d) $\hat{u}(y, z)$,(b),(e) $\hat{v}(y, z)$, (c),(f) $\hat{w}(y, z)$, along with (g) the first 20 singular values σ_j (open circles) and the product $|\sigma_j\chi_j|$ (squares).

In Figure A.6, we show the amplitude of the $\hat{u}$, $\hat{v}$, and $\hat{w}$ components of the harmonic for P4L as well as the projection onto the leading singular mode. Again, we also shown is a plot of the first 20 singular values and the magnitude of the product $|\sigma\chi|$. The lack of a dominant singular value suggests a rank-one approximation is not sufficient. However, leveraging the dominant scale interaction of the fundamental

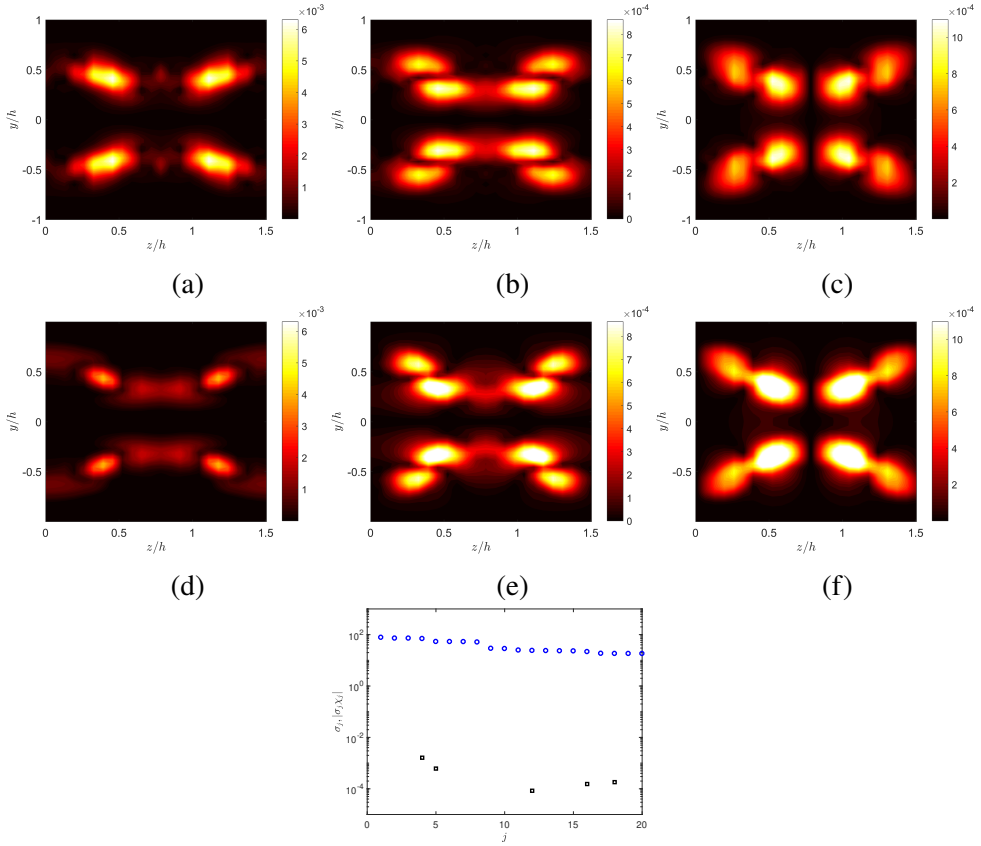

Figure A.6: The amplitude of the Fourier mode $\hat{\mathbf{u}}(k_x = 4, \omega = 4c; y, z)$ for P4L, with the top row corresponding to the true value and the middle row corresponding to the projection onto the leading response mode for (a),(d) $\hat{u}(y, z)$,(b),(e) $\hat{v}(y, z)$, (c),(f) $\hat{w}(y, z)$, along with (g) the first 20 singular values σ_j (open circles) and the product $|\sigma_j \chi_j|$ (squares).

mode, the harmonic can be recovered using Equation 3.9 as seen in Figure A.7.

In Figure A.8, we show the amplitude of the $\hat{u}$, $\hat{v}$, and $\hat{w}$ components of the fundamental Fourier streamwise wavenumber for the lower branch solution EQ10 Gibson et al., 2009 as well as the projection onto the leading singular mode. Also shown is a plot of the first 20 singular values and the magnitude of the product $|\sigma\chi|$. This behavior is consistent with the previously discussed lower branch solutions.

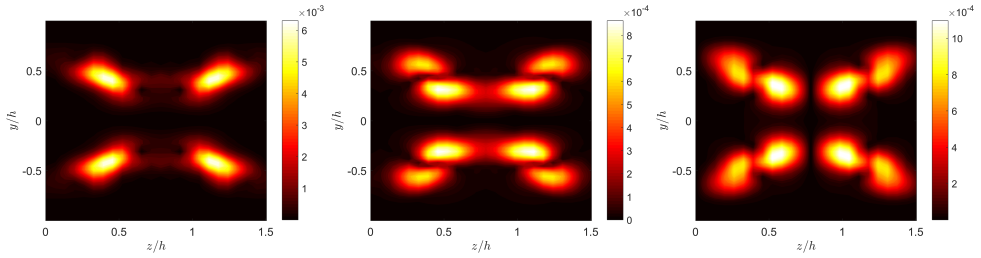

(a) (b) (c)

Figure A.7: The amplitude of the Fourier mode $\hat{\mathbf{u}}(k_x = 4, \omega = 4c; y, z)$ for P4L computed by passing the forcing generated by the interaction of the leading response mode for $(k_x = 2, \omega = 2c)$ through the resolvent operator (see equation 3.9): (a) $\hat{u}(y, z)$,(b) $\hat{v}(y, z)$ and (c) $\hat{w}(y, z)$.

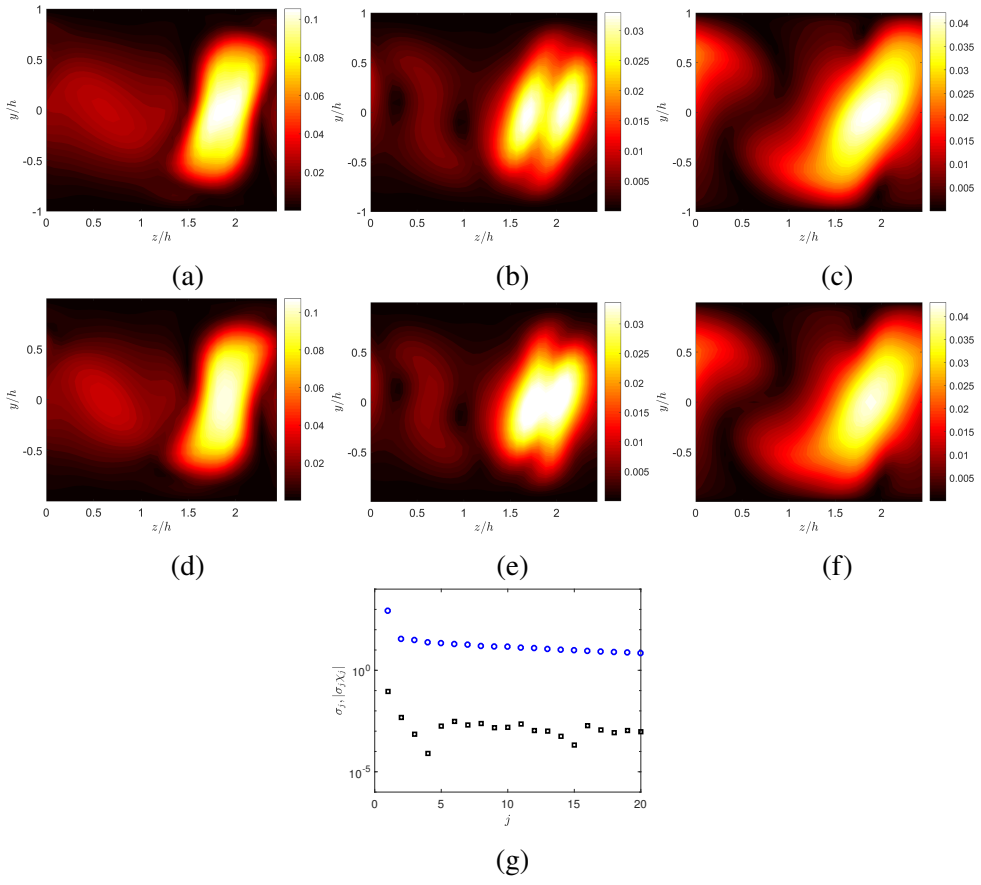

(a) (b) (c)

(d) (e) (f)

(g)

Figure A.8: The amplitude of the fundamental streamwise Fourier mode $\hat{\mathbf{u}}(k_x = 1.14, \omega = 0; y, z)$ for the lower branch solution EQ10 (Gibson et al., 2009), with the top row corresponding to the true value and the middle row corresponding to the projection onto the leading response mode for (a),(d) $\hat{u}(y, z)$,(b),(e) $\hat{v}(y, z)$, (c),(f) $\hat{w}(y, z)$, along with (g) the first 20 singular values σ_j (open circles) and the product $|\sigma_j \chi_j|$ (squares).

A.3 Coefficient solver results

In Figure A.9, we demonstrate the model proposed in Equation 3.25 to predict the mean profile of an upper branch solution from the lower branch for the pair EQ3 and EQ4 (Gibson et al., 2009). We again note this model requires the specification of a single parameter α which for this pair took the value of 2.5.

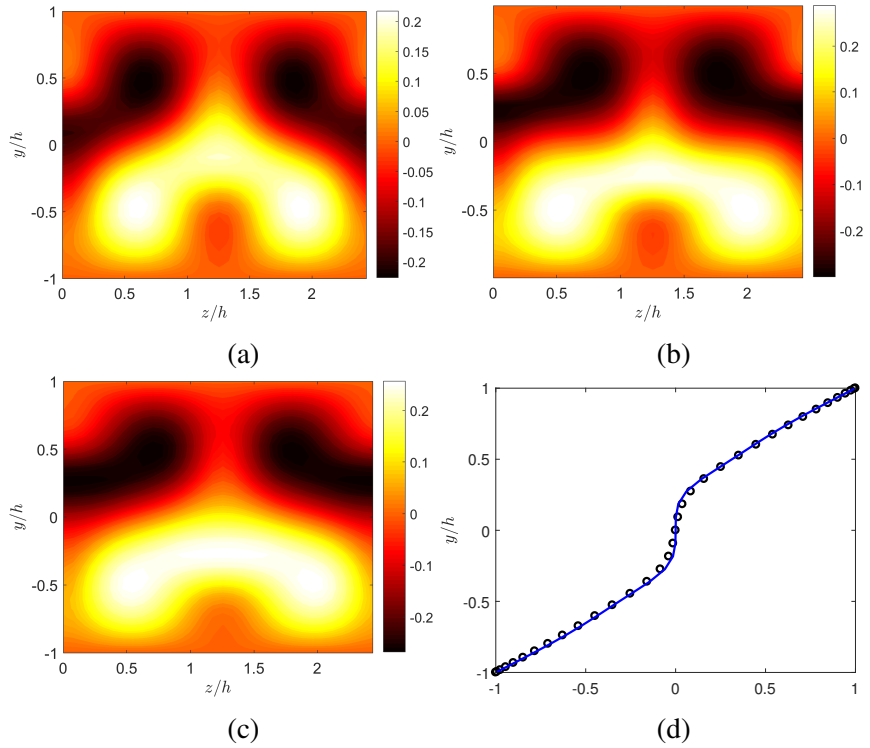

Figure A.9: The mean streamwise velocity (deviation from laminar) for (a) EQ3, (b) a guess for the upper-branch (EQ4) mean based on overly-amplified EQ3 mean-forcing (using a value of $\alpha = 2.5$ in Equation 3.25), (c) the true mean of EQ4, and (d) the corresponding 1-D mean profile (open circles- true profile, line- guess).

In Figure A.10, we demonstrate the results of the coefficient solver in which the true mean for EQ2 is used. Comparing these with the results shown in Figure 3.21 for the approximate EQ2 mean, we see we can indeed capture the correct statistics when the proper mean is used.

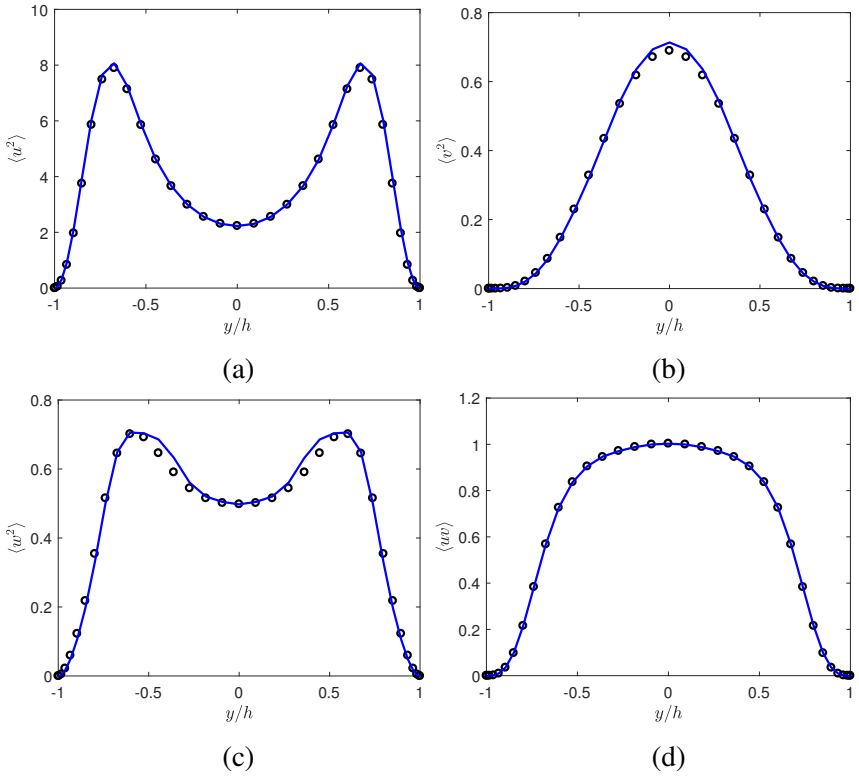

Figure A.10: Reynolds stress profiles for EQ2 (open circles) and the values based on the solution generated from the coefficient-solver (line) using the true EQ2 mean for (a) $\langle u^2 \rangle$, (b) $\langle v^2 \rangle$, (c) $\langle w^2 \rangle$, (d) $\langle uv \rangle$. All quantities are in inner units.

A.4 DNS of channel

In Figure A.11, for validation purposes we plot the mean profile and statistics for the wall-normal velocity and vorticity, comparing the results of the present DNS with the database results of Jiménez; the results are in good agreement.

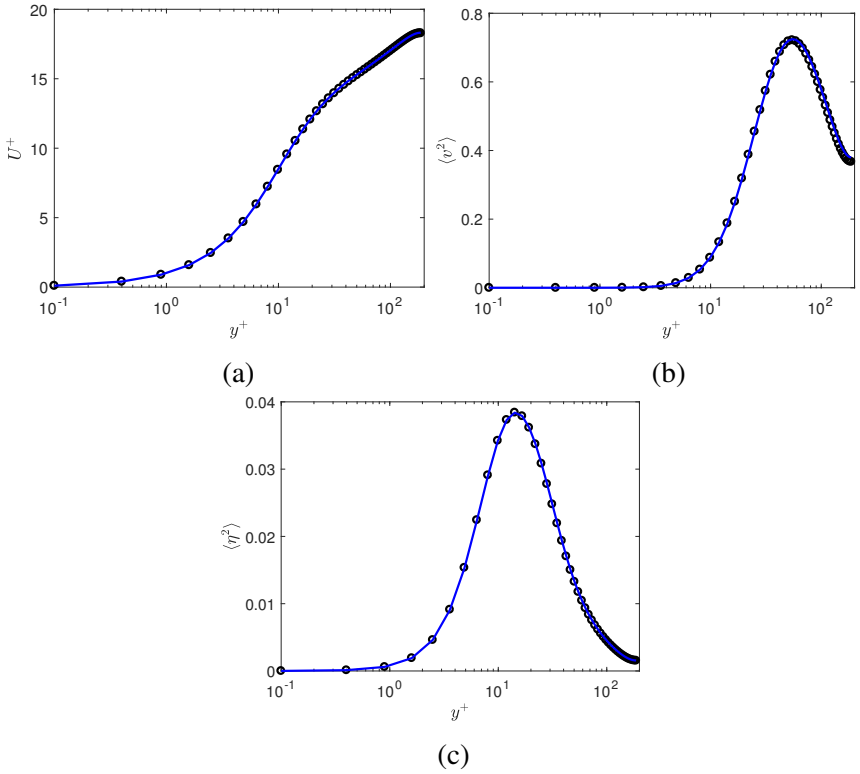

(a) (b)

(c)

Figure A.11: A comparison of statistics for the present DNS (solid line) with the database of Jiménez (open circles): (a) U, (b) $\langle v^2 \rangle$, and (c) $\langle \eta^2 \rangle$. All quantities are in inner units.

In Figure A.12, we plot the spectra of the forcing component f_{v_s} in which 20 overlapping windowed segments are used. In comparison to the results in Figure 4.2 in which 10 overlapping segments were used, we do not observe any significant quantitative difference between the two.

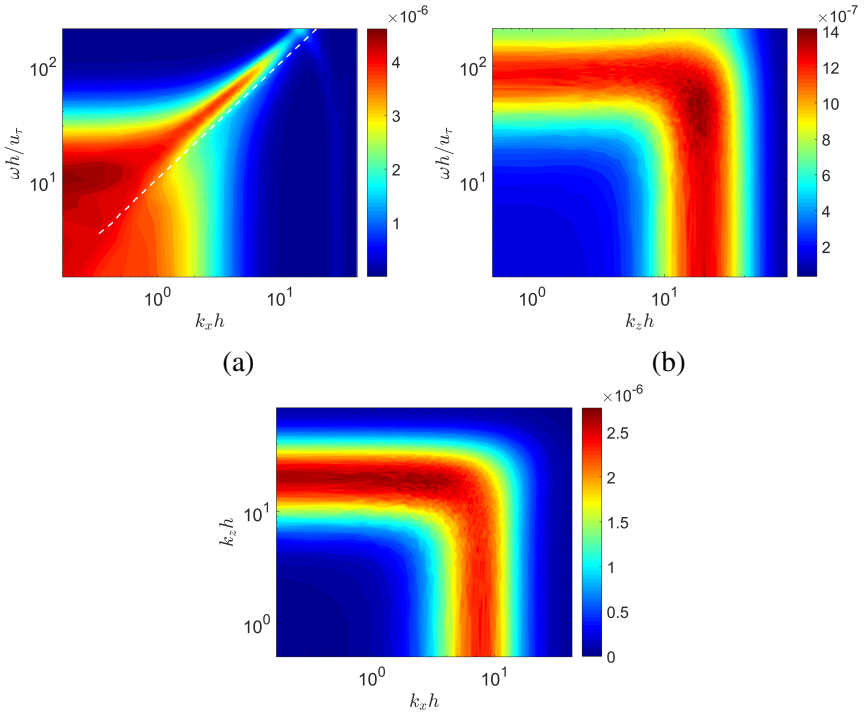

Figure A.12: 2D spectra at a fixed wall normal height of $y^+ \approx 15$ for f_{v_s} using 20 overlapping segments (in comparison to 10 segments used in Figure 4.2) plotted in the (a) k_x-ω plane, (c) k_z-ω plane, and the (e) k_x-k_z plane. No significant quantitative differences are observed.